Enhanced Earth Grid Performance by Improved Conductor Properties

A THESIS SUBMITTED TO THE SCIENCE AND ENGINEERING FACULTY OF QUEENSLAND UNIVERSITY OF TECHNOLOGY IN FULFILMENT OF THE REQUIREMENTS FOR THE DEGREE OF MASTER OF ENGINEERING (RESEARCH)

Amit Jyoti Datta

Principal Supervisor: Adj. Prof. Richard Taylor
Associate Supervisor: Prof. Gerard Ledwich
Associate Supervisor: A/Prof. Geoffrey Will

School of Electrical Engineering and Computer Science
Science and Engineering Faculty
Queensland University of Technology

Dated: 25^{th}August, 2015

Copyright in Relation to This Thesis

Statement of Original Authorship

The work contained in this thesis has not been previously submitted to meet requirements for an award at this or any other higher education institution. To the best of my knowledge and belief, the thesis contains no material previously published or written by another person except where due reference is made.

Signature:

Date: 25/08/2015

To my Family

Abstract

The quality and performance enhancement of the earth grid is one of the major challenges in todays power system design. Encroaching built environment with increased fault current levels is demanding a robust design/design approach and prolonged improved performance of the earth grid. With this in mind, the aim of the project is to perform a sensitivity analysis of the earth grid and a earthing performance evaluation with coated conductors. Subsequent to these, a conceptual design to continuously monitor the performance of the earth grid was developed. In this study, earth grid design standards were compared to evaluate their appropriate use in determining the safety condition. In addition a sensitivity test (simulation) was run with two different software packages. A process to grow a thin film of graphene on the surface of cylindrical copper rods was also developed. Earthing performance in terms of conductivity and corrosion susceptibility was evaluated with these conductors. A conceptual model was developed by implementing the insights gained from the current injection test and corrosion susceptibility testings. All of these reproducible simulations, lab and in field test results are expected to contribute to significant improvements in earthing practice.

Keywords

Touch potential, Step potential, Earth/Ground potential rise, Soil reistivity, Soil moisture content, Current injection test, Remote earth potential, Graphene, Electrochemical impedance spectroscopy, Scale model test of the earth grid, Earth grid impulse characteristics, AC corrosion, Cathodic protection, Continuous monitoring system of the earth grid.

Acknowledgement

My Master of Engineering study journey at Queensland University of Technology (QUT) would never have been possible without the immense support and guidance of various individuals. First and foremost, I have to thank my research supervisors, Adjunct Professor **Richard Taylor**, Professor **Gerard Ledwich** and Associate Professor **Geoffrey Will**. Without their assistance and dedicated involvement in every step throughout the process, this project would have never been accomplished. My special gratitude goes towards my principal supervisor Adjunct Professor Richard Taylor for his continuous support, motivation and technical contribution throughout my candidature. I would like to thank him very much for his support and understanding over the past one and half years.

I would also like to show gratitude to my thesis review committee. I gratefully acknowledge the financial support provided by **Powerlink Queensland** and the tuition fee waiver by **QUT** during my whole candidature which helped to make the research a success. Thank you to Principal Engineer (Substation electrical design) from Powerlink Queensland, **Andre Henrion** for providing me valuable direction about my research project and all the necessary data and literature for the research work. And thanks to **Luma Worrall** without whom I could have never learnt CDEGS so easily. I was also lucky to have other colleagues come supervisors like **Ralph Martin** and **Joseph Pinherio** and it was my immense pleasure to enjoy the companionship of and to learn from Joseph Pinherio during the Dalby, Qld trip.

Support from **Frank Demming** regarding the CST trial license made my simulation study convenient. I also received a good direction about Australian soil chemical behaviour from Professor **Les Dawes**.

Working in the tube furnace under the supervision of Professor **Nunzio Motta** added a new experience during my Master of Engineering study. Help in this experiment from **Mahnaz Shafiei** and **Bharati Gupta** was also noteworthy and they were very patient with my knowledge gaps in the area.

Getting through my dissertation required more than academic support. I have many, many people to thank for listening to me and for having to tolerate me over the past one and half years. I cannot begin to express my gratitude and appreciation for their friendship. **Sumit Mazumder Ami**, **Md. Nayim Kabir**, **Md. Hafizur Rahman** and **Md. Mostafizur Rah-**

man have been unwavering in their personal and professional support during the time I spent at the University. For many memorable evenings out and in, I must thank everyone above.

Most importantly, none of this could have happened without my family. Thank you to my fiance, who offered her encouragement through phone calls and messages every day despite our distant living and time zone difference. With her own brand of humour, **Susmita Chowdhury** has been lovely and supportive to me over the last several years. To my parents and my brother I am forever grateful for your affection and support. This dissertation stands as a testament to your unconditional love and encouragement.

Contents

1 INTRODUCTION **19**

1.0.1 General overview 19
1.0.2 The problem 20
1.0.3 Proposed solution 21
1.0.4 Contributions 22
1.0.5 Structure of the thesis 22

2 EARTH GRID DESIGN AND FIELD TESTING **23**

2.1 Earth grid design criteria 23
2.2 Earth grid design procedure 23
2.3 Soil resistivity layer modelling 26
2.3.1 The physics behind soil resistivity measurement 26
2.3.2 The principle of the Wenner method 27
2.3.3 Interpretation of trends in soil resistivity measurement data 29
2.4 Earth grid design safety parameters 30
2.5 Impact of the metal structures near the substation 31
2.6 Modification of preliminary design 32
2.6.1 Decreasing total grid resistance 32
2.6.2 Smaller mesh size 34
2.6.3 Limiting total fault current 36
2.6.4 Restricted access to limited areas 36
2.7 Substation current injection testing 36
2.8 Overview of the design of the substation 36
2.9 Current injection test setup 38
2.10 Reason behind operating the generator at 58Hz 39
2.11 Touch and step voltage measurement 39
2.11.1 Procedures 39
2.11.2 Sample calculation 42
2.11.3 Precision 42
2.12 Remote earth establishment 42

2.13 Earth potential rise measurement 43
2.13.1 Precision in EPR measurement 44
2.14 Discussion 44

3 COMPARISON OF THE STANDARDS IEEE-80 and IEC-60479 IN DETERMINING SAFETY CRITERIA FOR EARTH GRID DESIGN 47
3.1 Hazardous Voltages During Earth Faults 47
3.2 Comparison of IEEE and IEC safety criteria 48
3.2.1 Comparison in terms of allowable touch voltage 50
3.2.2 Comparison in terms of body resistance 51
3.2.3 Comparison in terms of allowable step voltages 53
3.2.4 Comparison in terms of surface layer resistivity 54
3.2.5 Comparison in terms of surface layer depth 55
3.2.6 Overall recommendations based on the analysis in section 3 56

4 RELATION BETWEEN THE DEPTH AND THE RESISTANCE OF THE ELECTRODE SYSTEM BURIED IN EARTH 57
4.1 Theoretical illustration 57
4.2 Simulation based illustration 58
4.2.1 For model A 58
4.2.2 For model B 59
4.2.3 For model C 61
4.2.4 For model D 63
4.3 Discussion 65
4.4 Simulation studies of conductors in use as earth grid material 65

5 SOIL RESISTIVITY: 71
5.1 Effect of temperature on soil resistivity 71
5.2 Effect of moisture content on soil resistivity 72
5.3 Soil resistivity measurement in the laboratory 74
5.3.1 Test procedure 75
5.3.2 Results and discussion 78

6 GRAPHENE COATING ON CONDUCTORS 79
6.1 Graphene as a prospective earth grid conductor coating 79
6.1.1 Structure of graphene 80
6.1.2 Electrical properties 82
6.1.3 Semiconductor-like properties 83
6.1.4 Graphene-metal interface 85

6.1.5 Prospect of good performance in soil environment . . . 86
6.1.6 Summary (Why graphene) . . . 86
6.2 Deposition and characterisation technique . . . 87
6.2.1 Graphene deposition on copper . . . 88
6.2.2 Characterisation of the graphene deposition on copper 90

7 CONVENTIONAL AND COATED CONDUCTOR TESTING 101
7.1 CDEGS simulation of earth grid system with coated conductor 101
7.2 Electrochemical impedance study of the earth grid . . . 104
7.2.1 Experimental setup . . . 105
7.2.2 Impedance spectroscopy results . . . 106
7.2.3 Corrosion performance evaluation . . . 107
7.3 Scale model test of the earth grid . . . 110
7.3.1 Test setup . . . 111
7.3.2 Test results . . . 112
7.4 Earth grid impulse characteristics . . . 113
7.4.1 Experimental results based on observations . . . 113
7.4.2 Insights into the change in impedance during a lightning impulse . . . 115
7.4.3 Preliminary results from a simulation study of the earth grid response to impulse current . . . 117

8 CORRODED CONDUCTORS STUDY 123
8.1 Corrosion types . . . 124
8.1.1 AC corrosion . . . 124
8.2 Survey of cathodic protection in use . . . 126
8.3 Summary . . . 127

9 EARTH GRID CONDITION MONITORING 129
9.1 Cathodic protection using the impressed current method . . . 129
9.2 Outline of a continuous monitoring system . . . 130
9.2.1 Stand-alone continuous monitoring system . . . 132
9.2.2 Continuous monitoring system utilizing a remote earth electrode of the telecommunication network . . . 134

10 CONCLUSION 135
10.1 Summary . . . 135
10.2 Future work . . . 136

Bibliography 137

APPENDICES **145**

A DATA USED FOR THE COMPARATIVE STUDY BETWEEN THE IEEE-80 and IEC 60479 **145**

A.1 Data of the comparison in terms of allowable touch voltage: . 146
A.2 Data of the comparison in terms of body resistance: 147
A.3 Data of the comparison in terms of allowable step voltage: . . 148
A.4 Data of the comparison in terms of surface layer resistivity: . . 149
A.5 Data of the comparison in terms of surface layer depth: 150

B Kumabarilla park earth grid injection testing report **152**

C SUPPORTING DATA OF EARTH GRID LIGHTNING STUDY WITH CDEGS **166**

Chapter 1

INTRODUCTION

1.0.1 General overview

Large power systems are normally operated with their neutral points directly earthed. At a major generating or switching station this results in the provision of a large earth grid (usually buried in the earth). The dimensions of earth grids (EG) are usually up to some hundreds of metres on a side. Metallic structures in the yard of a generating or switching station are electrically connected to the earth grid. The design of earthing systems requires a worst-case approach. It ensures that a conductor forming the grid will not fail electrically, thermally or mechanically in the worst case of maximum fault current persisting for a fault of maximum duration. There is a possibility of heavy currents flowing into the earth grid from the overhead earth wires through the tower, during a line conductor fault. Furthermore, there is the possibility of very heavy current in the earth grid due to lightning strikes. The flow of earth current during the fault or lightning conditions, results in a rise of earth grid potential with respect to a physically remote earth point. This rise of earth grid potential can lead to unsafe conditions under some conditions, for personnel and connected electrical plant. The standard [1] specifies that the maximum current flowing through a person (the shock current) should not exceed 100mA. But the resistance of the earthing system and the maximum shock current to which a person might be exposed can not be expressed with a simple equation. Therefore, the performance of an earthing system as a whole must be analysed. This study aims to investigate the potential of adding novel coatings to conventional copper earth Grid conductors, to enhance overall conductivity and diminish corrosion.

Figure 1.1: Typical view of a electrical substation. Earth grid is typically installed half a meter below the earth's surface all around the substation.

1.0.2 The problem

In general copper conductors are used as earth grid conductors. This has been implemented from the beginning of power system earthing practice. The earth grid is installed for the designed lifetime of the substation. A safe design of earth systems at a substation can not only provide means to dissipate electric current into the earth without exceeding any operating and equipment limits, but also assures that humans in the vicinity of earth facilities are not exposed to the danger of electric shocks under normal or fault conditions. For a defined prospective fault current, step and touch voltages and the rise of earth potential are kept below a safe limit. Over time, the prospective fault current increases and the state of the earth grid may change. This may occur because of a change in soil characteristics (moisture, pH, and organics), corrosion, accelerated aging from lightning and and earth current flows, the encroachment of the urban built environment thus putting the public closer to previously relatively isolated substation structures. These potentially lead to instances of higher than designed rise of earth potential,

unsafe step and touch potential and extended rise of earth potential outside the substation due to encroaching metallic structures. As a potential solution to these problems, graphene coated copper conductors were investigated with the aim to both increase conductor conductivity and reduce corrosion.

At present, there is no long term continuous monitoring of the state of earth grids in the Australian power industry. It would be very useful for earth grid designers to have data on earth grid effectiveness. This data would be most beneficial if recorded both over the long term, plus soon after the grid has been involved in conductor faults involving earth and lightning strikes. This Masters study concludes with the design details of an earth monitoring system, to be installed at a Powerlink substation.

1.0.3 Proposed solution

In order to evaluate the complex relationship between the earth grid conductors and the earth, a sensitivity analysis was performed. To gain a clearer picture of the electro-magnetic field distribution across the earth grid, two different software packages were used in a sensitivity analysis study, varying a number of parameters.

Copper has a band gap (Fermi energy) of 5.02 eV [2]. In contrast, along with many other excellent physical properties, graphene is a zero band gap semiconductor [3]. Other properties of graphene include extremely high charge (electrons and holes) mobility (230,000 cm^2/Vs), thermal conductivity (3000 W/mK), and the highest strength (130 GPa) and the highest theoretical specific surface area (2600 m^2/g) compared to any other thin film [4–8]. In total, these properties have raised its potential as a novel coating for a conductor surface, to enhance the performance of copper conductor based earth grids. The fundamental physical properties of conductors, such as band gap energy levels, and charge mobility, were investigated in graphene as a possible copper conductor coating.

The capability to continuously and non-invasively monitor the integrity of the earth grid was studied. This included the design and installation of an EG monitoring system able to study the long term system reliability and individual incidence correlation with power system disturbances at both 50Hz and lightning strikes.

1.0.4 Contributions

- A review of earth grid design system in accordance with both the IEEE-80 and IEC 60479 standards with the illustration and comparison of design criteria by CDEGS simulations (Chapter 2 and 3),

- A method for determining optimum earth grid installation depth (Chapter 4),

- A review of the current injection test and a proposed new method of testing (Section 2.7- 2.14, and section 9.2.2),

- An analysis of the effect of soil moisture content on soil resistivity (Chapter 5),

- A study of earthing performance with graphene coated metals (Chapter 6 and 7),

- A study of corroded earth grid conductors (Chapter 8),

- A proposed system for earth grid condition monitoring (Chapter 9).

1.0.5 Structure of the thesis

Chapter 2 focuses on the earth grid design standards and concludes with an account of field testing with the industry crew. Results from the field test are also included in this chapter.

Results and understandings from an earth grid sensitivity analysis is described are chapter 3 and 4.

In chapter 5, the effect of different factors in the soil resistivity of a specific area is explained with the aid of a laboratory experiment.

Chapter 6 comprises of graphene deposition and characterization techniques on the surface of a bulk copper rod. These graphene coated samples were tested in different lab environment to evaluate its use in the earthing system and is explained in the chapter 7.

In chapter 8, a study of the corroded metals and earth grid conductors is presented. In chapter 9, an outline of continuous monitoring system of the earth grid has been proposed.

Chapter 2

EARTH GRID DESIGN AND FIELD TESTING

This chapter focuses on the earth grid design standards and concludes with an account of a field testing with the industry crew. Results from the commissioning test are also included in this chapter.

2.1 Earth grid design criteria

Present day design considerations are:

- To ensure that accessible non-current-carrying metallic structures and equipment are maintained at the same potential,
- Hazardous step, touch and transfer voltages do not exist during fault conditions,
- A common earthing point is provided to reduce or eliminate static buildup,
- The initial design criteria are maintained over the design life of the installation despite additions or modifications [9].

2.2 Earth grid design procedure

IEEE-80 provides a logical flow of activities for the earth grid designer. This standard is followed all over the world for earth grid design. Figure 2.1 illustrates the sequences of the steps to design an earth grid.

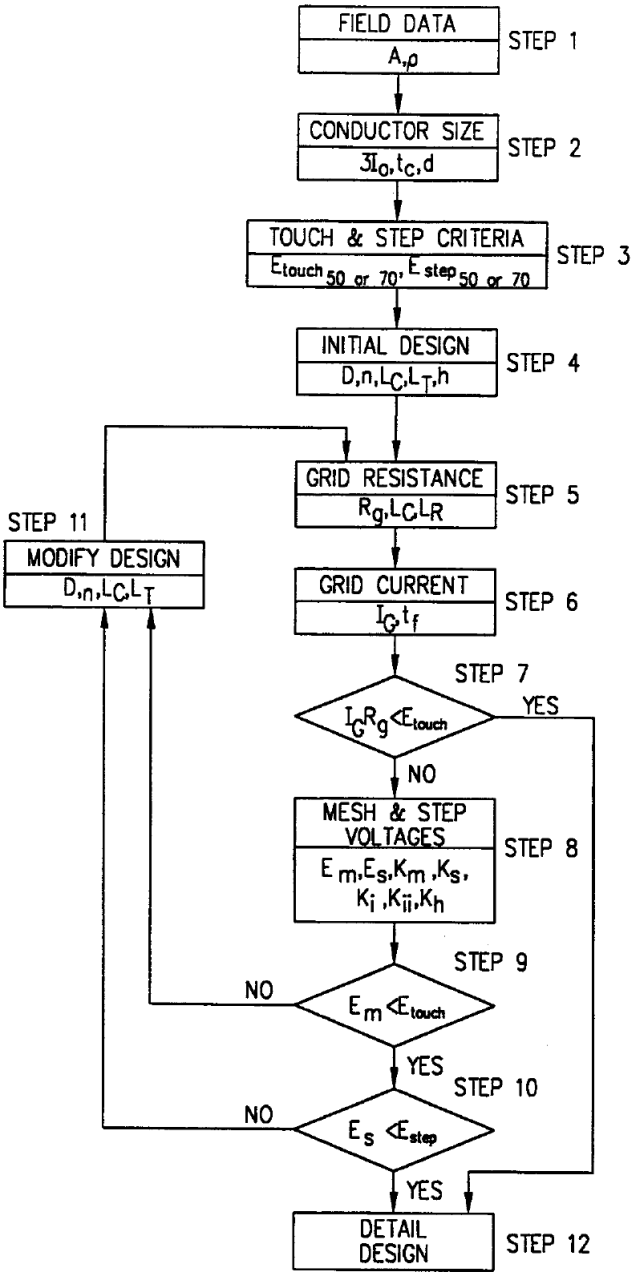

Figure 2.1: Design procedure block diagram [1]

The following describes each step of the procedure in more detail:

Step 1: The property map and the general location plan of the substation

are used to provide good estimates of the area to be grounded. From the soil resistivity test, the soil resistivity profile and soil model is determined.

Step 2: The conductor size is determined by following equation:

$$A = I * \sqrt{\frac{t_c \alpha_r \rho_r * 10^4 (TCAP)^{-1}}{\ln[1 + \frac{T_m - T_a}{K_o + T_a}]}} \tag{2.1}$$

A= Conductor area
I= RMS fault current(kA)
T_m= Maximum allowable temperature (K)
T_a= Ambient temperature (K)
T_r= Reference temperature for material constant
α_r= Thermal co-efficent of resistivity at 273 K
ρ_r= Resistivity of earth conductor at reference temperature, T_r
$K_o = (\frac{1}{\alpha_r}) - T_r$
t_c= Fault clearing time (s)
TCAP= Thermal capacity factor (J/m^3/K)

In figure 2.1, $3I_0$ refers to the maximum expected future fault current. tc, refers to the maximum possible clearing time.

Step 3: The tolerable touch and step voltages are determined by the equations given in section 2.4. Section 2.4 indicates how to calculate the tolerable touch and step voltage.

Step 4: The preliminary design should include a conductor loop surrounding the entire grounded area. The initial estimates of the conductor spacing and the ground rod locations should be based on the current I_G and the area being grounded.

Step 5: Estimates of the preliminary resistance of the earthing system in uniform soil can be determined by the method of Sverak [10] and Schwarz [11].

Step 6: The current I_G is determined from system fault studies. The current I_G refers to the maximum grid current that flows between the earth grid and the surrounding earth (including dc offset).

Step 7: Earth/Ground potential rise (EPR/GPR) of the preliminary design is compared with the tolerable touch voltage. No further analysis is necessary if GPR is less than tolerable touch voltage.

Step 8: The calculation of the mesh and step voltages for the grid can be done by approximate analysis techniques. For more precision, computer analysis techniques are used. For example, CDEGS (simulation software) is used in this purpose.

Step 9: Computed mesh voltage is compared with the tolerable touch voltage. If the computed mesh voltage is below the tolerable touch voltage then the design may be complete. If the computed mesh voltage is greater than the tolerable touch voltage, the preliminary design should be revised.

Step 10: If both the computed touch and step voltages are below the tolerable voltages, the design needs only the refinements. If not, the preliminary design must be revised (Step 11).

Step 11: If either the step or touch tolerable limits are exceeded, revision of the grid design is required.

Step 12: After satisfying the step and touch voltage requirements, additional grid and ground rods may be required. Additional grid conductors may be required if the grid design does not include conductors near the equipment to be grounded. Additional ground rods may be required at the base of the surge arresters, transformer neutrals, etc. The final design should also be reviewed to eliminate hazards due to transferred potential and hazards associated with special areas of concern.

2.3 Soil resistivity layer modelling

The earth grid design is done based upon a definite soil resistivity layer model. After the selection of the site, soil resistivity test is done. From this test data the soil resistivity layer model is designed.

2.3.1 The physics behind soil resistivity measurement

The earth surface is considered to be a homogenous isotropic medium. If a point electrode delivers I Amperes through that surface then the circuit is completed by another electrode located far enough away. The potential at the surface will be influenced by the both point sources. The potential will be a function of the distance between the electrodes.

Current is allowed to flow from an electrode to the earth. It commences its flow from a metal of low resistance and passes into the soil immediately surrounding it. The soil adjacent to the electrode can be likened to a sheath of higher resistance material. These sheaths rapidly take the shape of hemispherical shells. The surface of these shells is a loci of equal voltage. However, as the current passes through this sheath it continues into another sheath of slightly larger dimensions. Because of the larger dimensions, a greater area is provided for the current to flow, as it flows into a sheath of ever increasing area. The current flowing through the moving coil of a PMMC (permanent magnet moving coil) causes a deflection of the instrument. The coil current is directly proportional to the voltage across the coil. Therefore, the scale of the PMMC meter could be calibrated to indicate voltage.

Direct current is not usually used for testing purposes. Direct current creates the possibility of electrolysis [12]. For the alternating current consideration is given to the frequency. Electrolysis does occur even with alternating current of power frequency, and power frequency may cause stray current also. As with higher frequency it is possible to have mutual induction between the testing cables and between the cables and the earth. Since soil is a comparatively high resistance conductor there is also the probability of the skin effect of the soil. So the best frequency is probably one differing from power frequency but not too high. For example, 60 to 70 cycles per second could be an optimum frequency.

2.3.2 The principle of the Wenner method

For a cylindrical body, the resistivity

$$\rho = R\frac{A}{L} \tag{2.2}$$

with R being the electrical resistance (Ω), L the length of the cylinder (m) and A its cross sectional area (m^2).

The electrical resistance of the cylindrical body R (Ω), is defined by the Ohm's law as follows:

$$R = \frac{V}{I} \tag{2.3}$$

with V being the potential (V) and I is the current (A). Electrical characteristics are also commonly described by the conductivity value $\sigma(Sm^{-1})$, which is equal to the reciprocal of the soil resistivity. Thus:

$$\sigma = \frac{1}{\rho} \tag{2.4}$$

The conduction of the electricity in earth may be either electronic or ionic current flow. The resistance to current flow by any material may be expressed in terms of the resistivity, ρ defined by the Ohm's law expression:

$$J = \sigma E \qquad \text{or} \qquad E = \rho J \qquad \text{or} \qquad \frac{V}{r} = \rho J \tag{2.5}$$

where E is the electric field strength expressed in Vm^{-1}, J is the current density in A/m^2 In a homogenous and isotropic half space, current flows radially outwards. So, electrical equipotential is hemispherical when the current electrodes are located at the soil surfaces as in figure 2.2 [13]. The current distribution is equal everywhere on this surface which is also called an equipotential surface. The current density J then has to be calculated for all the radial directions with:

$$J = \frac{I}{2\pi r^2} \tag{2.6}$$

where the denominator is the surface of a hemispherical sphere of radius r. The potential V can then be expressed as follows:

$$V = \frac{\rho I}{2\pi r} \tag{2.7}$$

It is not likely to obtain an accurate soil resistivity result via laboratory analysis of a sample of soil taken from a site. Because, soil is nonhomogeneous and it is affected by the moisture and the temperature of the site. The onsite test would achieve a more reliable result.

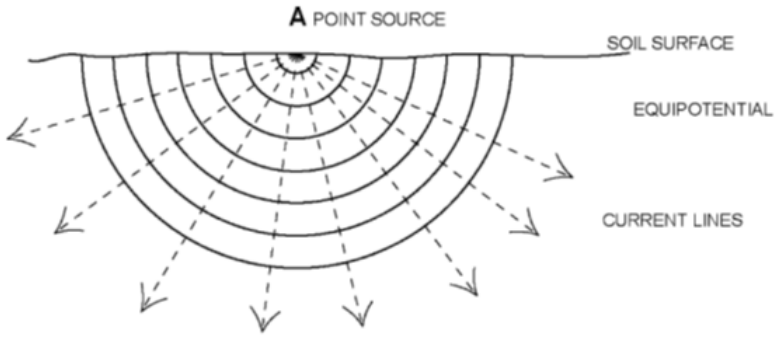

Figure 2.2: Distribution of current flow in a homogenous soil [14]

The most common technique used in the field for determining the soil resistivity is to inject a known current into a given volume of soil and measure

the voltage drop produced by the current through the soil and then calculate the resistivity using the equation:

$$\rho = 2\pi r R \tag{2.8}$$

2.3.3 Interpretation of trends in soil resistivity measurement data

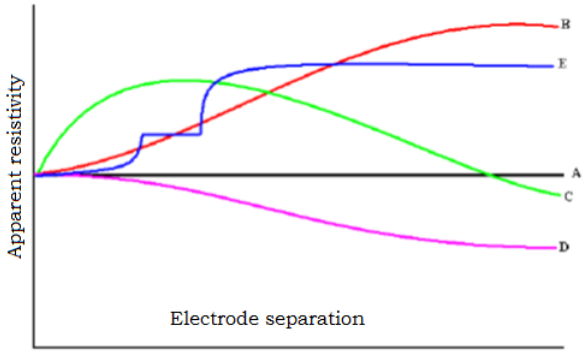

Figure 2.3: Interpretation of soil resistivity measurement data

From the curve trends in figure 2.3, the following resistivity profiles can be inferred:

- Curve (A) represents homogenous resistivity
- Curve (B) represents a low resistivity layer overlaying a higher resistivity layer
- Curve (C) represents a high resistivity layer between two low resistivity layers
- Curve (D) represents a high resistivity layer overlaying a lower resistivity layer

- Curve (E) represents a low resistivity layer over a high resistivity layer with vertical discontinuities.

From this using CDEGS as a design aid, the earth grid designer has to estimate the number of the layers of the soil. For a double layer model Sundaes graph is used to find out the depth of the each soil resistivity layer. The RMS error between the measured and 'CDEGS RESAP module simulated' value below 40% are generally acceptable.

2.4 Earth grid design safety parameters

The conductor size of the earth grid is determined after doing the fault current study. Then the tolerable step and touch potential is calculated for the system. This is done to set up a safety threshold level. In other words, it will allow a designer to check the step and touch voltage for a fault condition against the threshold values.

The earthing resistance of the earth grid of substations extending over large areas and with low soil resistivity is usually small. If the design of the earthing system is not suitable, then when a earthing fault takes place, the potential gradient on the earth surface may be very high. This may generate high step and touch voltages which would be dangerous to people and power apparatus [15]. The voltage difference between an earthed metallic structure and a point on the earth's surface separated by a distance equal to a man's normal maximum horizontal reach (approximately one metre) is referred to as the touch voltage. If the reference is between two points on the earth's surface then it is called the step voltage [16]. Touch and step voltage depends also on the soil resistivity.

Equations for touch and step voltage determination are [1]:

$$E_{touch50} = (1000 + 1.5C_s.\rho_s)\frac{0.116}{\sqrt{t_s}} \tag{2.9}$$

$$E_{touch70} = (1000 + 1.5C_s.\rho_s)\frac{0.157}{\sqrt{t_s}} \tag{2.10}$$

$$E_{step50} = (1000 + 6C_s.\rho_s)\frac{0.116}{\sqrt{t_s}} \tag{2.11}$$

$$E_{step70} = (1000 + 6C_s.\rho_s)\frac{0.157}{\sqrt{t_s}} \tag{2.12}$$

Where

$$C_s = 1 - 0.106[\frac{1 - \frac{\rho_{soil}}{\rho_s}}{2h_s + 0.106}] \tag{2.13}$$

Here, E_{step50} and E_{step70} is the step voltage in Volts for a body mass of 50 kg and 70 kg, respectively; $E_{touch50}$ and $E_{touch70}$ is the touch voltage in Volts for a body mass of 50 kg and 70 kg; t_s is the duration of shock current in seconds; C_S is the reduction factor for derating the nominal value of surface layer resistivity ρ_S with a thickness of h_S laid on a native soil of resistivity ρ_{soil}.

2.5 Impact of the metal structures near the substation

$E_{touch} < I_G R_G$ refers to the requirement for refinement in design. One of the primary reasons for requirement of refinement of design could be not considering metal structures near the substation.

For substations located in regions with high soil resistivity, decreasing the earthing resistance of the earthing system for the substation to a safe value is very difficult. But if the earthing system design adopts countermeasures to equalize the potential gradient of the earth surface and so decrease the maximum of touch and step voltages, then the earthing system can still satisfy safety demands.

The presence of metallic structures in the vicinity of the designed substation causes remote earth points to shift from their predicted locations. This extends the possibility of hazardous voltages outside the substation. From figure 2.4, it could be said that, any metallic structure in the exponential decay region of the figure can draw hazardous voltage to the earth outside the substation.

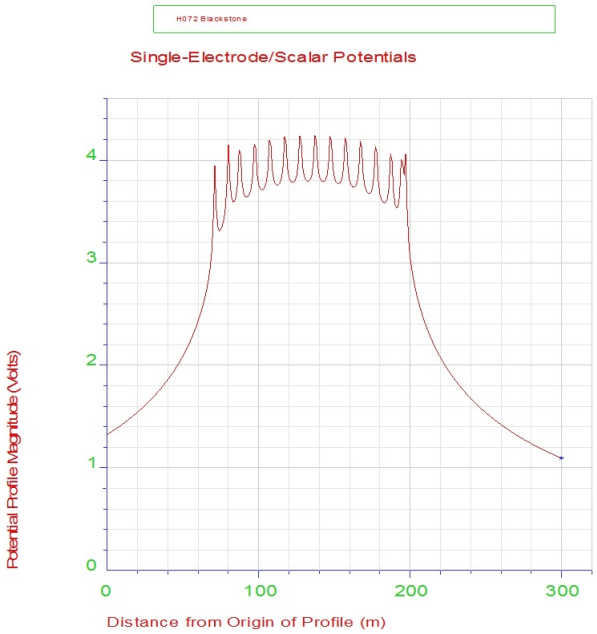

Figure 2.4: Impact of the metal structures near the substation

2.6 Modification of preliminary design

In the preliminary earth grid design calculations and simulations, there might be indication of dangerous voltages within the substation. The following refinement can then be applied where appropriate.

2.6.1 Decreasing total grid resistance

A decrease in the total grid resistance will decrease the maximum EPR. The most effective way to decrease earth grid resistance is by increasing the area occupied by the grid. This can be achieved by using a vertical earth rod which is the most common form of electrode used to decrease the total grid resistance. It can be driven deep into the moisture level below the earth to take advantage of a low-resistivity soil. This lower resistivity may be due to the soil type and/or an increased moisture level at greater depth. On the contrary, in the case where the top soil-layer resistivity is less than the bottom-layer resistivity, the earth grid with and without a earth rod will slightly reduce the value of GPR. This indicates that the current density over the grid directly affects current distribution to the soil layer. Therefore,

the design and construction of the earth grid in areas where the top soil-layer resistivity is less than the bottom-layer resistivity, can lessen the number of ground rods required in the grid [17].

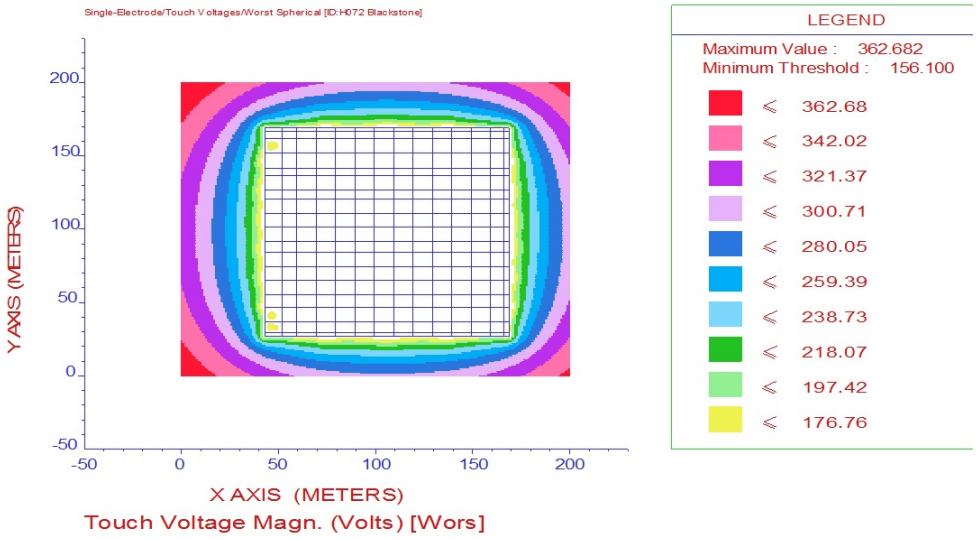

Figure 2.5: Spot 2D view of the earth grid design for inspecting existence of hazardous potential inside the substation

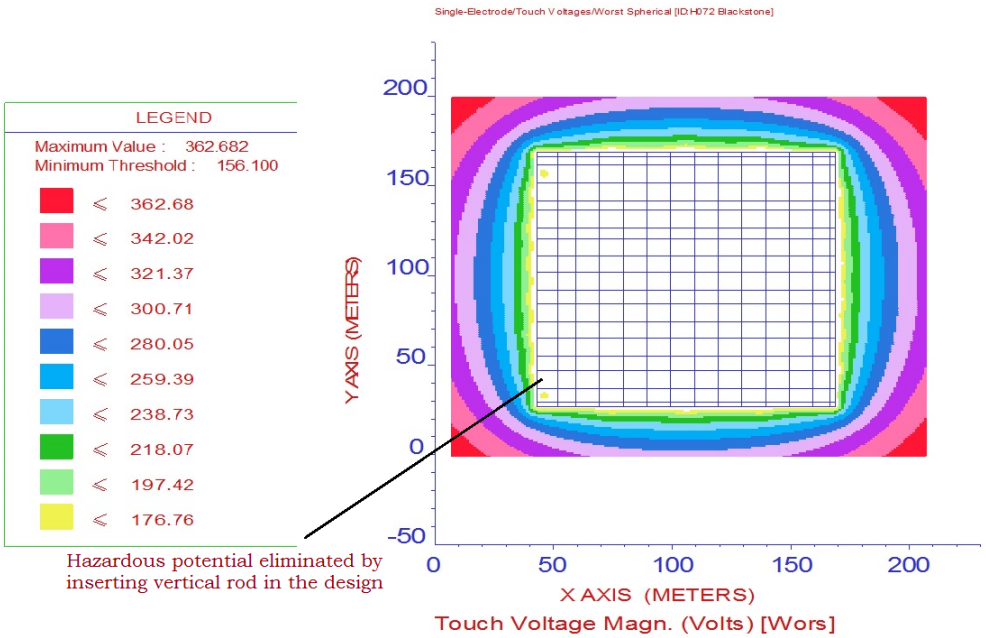

Figure 2.6: Spot 2d view of the earth grid design after increasing the number of vertical rods to manage local hazardous potential

2.6.2 Smaller mesh size

Spacing of the grid conductors can be decreased to make the mesh size smaller. Hazardous voltages inside the substation can thus be eliminated. At a small substation when the resistivity can be high this troubleshooting is little difficult. In this case often the earth grid is extended outside the substation fence. Another effective and economical way to control gradients is to increase the density of ground rods at the perimeter. Two or more parallel conductors around the perimeter are buried at successively greater depths as distance from the substation is increased. Sverak's [18] approach which varies the grid conductor spacing with closer conductors near the perimeter of the grid is also worth mentioning. These are the approaches to control perimeter gradients and step potential.

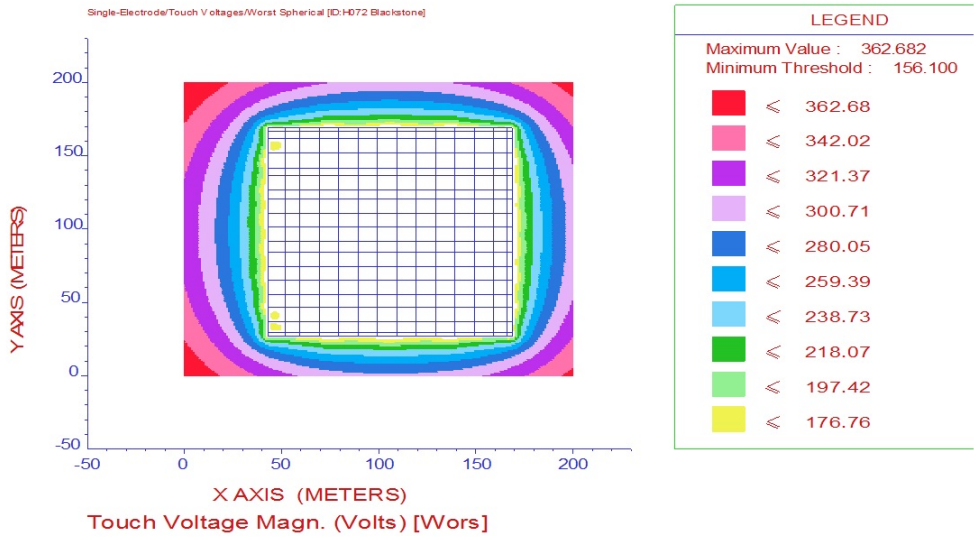

Figure 2.7: Spot 2D view of the earth grid design for investigating the impact of smaller mesh in EG design for eliminating hazardous potential

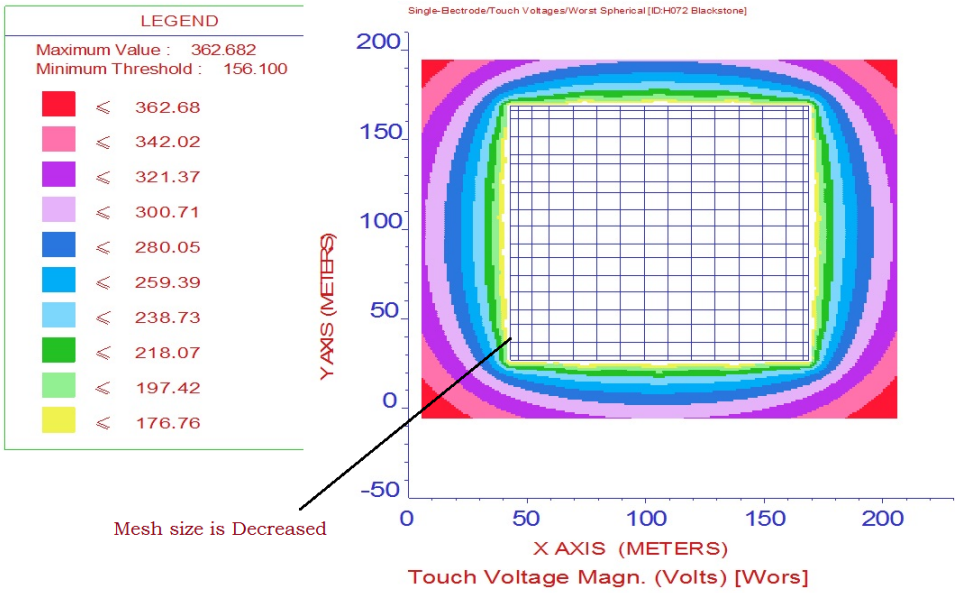

Figure 2.8: Spot 2D view of the earth grid design after decreasing mesh sizing to manage local hazardous potential

2.6.3 Limiting total fault current

In order to decrease the GPR, total fault current of the whole system could be limited to a smaller value. By connecting ground wires to the transmission lines or by decreasing the tower footing resistances near the substation, part of the fault current will be diverted from the grid. But increasing the fault clearing time for this purpose would not reduce the probability of hazard.

2.6.4 Restricted access to limited areas

Restricting access to certain possibly hazardous areas will reduce the probability of accidents to personnel.

2.7 Substation current injection testing

A (275/132kV) substation situated near Dalby, Queensland was the site of the cuurent injection test. Its dimension are around 140 m by 180 m. In this report this substation will be designated as "Sub-A".

2.8 Overview of the design of the substation

For the earthing system design study of Sub-A, the conservative soil model in table 2.1 was utilised:

Table 2.1: CDEGS generated soil model of Kumberilla [19]

Layer	Soil Resistivity (Ω m)	Depth (m)
Top	350	0.4
Middle	20	4
Bottom	35	Infinity

The allowable prospective step and touch voltages given in the following table have been calculated using the soil resistivity data detailed in the previous table. The voltages have been calculated based on a 50 kg body and 70 kg body. The 70kg safety criterion is only used within the substation area with a 100 mm thick crushed rock layer in the order of 3000 Ωm. For this study, clearing times of 0.5 seconds are utilised for the step and touch voltage safety calculations.

Table 2.2: Allowable touch and step potential

Fault case	Clearing time	Body weight	Touch potential		Step potential	
			No crushed rock (8Ωm soil)	Crushed rock (0.1m 3000Ωm soil)	No crushed rock (8Ωm soil)	Crushed rock (0.1m 3000Ωm soil)
275kV	0.5	50 kg person	166 V	474 V	172 V	1403 V
		70 kg person	225 V	642 V	233 V	1900 V

The worst earth fault level for the initial configuration is as follows:

Table 2.3: Worst earth fault level for theinitial configuration

System Voltage	X/R ratio	Clearing time (s)	Grid current	Adjusted grid current
275 kV	11.27	0.5	7939.3 A	8220 A

The following minimum conductor size is required at the Sub-A:

Table 2.4: Conductor size requirement

Fault level (kA)	Location	Clearing time (s)	Conductor size (mm^2)
40	Earth tails/risers	0.31	115
28 (70% of 40kA)	Buried earth Grid	0.31	80.5

Therefore, based on equipment designed for afault level of 40 kA for 0.31 seconds the required conductor sizes are:

Earth bonds/tails = 120 mm^2 copper conductor
Buried earth Grid = 95 mm^2 bare stranded copper conductor
Based on the grid current and the local earth grid resistance, the expected EPR at Kumbarilla Park Substation is:
Earth potential rise = I_g x $R_g = 8220A * 0.093\Omega = 765$V

The expected worst prospective step and touch voltages within and around the substation are given in the table 2.5:

Table 2.5: Worst prospective touch and step potential inside and outside the substation

Fault scenario	Maximum touch voltage (V)		Maximum step voltage (V)	
	Inside	Outside	Inside	Outside
275 kV	60 V	50 V	20 V	63 V

All incoming water services (via metallic pipes) to the substation should be isolated to a minimum of 6 m from the edge of the substation grid. This will limit the transfer hazard to any metallic services outside the substation. A commissioning test will confirm that there is no transfer hazard to the neighbourhood properties (via water services) around the Sub-A during an earth fault.

2.9 Current injection test setup

The earthing measurements are made with a full phase-to-earth fault current in a substation because it provides the most accurate step, touch, and transfer voltage data. However, this type of test is rarely performed after the establishment of a substation unless there are some demanding reasons such as: determination of the circuit parameters, equipment performance observation and protection characteristics existence. The staged fault test was performed in the same manner as described in the following figure:

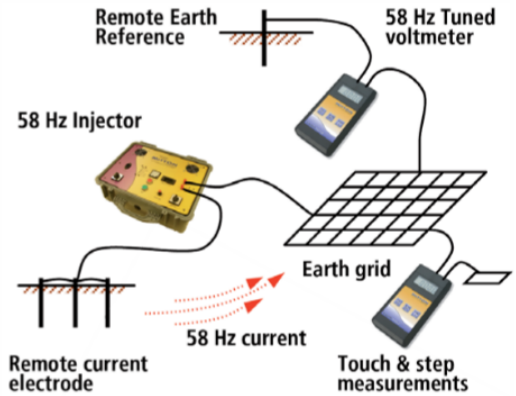

Figure 2.9: Schematic diagram of the current injection test setup [20]

2.10 Reason behind operating the generator at 58Hz

Inductive coupling can occur between the components of two or more AC circuits. The coupling effect between the test leads becomes significant when measuring the low values of the earth impedance. Any voltage produced in the potential lead due to the coupling effect is directly added to the true voltage and it produces a measurement error. The 50 Hz or 60 Hz inductive coupling between the two parallel test leads might be as high as 0.1 Ω/100 m. As a result, the error can be appreciable. Because low earth impedance usually occurs in the earth grids that cover large areas, long test leads are typically required to reach the remote earth.

Conversely, a earth grid that covers a small area usually has relatively high earth impedance, and shorter test leads can be used to reach the remote earth. Thus, the effects of coupling can be expected to be worse in the measurements of large-area, low-impedance earth grids. If the lead impedance is a problem, it is removed by the four wire method. A current is injected by two current carrying leads while the potential rise is detected with two voltage sensing leads. This is routinely applied in micro-Ohm meters (for joint and contact resistance testing). To eliminate 50/60 Hz power system interference, the test devices are operated at a test frequency that is slightly above or below [21] the power frequency to obtain more accurate measurements.

2.11 Touch and step voltage measurement

2.11.1 Procedures

The steps for the measurement procedure are as follows:

a) Test current is circulated between a remote point and the grid being tested. Local potential differences are usually tested along with the station earth impedance.

Figure 2.10: (a) Transmission grid isolator opened (b) Generator fed into the transmission line

b) The potentials can be measured differentially using a twisted wire pair attached to the two probes (step voltage) or attached to one probe and a clip to a nearby metallic structure (touch voltage). It is preferable to use a varying frequency voltmeter/multimeter.

c) The probes are needed to make good contact with the underlying soil. A separate battery-powered AC ohmmeter can be configured to measure the resistance between the probe and the station earth. This confirms that its resistance is small compared to the input impedance of the main test instrument.

d) Relatively thin rods (6 mm diameter) are much easier to drive than permanent ground rods (18 mm diameter). The rods must be rigid, smooth, and corrosion resistant. Penetration up-to 150 mm into the moist subsoil is usually sufficient [22].

e) Wireless communications between the person placing the probes and the person making the measurements helps to speed up the testing.

f) Using a tape measure and placing several probes, or using a global positioning system unit, reduces positional errors.

g) The step or touch voltage is normally measured as a voltage relative to a remote earth potential probe or relative to the earth grid. The test current is also recorded. The measured voltages are then scaled by the fault current that might enter the interconnected earthing system, and the touch or step voltage is determined.

h) To assess safety, the measured touch and step voltages are compared with the tolerable voltage limits as defined by IEEE Std 80. As defined, these limiting voltages depend on the tolerable current limit, the resistance under the feet and the duration of the fault.

Figure 2.11: (a) Touch voltage measurement (b) Step voltage measurement

2.11.2 Sample calculation

I_g = 8250A
But current injected = 25 A
So scaling factor = 8250/25 = 330
Touch voltage reading = 0.08V
Equivalent reading = 0.08V x 330 = 26.4V < allowable touch voltage (166V)

2.11.3 Precision

The impedance of the test electrodes can have a significant effect on the accuracy of the impedance measurements. A earth test is performed using the two-point test method. The measurement error can be minimized if the impedance of the test electrode is negligible with respect to the earth being tested. A earth test could also be performed using the three-point test method also. The measurement error can be minimized if the impedance of the test electrode is similar in magnitude to the impedance of the earth being tested. In the case of impedance measurements using the fall-of-potential method, the requirements for the test electrodes are not as critical.

Often, the most effective way of increasing the test current is to decrease the current electrode resistance. The resistance of the test electrode can be reduced by

- driving the rod deeper into the soil,
- pouring water around the rod,
- driving additional rods and interconnecting them in parallel,
- the addition of salt to the water poured around the test electrodes is of very little value; the moisture is the main requirement.

2.12 Remote earth establishment

Remote earth refers to a point where the voltage is zero. Theoretically it is the centre of the earth. But in the practical case of measurement it is referred to a point where there is no impact of the voltage source. So in case of this current injection test, the point where there will be no voltage from the generator will be referred as remote earth. From the design documents of the substation, the remote earth point can be assumed , and using the GPS device, electrodes could be set up around that point. Then by measuring

the impedance over that point, the location of the remote earth point can be verified.

Figure 2.12: Remote earth point establishment

2.13 Earth potential rise measurement

Earth potential rise (EPR) is measured with respect to the remote earth point. For the EPR measurement one probe has to be in the remote earth point, and the measurement starts at the substation fence. EPR is expected to decrease gradually from outside the substation to a constant value.

Figure 2.13: (a) EPR measurement near substation fence (b) EPR measurement a distance from the substation

2.13.1 Precision in EPR measurement

Partially or completely buried objects (such as rails and metallic pipelines) located in the vicinity of the earth being tested will have considerable influence on the test results [23, 24]. The earth potential contours are distorted and gradients are increased when measured above buried metallic objects. The influence of these structures on the soil resistivity measurement results can be minimized by aligning the test probes in a direction perpendicular to the routing of these structures. The test probes have to be located as far as possible from buried structures. Test lead coupling can be minimized by appropriately routing the potential and current leads. When the test lead coupling is anticipated, appropriate routing may include separating the leads or crossing the leads at 90^o.

2.14 Discussion

The measurement of local potential differences can raise the following issues:

a) Some publications have suggested using a conductive shoe to contact the

soil surface for measuring the step or touch voltages. This method is likely to fail if the desired contact resistance with the surface is not achieved.

b) Phase angles (if available on the test instrument) do not need to be recorded when measuring differentially between two nearby points. Even when testing sequentially with a single test lead (subtracting two nearby readings) the phase angles tend to be practically the same and can be ignored.

c) Local potential differences tend to be small (a fraction of the earth potential rise) so the test instrument needs to have sufficient resolution (better than 1 mΩ) and good 60 Hz noise cancellation performance.

d) It can be difficult to judge where the highest potentials will occur. Given that only a limited number of probe locations can be tested within the available time, drawings of the grid layout, or underground cable tracing equipment can be helpful.

e) Seasonal changes in the soil moisture can affect the test results. The highest potentials normally occur when the surface soil resistivity is at a maximum. Hilly areas without the plant cover and with the sand or gravel subsoil may experience the largest seasonal changes.

f) The results require adjustment if the injected test current causes different splits in overhead ground wires or interconnected neutrals.

g) Surfaces finished with asphalt or concrete are difficult to access with probes. It might be possible to find adjacent accessible areas having a similar offset from nearby buried grounding conductors that can provide a similar step or touch voltage.

h) Errors can be introduced due to potential differences present across the grid. These errors are most likely to occur close to where the test current generator is connected to the earth grid.

i) The current probe has to be injected at a sufficient distance from the earth grid being investigated. For better accuracy it is suggested that this distance needs to be at least five times the largest dimension of the earth grid.

Chapter 3

COMPARISON OF THE STANDARDS IEEE-80 and IEC-60479 IN DETERMINING SAFETY CRITERIA FOR EARTH GRID DESIGN

Results and understanding obtained from the earth grid sensitivity analysis are described in the following two chapters.

3.1 Hazardous Voltages During Earth Faults

Power system earth fault, encroachment of urban built environment may contribute to an earth potential rise inside and outside the substation fence. For a 40 kA earth fault, earth potential rise of an earth grid with four meshes, dimensions of 30 m by 30 m has been projected in the figure 3.1. An earth grid is designed to protect the human and electrical apparatus even at the occurrence of possible maximum earth potential rise due to any fault incident. Several articles have reported that designing the earth grid only with the aid of IEEE 80 will not completely ensure safety [25–27].

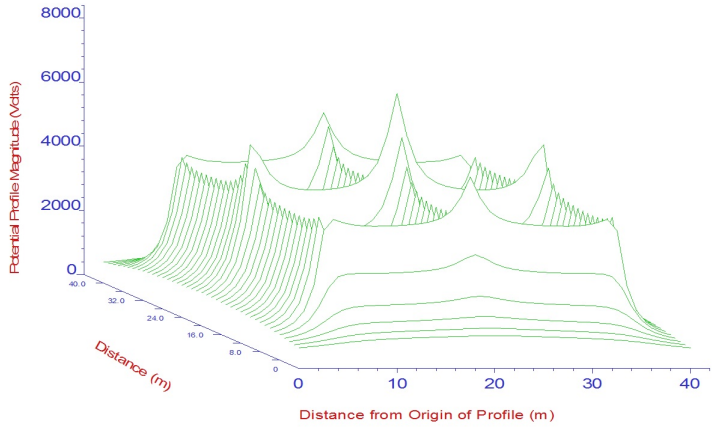

Figure 3.1: Surface potential for 30m x30m earth grid. Burial depth=0.5 m. Top soil layer resistivity=1000 Ωm; Bottom soil layer resistivity=100 Ωm. Fault current=1000 A

3.2 Comparison of IEEE and IEC safety criteria

IEEE 80 provides a risk-based approach for assessing the earth grid design while IEC 60479 comprises of a deterministic approach [28]. The method for establishing the safety criteria with IEC 60479 is like as follows:

- From figure 3.2 the value of permissible body current is determined. This calculation is done for a given fault clearing time. The probability of ventricular fibrillation is assumed in this case.
- Using the standard tables, corresponding body resistance is determined.
- Then foot resistance is calculated with the IEEE80 standard.
- Then finally, the touch and step voltages are computed.

The following sections provide a comparison between the two standards. The basis of comparison of the standards is different in each case. In each curve, a CDEGS simulation was run tofind the coordinates for each of points. With these generated data, the following curves were generated using MATLAB.

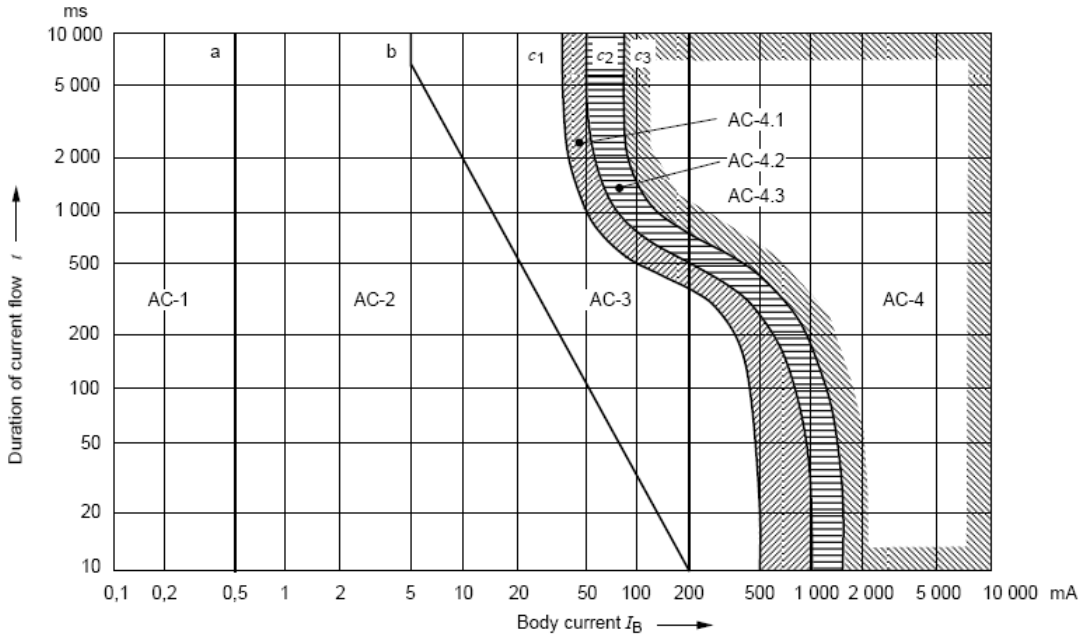

Figure 3.2: Permissible body current versus duration curve [29]

Table 3.1: Explanation of figure 3.2

Zones	Boundaries	Physiological effects
AC-1, AC-2	Up to curve b	No harmful physiological effect
AC-3	Curve b and above	Strong involuntary muscular contractions. Difficulty in breathing. Reversible disturbances of heart function. Immobilization may occur. Usually no organic damage would be expected
AC-4	Above curve c_1	Patho-physiological effects may occur. Probability of ventricular fibrillation increasing with current magnitude and time.
AC-4	$c_1 - c_2$	AC-4.1 Probability of ventricular fibrillation increasing up to 5%
AC-4	$c_2 - c_3$	AC-4.2 Probability of ventricular fibrillation increasing up to 50%.
AC-4	Beyond curve c_3	Probability of ventricular fibrillation above 50%.

3.2.1 Comparison in terms of allowable touch voltage

Fault clearing time was varied for the earth grid sytem described in section 3.1. This was done using the IEEE standard with 50 kg and 70 kg body mass model, and using IEC c1, c2, c3 model with a 50^{th} percentile rank of the population surveyed. Changes in allowable touch voltage was observed with the change in the models.

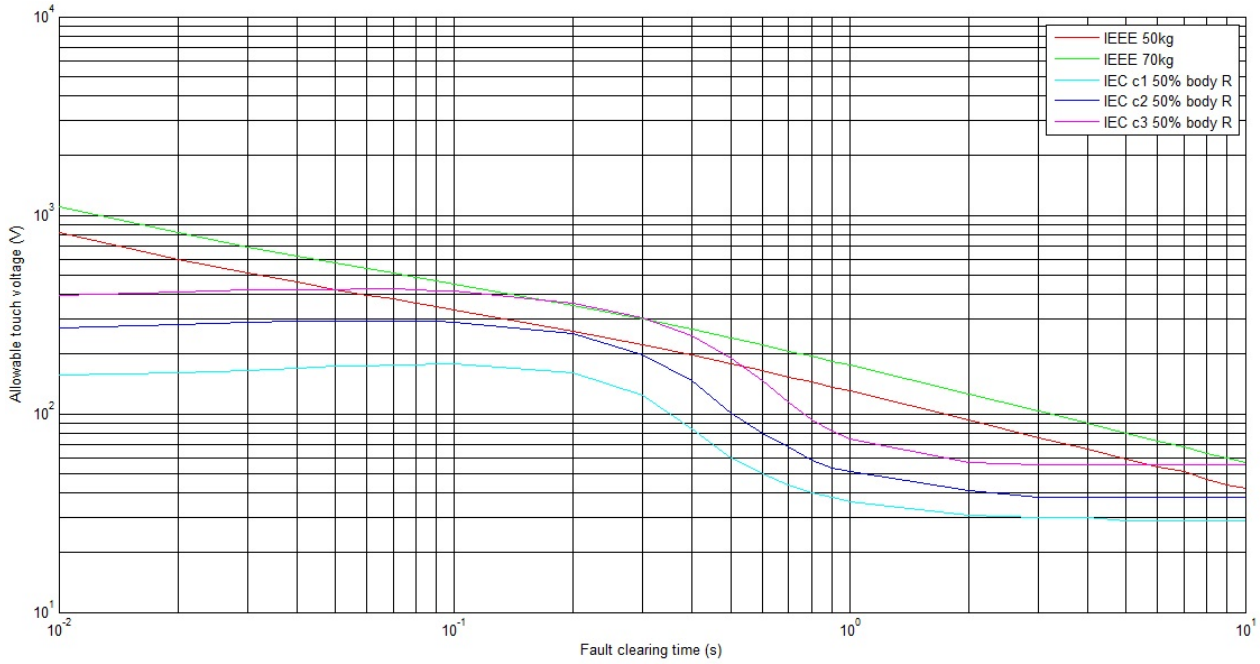

Figure 3.3: Allowable touch voltages for varying the fault clearing times (surface layer resistivity 100 Ωm and top layer soil resistivity 100 Ωm)

Table 3.2: Summary of figure 3.3

Topics	Observations about allowable touch voltages
IEEE	Linear decrease of allowable touch voltage with increased fault clearing time. Higher for 70 kg persons than for 50 kg persons.
IEC	For higher probability of fibrillation allowable touch voltages are increased [30].
Fault clearing time >1 second	All methods converge to virtually the same value
Fault clearing time <0.1 second	Differences between methods are much greater.

3.2.2 Comparison in terms of body resistance

IEEE-80 defines the safety criteria for a given body mass. IEC 60479 states it has been shown that body impedance is not greatly influenced by body mass. In IEC standard, body impedances are given for the 5^{th}, 50^{th} and 95^{th} percentile ranks of the population surveyed. This population consists of the dry, water wet and salt water wet conditions. The body impedance values corresponding to the 5^{th} percentile are the lowest. It is the most conservative from a safety perspective because it results in a higher current value through the body. Figure 3.4 shows the values for the body resistance used by both the standards.

Table 3.3: Summary of figure 3.4

Topics	Observations about body resistances
IEEE	Fixed value of 1000 Ω
IEC	Variable body resistance value. Lower for higher probability of fibrillation.
Fault clearing time >1 second	Body resistance for IEC method is smaller than IEEE.
Fault clearing time <0.1 second	Body resistance for IEC method is smaller than IEEE.

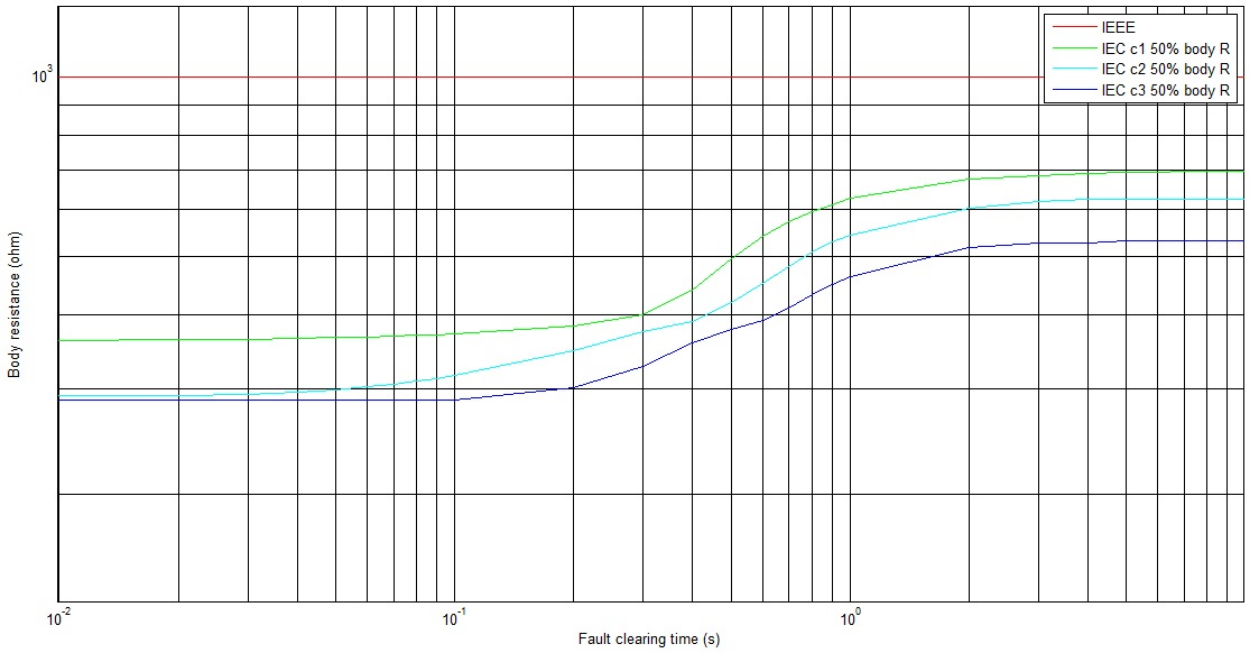

Figure 3.4: Body resistance values (touch voltages) for varying the fault clearing time (surface layer resistivity 100 Ωm and top-layer soil resistivity 100 Ωm)

3.2.3 Comparison in terms of allowable step voltages

Figure 3.5 shows the allowable step voltages for varying the fault clearing times from 0.01 to 10 seconds using both standards.

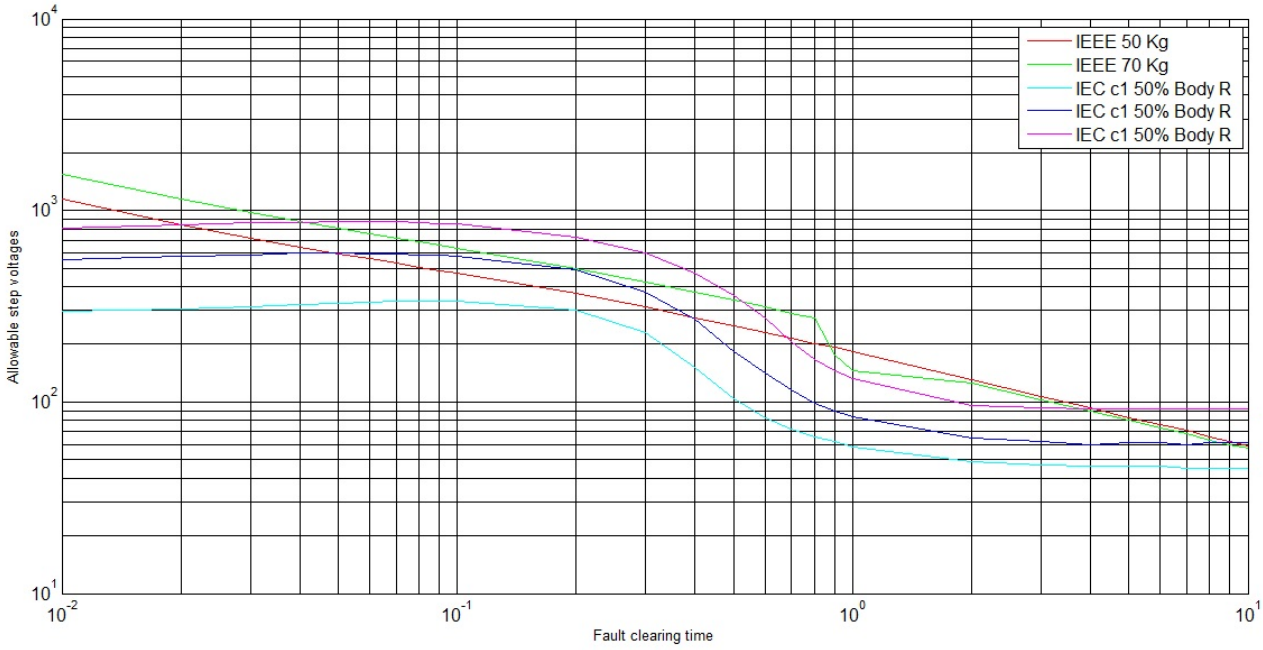

Figure 3.5: Allowable step voltages for varying the fault clearing times (surface layer resistivity 100 Ωm, top layer resistivity 100 Ωm)

Table 3.4: Summary of figure 3.5

Topics	Observations about allowable step voltages
General	At 0.5 seconds fault clearing time, the IEEE-80 70kg method is the safest approach. The IEC c3 50% body resistance method is the next safest approach.

3.2.4 Comparison in terms of surface layer resistivity

A thin layer of surface material is spread in a substation (when the surface material resistivity is greater than the top soil layer resistivity) .It increases the contact resistance between a person's feet and the earth, and can reduce the current through the body considerably. The reduction depends on the relative resistivity of the surface, the top soil layer resistivity and on the thickness of the surface material. Figure 3.6 shows the allowable touch voltages for varying surface layer (i.e. crushed rock or asphalt) resistivity from 100 Ωm (same as top soil layer) to 10,000 Ωm.

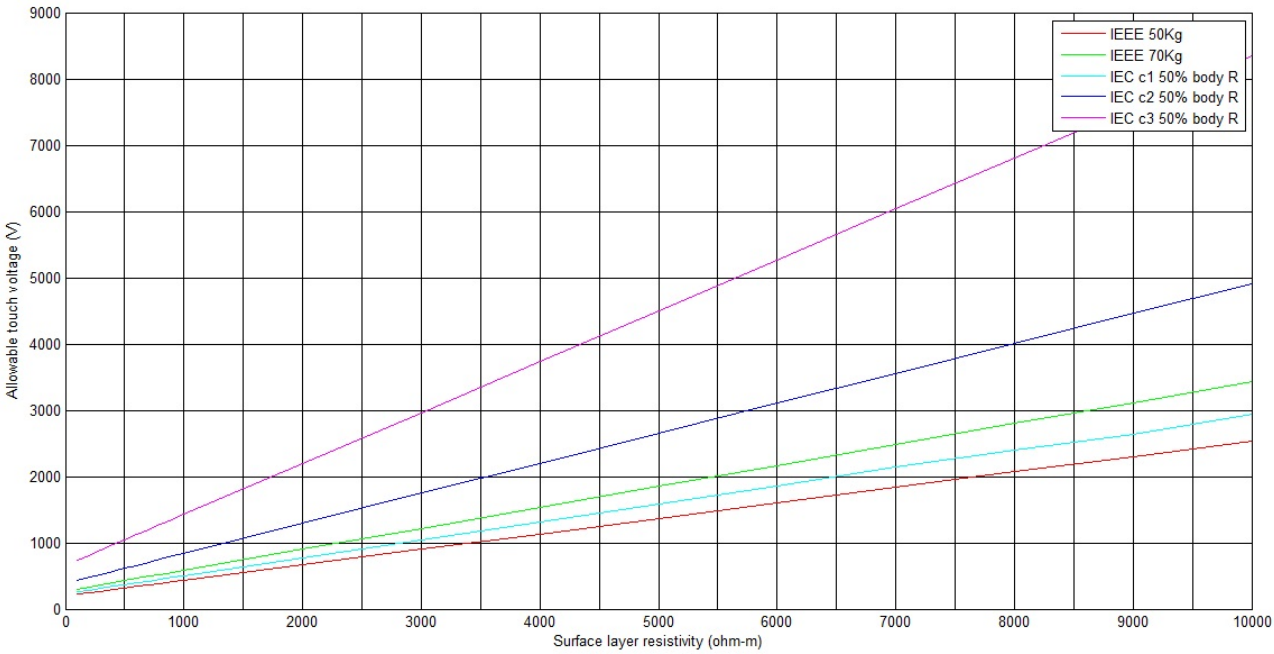

Figure 3.6: Allowable touch voltages for varying surface layer resistivity (top-layer soil resistivity 100 Ωm; surface layer depth 0.15 m; fault clearing time 0.3 s)

Table 3.5: Summary of figure 3.6

Topics	Observations about varying surface layer resistivity
General	Allowable touch voltages increases with increased surface layer resistivity. The IEC c3 50% body resistance method is the safest approach.

3.2.5 Comparison in terms of surface layer depth

Figure 3.7 shows the affect of varying the depth of the surface layer material (from 0.01 to 0.3 m) on allowable touch voltages. Surface layer resistivity is fixed at 3000 Ωm.

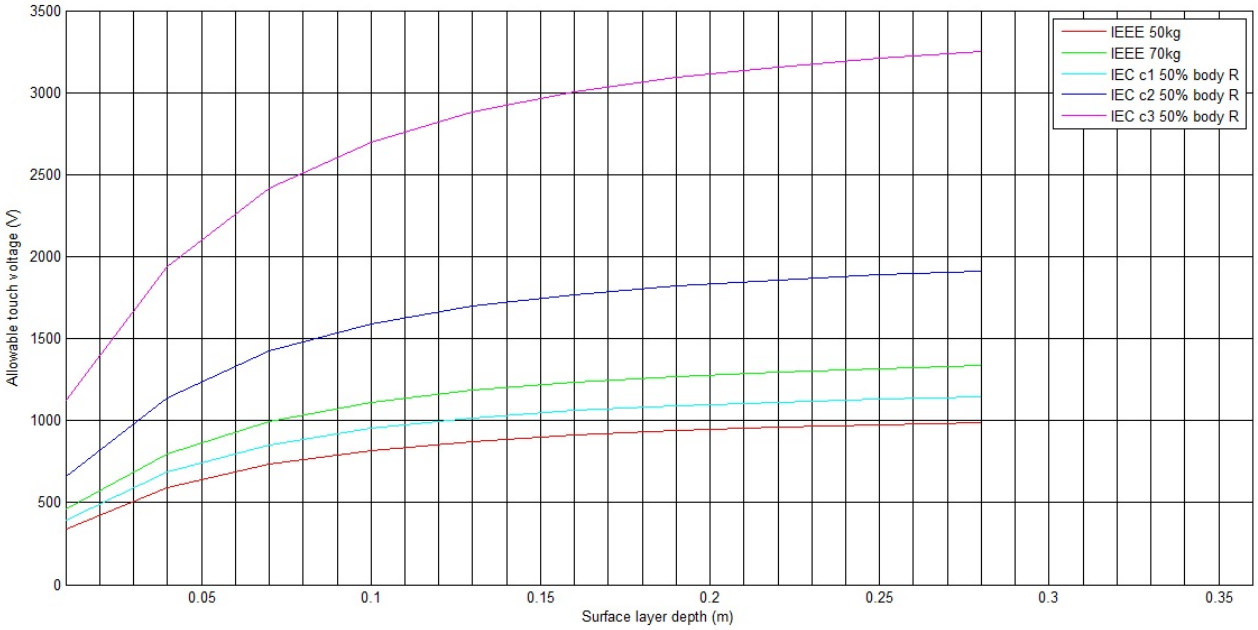

Figure 3.7: Allowable touch voltages for varying surface layer depth (surface layer resistivity 3000 Ωm; top-layer soil resistivity 100 Ωm; fault clearing time 0.3 s)

Table 3.6: Summary of figure 3.7

Topics	Observations about varying surface layer depth
General	Allowable touch voltage increases with greater surface layer depth. The IEC c3 50% body resistance method is the safest approach.

3.2.6 Overall recommendations based on the analysis in section 3

Though the different standards are based on different assumptions but the purpose is the same; i.e., to ensure a safe design of the earth grid. The above case study sets out the importance of evaluating an earth grid design with both the standards to confirm mitigation of the hazards in the substation for any earth fault incident or lightning strike. There was a significant difference in between the allowable voltages determined by the different standards and it varied over the fault clearing time. Safety limit curves can be utilized to identify any potential hazard in the design, and a conservative approach should be taken. A mixed use of the both standards IEEE 80 and IEC 60479 is recommended for evaluating the safety of an earth grid design. It was found in the case study that IEC 60479 was the conservative approach in most of the cases but in some cases IEEE 70 kg model was the conservative one. Subsequently, an earth grid designer will get more flexibility in developing a robust and safe design if both the standards are utilized in assessing the specific design. It can be also implemented to avoid overspending and unnecessary infrastructure setup.

Chapter 4

RELATION BETWEEN THE DEPTH AND THE RESISTANCE OF THE ELECTRODE SYSTEM BURIED IN EARTH

4.1 Theoretical illustration

In most cases, the measurement will show that the resistivity ρ is mainly a function of depth z. For purposes of illustration, we will assume that this function can be written as follows:

$$\rho = f(z) \tag{4.1}$$

In reality, the nature of this function is not simple. Consequently, the interpretation of the measurements will consist of establishing a simple equivalent function of z which gives the best approximation [22]. The equation developed by Schwarz [11] for horizontal buried conductors is as follows:

$$R_G = \frac{\rho}{\pi L}[\ln \frac{2L}{h} + \frac{K_1 L}{\sqrt{A}} - K_2] \tag{4.2}$$

R_G= Resistance of the electrode system
ρ= Resistivity of the soil layer in which the grid is buried
h= Depth of burial
L= Total length of grid conductor
A= Grid area
K_1, K_2= Grid geometry related constant

4.2 Simulation based illustration

4.2.1 For model A

Table 4.1: Soil resistivity profile model A

Layer	Resistivity (Ωm)	Thickness (m)
1	2000	3
2	100	3
3	1000	∞

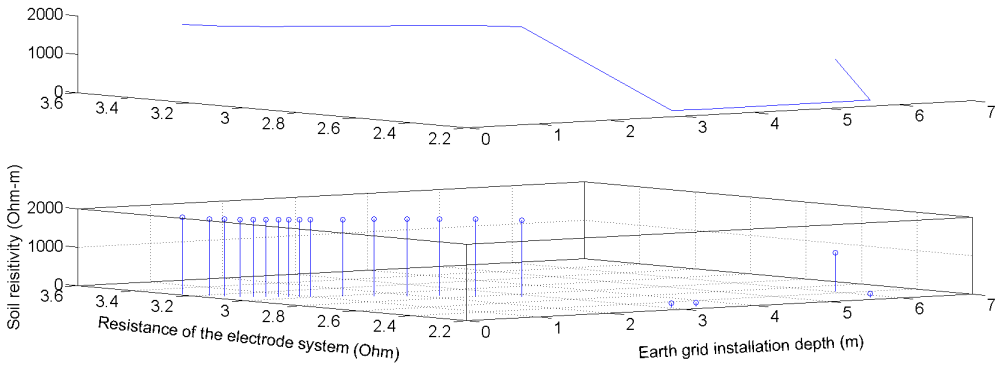

Figure 4.1: Relation between z and R_G for model A simulated in CDEGS

The grid is placed at lower depths progressively. With respect to the grid at 0.1 m the resistance of the electrode system reduces with increased depth. Overall, the resistance of the electrode system is a function of both individual layer resistivity and the respective layer.
Specification of of stranded copper is AWG 4/0 (107 mm^2) and radius of 0.0067056m. Specification of solid copper is AWG 4/0 and radius of 0.005842m is used in the calculations of this chapter.

Table 4.2: For model A in case of stranded copper

Depth of the grid (m)	Resistance of the electrode system(Ω)
0.1	3.25
0.2	3.18
0.3	3.15
0.4	3.12
0.5	3.1
0.6	3.08
0.7	3.06
0.8	3.05
0.9	3.036
1	3.023
1.3	2.9858
1.6	2.95
1.9	2.91
2.2	2.87
2.5	2.82
2.8	2.73
3.1	2.27
3.4	2.2597
5.8	2.257
6.1	2.46

4.2.2 For model B

Table 4.3: Soil resistivity profile model B

Layer	Resistivity (Ωm)	Thickness (m)
1	50	3
2	1000	3
3	100	∞

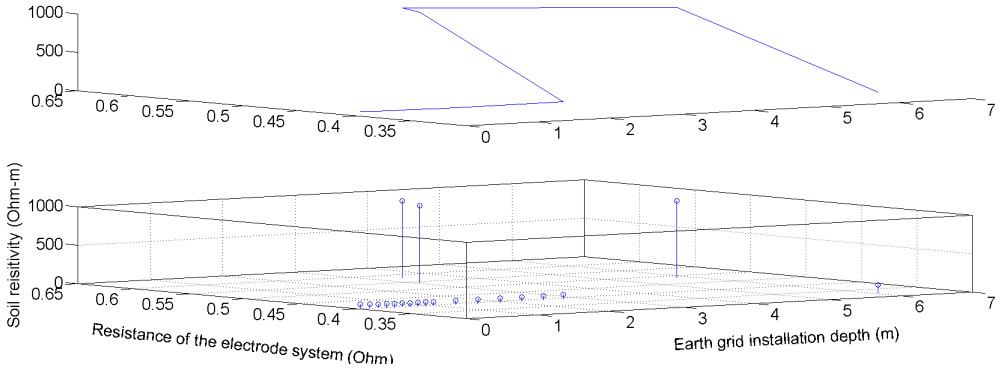

Figure 4.2: Relation between z and R_G for model B simulated in CDEGS

The grid is placed at lower depths progressively. With respect to the grid at 0.1 m the resistance of the electrode system reduces with increased depth up to a depth of around 3 m. But in the high resistivity area, the resistance of the electrode system increased by a significant amount.

The variation in resistance of the electrode system is less in low resistivity soil than in higher resistivity soil.

Table 4.4: For model A in case of stranded copper

Depth of the grid (m)	Resistance of the electrode system(Ω)
0.1	0.40237
0.2	0.40029
0.3	0.39905
0.4	0.3981
0.5	0.3974
0.6	0.3969
0.7	0.3964
0.8	0.3959
0.9	0.3956
1	0.3952
1.3	0.39448
1.6	0.3939
1.9	0.3935
2.2	0.3934
2.5	0.3937
2.8	0.3953
3.1	0.5442
3.4	0.57939
5.8	0.4883
6.1	0.3267

4.2.3 For model C

Table 4.5: Soil resistivity profile model C

Layer	Resistivity (Ωm)	Thickness (m)
1	1000	2
2	750	2
3	500	2
4	250	2
5	150	2
6	100	∞

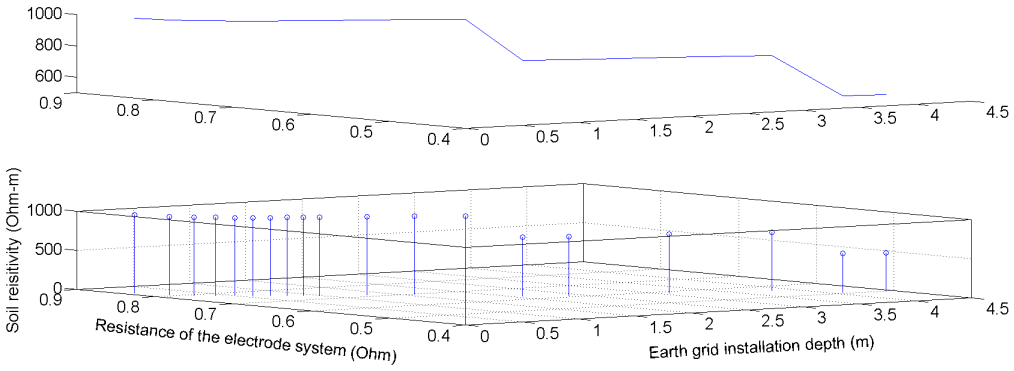

Figure 4.3: Relation between z and R_G for model C simulated in CDEGS

The grid is placed at lower depths progressively. With respect to the grid at 0.1 m the resistance of the electrode system reduces with increased depth. So the deeper the grid is installed, the lower the resistance of the electrode system.

Table 4.6: For model C in case of stranded copper

Depth of the grid (m)	Resistance of the electrode system(Ω)
0.1	0.8404
0.2	0.8106
0.3	0.79289
0.4	0.77993
0.5	0.76952
0.6	0.76066
0.7	0.75281
0.8	0.74565
0.9	0.73898
1	0.73265
1.3	0.71484
1.6	0.69723
1.9	0.67542
2.1	0.63066
2.4	0.61457
3.1	0.58648
3.8	0.55544
4.1	0.50772
4.4	0.4958

4.2.4 For model D

Table 4.7: Soil resistivity profile model D

Layer	Resistivity (Ωm)	Thickness (m)
1	100	2
2	150	2
3	250	2
4	500	2
5	750	2
6	1000	∞

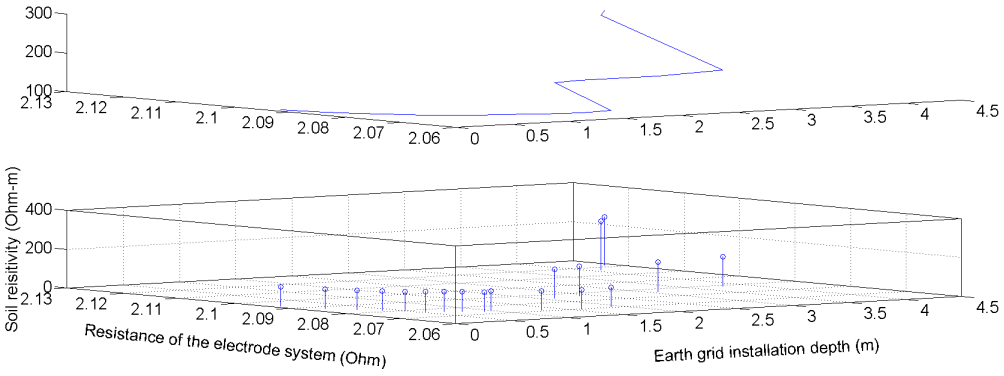

Figure 4.4: Relation between z and R_G for model D simulated in CDEGS

In this soil layer model, resistivity increases gradually with the depth. The grid is placed at lower depths progressively. With respect to the grid at 0.1 m the resistance of the electrode system reduces with increased depth up to 2 m. But when the resistivity increases in deeper soil, the resistance of the electrode system slightly increases and then again it continues to decrease up-to the next layer. So cases with this type of soil profile, the earth grid may be installed at a depth of 0.5 m for optimum performance.

Table 4.8: For model D in case of stranded copper

Depth of the grid (m)	Resistance of the electrode system(Ω)
0.1	2.0935
0.2	2.0875
0.3	2.0838
0.4	2.0813
0.5	2.0792
0.6	2.0776
0.7	2.0762
0.8	2.075
0.9	2.073
1	2.0739
1.3	2.0709
1.6	2.0697
1.9	2.0705
2.1	2.0847
2.4	2.0864
3.1	2.0863
3.8	2.0889
4.1	2.1169
4.4	2.1223

4.3 Discussion

By taking into consideration observations made regarding the above analysis, it will be easier for a designer to decide the earth grid installation depth for optimum performance. Based on the soil profile of the earth grid installation area, the designer can select the optimum earth grid installation depth.

4.4 Simulation studies of conductors in use as earth grid material

In chapter 4 four different soil model is assumed. For each case, resistance of the earth grid is calculated using CDEGS. This simulation was run for solid copper and stranded copper. Resistance of the electrode system is higher for solid copper than for the stranded copper rods. Using the solid copper instead of stranded copper, resistance increase around **0.5% to 4%**

(data is presented below this paragraph). Stranded copper provides a larger effective surface area per unit length of the buried conductor due to the larger conductor radius for the same copper cross section. So reistance of the electrode system is less when the stranded copper is used as the earth grid material.

Table 4.9: For model A in case of solid copper:

Depth of the grid (m)	Resistance of the electrode system(Ω)
0.1	3.2627
0.2	3.2002
0.3	3.1628
0.4	3.1354
0.5	3.1135
0.6	3.0947
0.7	3.0781
0.8	3.063
0.9	3.049
1	3.0357
1.3	2.9985
1.6	2.9629
1.9	2.9268
2.2	2.8872
2.5	2.8378
2.8	2.7524
3.1	2.2724
3.4	2.261
5.8	2.2583
6.1	2.47

Table 4.10: For model B in case of solid copper:

Depth of the grid (m)	Resistance of the electrode system(Ω)
0.1	0.40278
0.2	0.40071
0.3	0.39948
0.4	0.39859
0.5	0.39779
0.6	0.39733
0.7	0.39685
0.8	0.39643
0.9	0.39605
1	0.39572
1.3	0.39492
1.6	0.39434
1.9	0.39397
2.2	0.39386
2.5	0.3942
2.8	0.39575
3.1	0.55031
3.4	0.58538
5.8	0.49422
6.1	0.3274

Table 4.11: For model C in case of solid copper:

Depth of the grid (m)	Resistance of the electrode system(Ω)
0.1	0.8463
0.2	0.81653
0.3	0.79877
0.4	0.78581
0.5	0.77541
0.6	0.76655
0.7	0.7587
0.8	0.75154
0.9	0.74487
1	0.73855
1.3	0.72074
1.6	0.70314
1.9	0.68133
2.1	0.63512
2.4	0.61903
3.1	0.59095
3.8	0.55991
4.1	0.51074
4.4	0.49883

Table 4.12: For model D in case of solid copper:

Depth of the grid (m)	Resistance of the electrode system(Ω)
0.1	2.0947
0.2	2.0887
0.3	2.0851
0.4	2.0825
0.5	2.0805
0.6	2.0788
0.7	2.0775
0.8	2.0763
0.9	2.0752
1	2.0743
1.3	2.0722
1.6	2.071
1.9	2.0718
2.1	2.0865
2.4	2.0882
3.1	2.088
3.8	2.0906
4.1	2.1195
4.4	2.1249

Chapter 5

SOIL RESISTIVITY

In this chapter the effect of different factors in the soil resistivity of a specific area is explained with the aid of a laboratory experiment.

Electrical conduction in soil is essentially electrolytic. For this reason the soil resistivity depends on:

- Moisture content,
- Salt content,
- Temperature,
- Cation exchange capacity (CEC),
- Porosity.

5.1 Effect of temperature on soil resistivity

At temperatures above freezing point the resistivity of soil is relatively uniform. It is the extremes of temperature which markedly affect the resistivity. If the temperature is high enough to force water from the soil or low enough to freeze the water in the pores then the resistivity will change significantly. At moderate temperatures the temperature change is reflected only in the change in the conductivity of the electrolyte in the soil, given by the equation:

$$\rho_T = \frac{\rho_{ref}}{1 + \alpha_t(T_a - T_{ref})} \tag{5.1}$$

where ρ_{ref} is the resistivity measured at a reference temperature,
T_a is the ambient temperature,

α_t is the temperature coefficient of resistivity which for most electrolytes is about 0.025 per degree Celsius

Measurements of soil resistivity at sub-freezing temperature have shown that at -12 degrees Celsius, the resistivity is about 10 to 100 times larger than the resistivity measured at room temperature.

5.2 Effect of moisture content on soil resistivity

The resistivity of most soils rises abruptly whenever the moisture content accounts for less than 15% of the soil weight. The amount of water present depends on the grain size, compactness and variability of the grain size that comprise the soil. Fine grained soils and rocks hold more water than coarse grained. Once the moisture content exceeds about 22% the resistivity is not significantly affected [31].
For accuracy within an order of magnitude, Hummel's empirical formula is useful in estimating the resistivity of soils which conduct electricity by the electrolytic process:

$$\rho_s = \frac{1.5}{C} - 0.5\rho_w \tag{5.2}$$

where ρ_s is the soil resistivity, C is the relative volume of water contained in soil, ρ_w is the water resistivity.

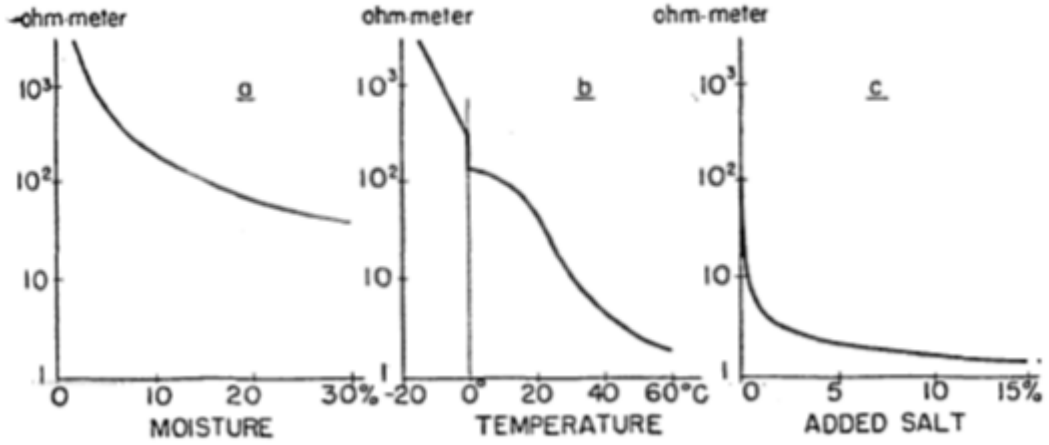

Figure 5.1: Effect on soil resistivity of (a) moisture (b) temperature (c) added salt [23]

Conduction of current in the soil is mostly electrolytic. So it follows that the quantity of water and the nature and amount of dissolved salts play an important part in determining the soil resistivity. The amount of water varies with the weather, the time of year, the nature of the sub soil and the depth of the permanent water table (if any). Except for desert soil, the soil is seldom dry. On the other hand, soil with a moisture content greater than 40% does not occur very often.

MaCollum and Logan started an experiment with 5% moisture oven dried red clay soil with a resistivity of 2.34 x10^2 $\Omega - m$. The moisture content was increased to 22% and the resistivity dropped to 68 $\Omega - m$. In some other experiments with different soil samples, the moisture content was increased and as a result, the resistivity decreased drastically. But above of 14-18% moisture content, the rate of resistivity decrease lessens.

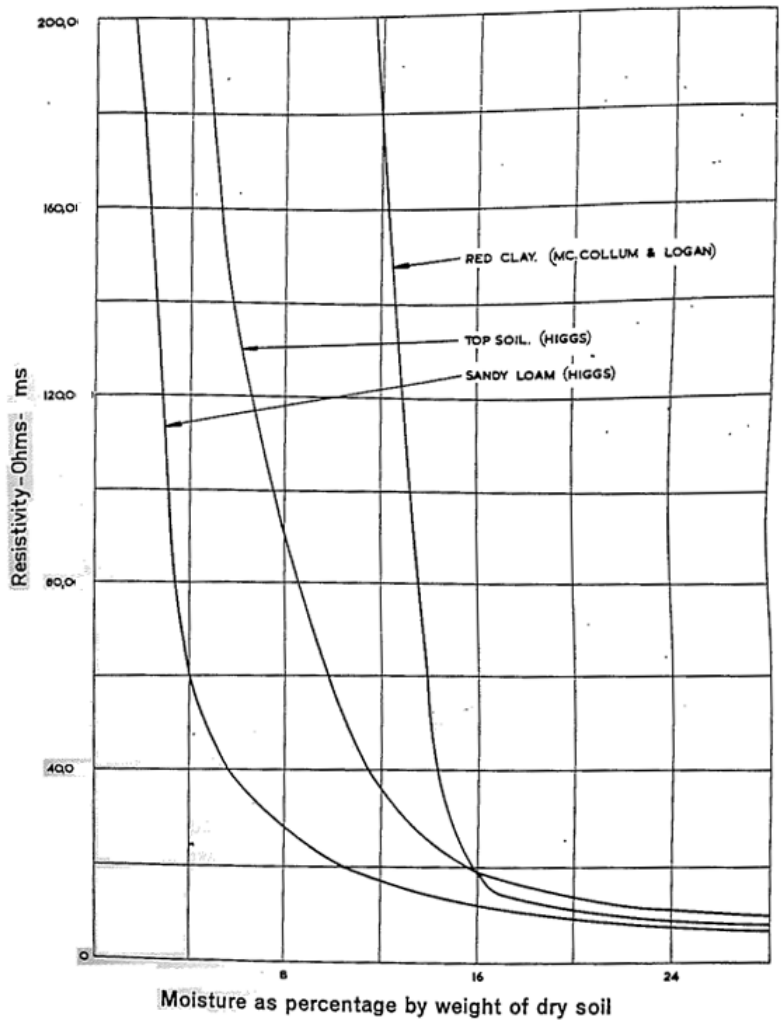

Figure 5.2: Effect of Moisture content and dissolved salts in the water [12]

5.3 Soil resistivity measurement in the laboratory

Soil resistivity can be measured in a device called the soil box. If it is inappropriate for some reason to carry out field surveys or a soil sample requires additional chemical testing in the laboratory, a quantity of soil may be taken from the field. The soil box is filled with the soil and the box is set up in the correct position for direct Wenner measurement. The resistivity test is

done using the same principle as the Wenner four pin method. The current is driven through the two outer points and the voltage drop is measured across the two inner points. The equation for the resistivity calculation is as follows:

$$\rho = \frac{RWD}{L} \tag{5.3}$$

where W, D and L are the soil box dimensions, and R is the resistance.

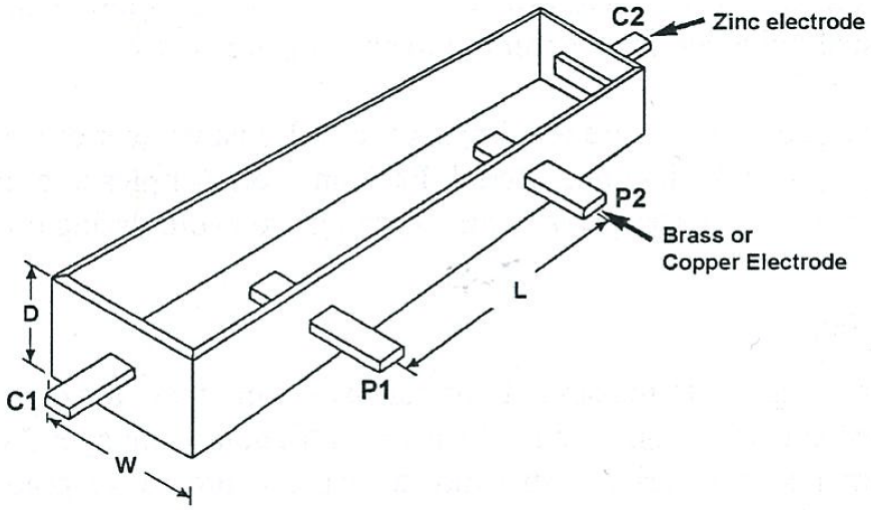

Figure 5.3: Soil box of soil resistivity measurement in the laboratory [32]

5.3.1 Test procedure

Soil samples were taken from two different locations, and soil moisture content was measured according to AS 1289.2.1.4. Then soil resistivity was measured in the soil box following the standard AS 1289.4.4.1. Then water was added proportionally to the mass of dry soil to get an idea of the soil resistivity during the rainy season and flood conditions. Applied soil moisture content levels to the soil samples were decided accordingly to soil science procedures. Soil resistivity was measured with the changed moisture content level.

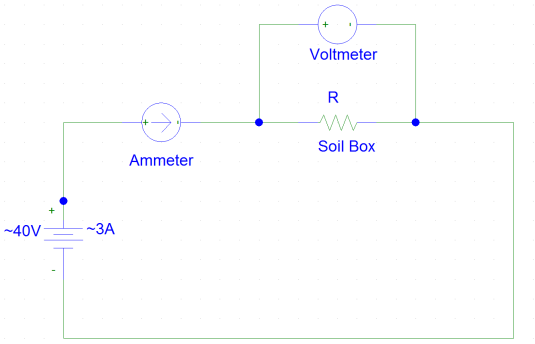

Figure 5.4: Circuit diagram of the soil mositure content measurement in PSPICE

Figure 5.5: Soil sample is dried in the oven determine soil moisture content

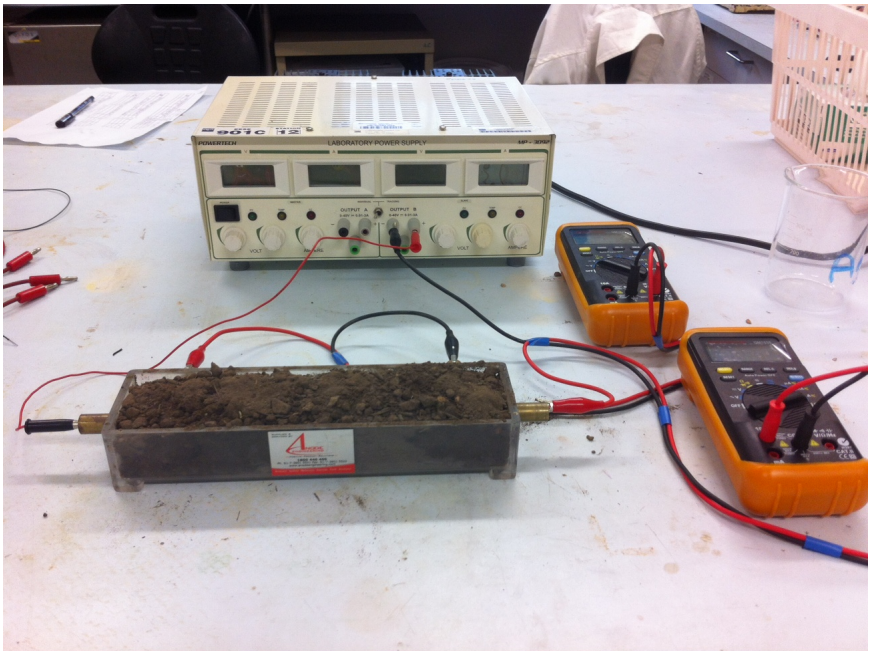

Figure 5.6: Soil resistivity measurement in the laboratory

5.3.2 Results and discussion

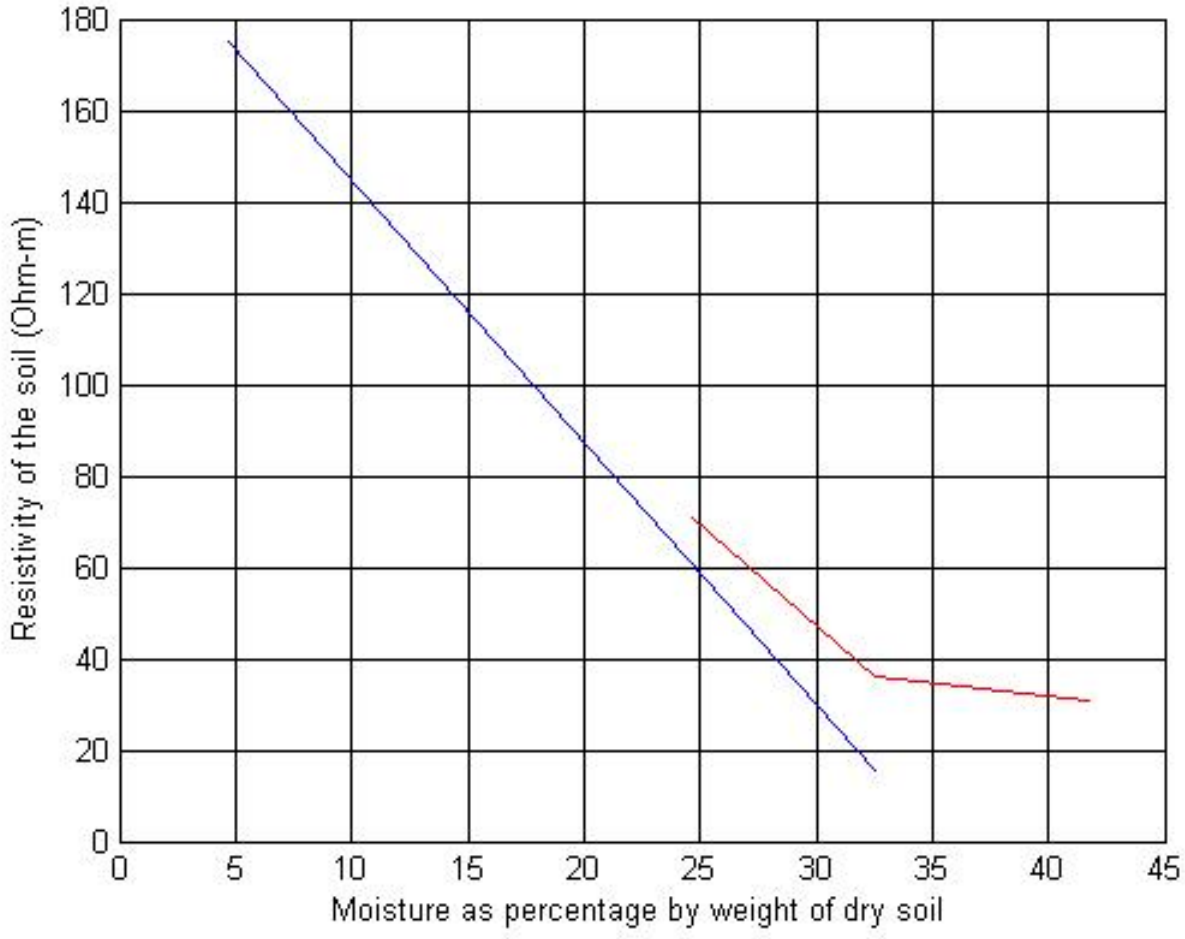

Figure 5.7: Change in soil resistivity with the increase in soil moisture content in the laboratory test

Figure 5.7 resembles figure 5.2, so the emperical formula 5.2 is not required. This formula could be utilized to predict the resistivity of **any** type of soil with any type of soil moisture content level. A soil model utilizing figure 5.2 could give an idea of soil resistivity in the rainy season or in flood conditions. This may lead to changes in design specifications for increasedsafety inside and outside the substation.

Chapter 6

GRAPHENE COATING ON CONDUCTORS

This chapter investigates graphene deposition and characterization techniques on the surface of bulk copper conductors.

6.1 Graphene as a prospective earth grid conductor coating

A great many scientific activities were initiated after the publication in 2004 of a method to prepare free-standing graphene. Graphene was found to be a single 2D carbon sheet with the same structure as the individual layers in graphite [4–8]. Graphene is a rapidly rising star on the horizon of materials science and condensed-matter physics. This strictly two-dimensional material exhibits exceptionally high crystal and electronic qualities. Despite its short history under scientific investigation it has already revealed a cornucopia of new physics and potential applications.

Graphene is the name given to a single layer of carbon atoms densely packed into a benzene-ring structure. It is widely used to describe the properties of many carbon based materials, including graphite, large fullerenes, nanotubes, etc. (e.g. carbon nanotubes are usually thought of as graphene sheets rolled up into nanometer-sized cylinders). The planar graphene itself had been presumed not to exist in the free state. In the past few years many fascinating properties have been discovered through the investigation of pristine graphene including extremely high charge (electrons and holes) mobility (230,000 cm^2/Vs), thermal conductivity (3000 W/mK), and the highest strength (130 GPa) and the highest theoretical specific surface area

(2600 m^2/g) in comparison to any other thin films.

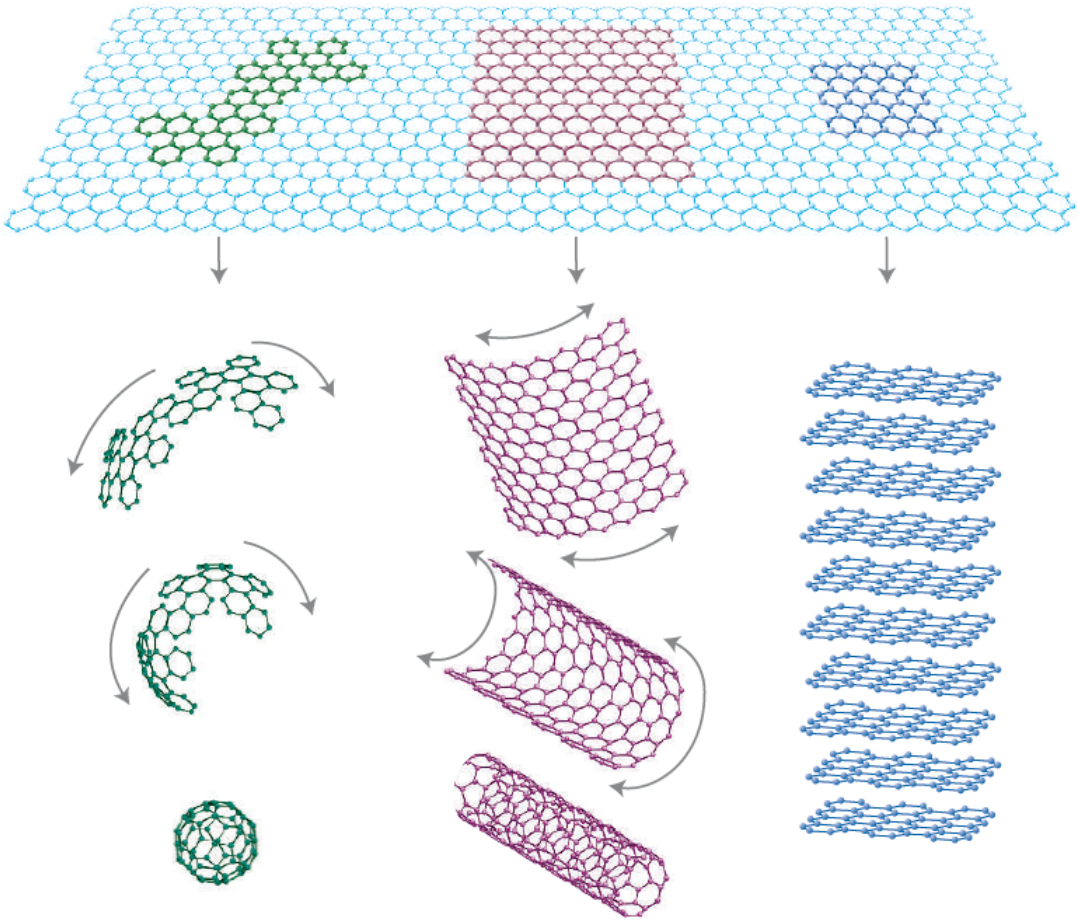

Figure 6.1: Origin of all graphitic forms. Graphene is a 2D building material for carbon materials of all other dimensionalities. It can be wrapped up into 0D buckyballs, rolled into 1D nanotubes or stacked into 3D graphite [7]

6.1.1 Structure of graphene

Pristine graphene, a two-dimensional honeycomb carbon lattice is a zero gap semiconductor. The sp^2 hybridized carbon atoms are arranged in hexagonal fashion in a 2-dimensional layer. A single hexagonal ring comprises of three strong in-plane sigma bonds (face-to-face overlapping of electronic orbitals) P_z orbitals perpendicular to the planes. Different graphene layers

are bonded by the weak P_z interaction while strong in-plane bonds keep the hexagonal structure stable. This facilitates the de-lamination of the 3D structure (graphite) into the individual graphene sheet just by applying mechanical stress [3].

One of the most interesting aspects of graphene is its highly unusual nature of charge carriers, which behave as massless relativistic particles (Dirac fermions). Its charge carriers are considered as electrons that have lost their rest mass. The Dirac fermion's behaviour is very abnormal compared to the electrons when subjected to the magnetic fields.

The band structure of single layer graphene exhibits two bands intersecting at two inequivalent points K and K^0 in the reciprocal space. Near these points electronic dispersion resembles that of the relativistic Dirac electrons. K and K^0 are referred as Dirac points where valence and conduction bands are degenerated, making graphene a zero band gap semiconductor (Figure 6.2).

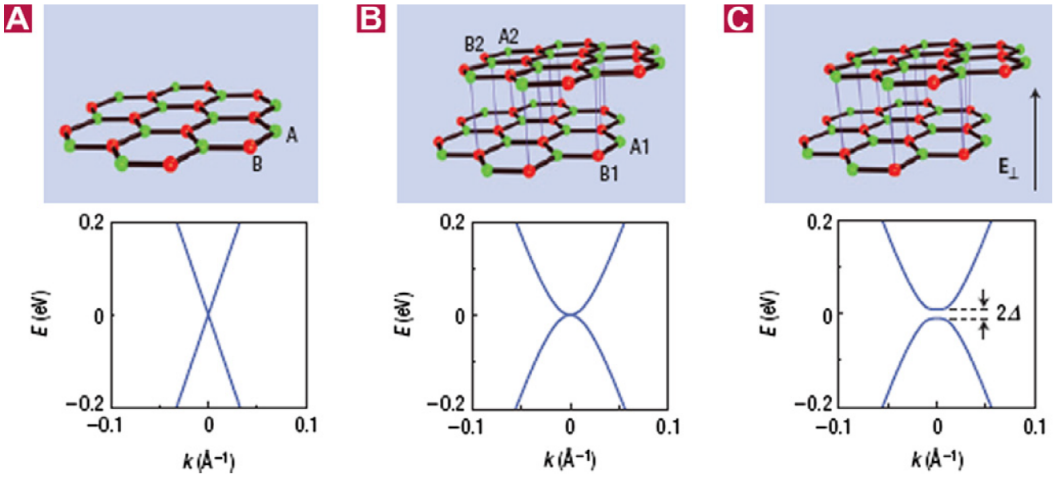

Figure 6.2: Bandgap in the graphene. The schematic diagrams of the lattice structure of (A) monolayer and (B) bilayer graphene. The green and red coloured lattice sites indicate the A (A1/A2) and B (B1/B2) atoms of the mono-layer and bilayer graphene, respectively. The diagrams represent the calculated energy dispersion relations in the low-energy regime, and show that the mono-layer and the bilayer graphene are zero-gap semiconductors. (C) When an electric field (E) is applied perpendicular to the bilayer, a band gap is opened in the bilayer graphene, whose size (2D) is tunable by the electric field [3]

6.1.2 Electrical properties

In early experiments, graphene films of a few layers could be prepared up to 10^{-6}m thickness. This was the thinnest possible deposition of graphene layers on any substrate. Films were prepared up to 10^{-5} m thick while still being visible to the naked eye [4]. Despite being atomically thin, the films are of high quality so the 2D electronic transport is ballistic at submicrometer distances. Graphene is the most conductive thin film reported to date.

The high electronic conductivity in a single layer is due to the very high quality, i.e. low defect density of its crystal lattice. Defects in general act as scattering sites and inhibit charge transport by limiting the electron mean free path. There is evidence that pristine graphene is defect free [3].

Bilayer graphene also shows remarkable performance as conductor. Unlike some traditional metals, even at a lower temperature (e.g. liquid helium

temperatures) it remained metallic.

6.1.3 Semiconductor-like properties

Graphene's quality clearly reveals itself in a pronounced ambipolar electric field effect (Figure 6.3). The charge carriers can be tuned continuously between the electrons and holes in concentrations as high as 10^{13} cm^{-2} and their mobilities μ can exceed 15,000 cm^2 V^{-1} s^{-1} even under ambient conditions. Moreover, the observed mobilities weakly depend on temperature T, which means that μ at 300 K is still limited by impurity scattering, and therefore can be improved significantly, perhaps, even up to 100,000 cm^2 V^{-1} s^{-1}. Although some semiconductors exhibit room temperature μ as high as 77,000 cm^2 V^{-1} s^{-1} (namely, InSb), those values are quoted for undoped bulk semiconductors. In graphene, μ remains high even at high n ($>10^{12}$ cm^{-2}) in both electrically and chemically doped devices, which translates into ballistic transport on the sub-micrometre scale (currently up to 0.3 μ at 300 K). A further indication of the system's extreme electronic quality is the quantum Hall effect (QHE) that can be observed in graphene even at room temperature, extending the previous temperature range for the QHE by a factor of 10 [7].

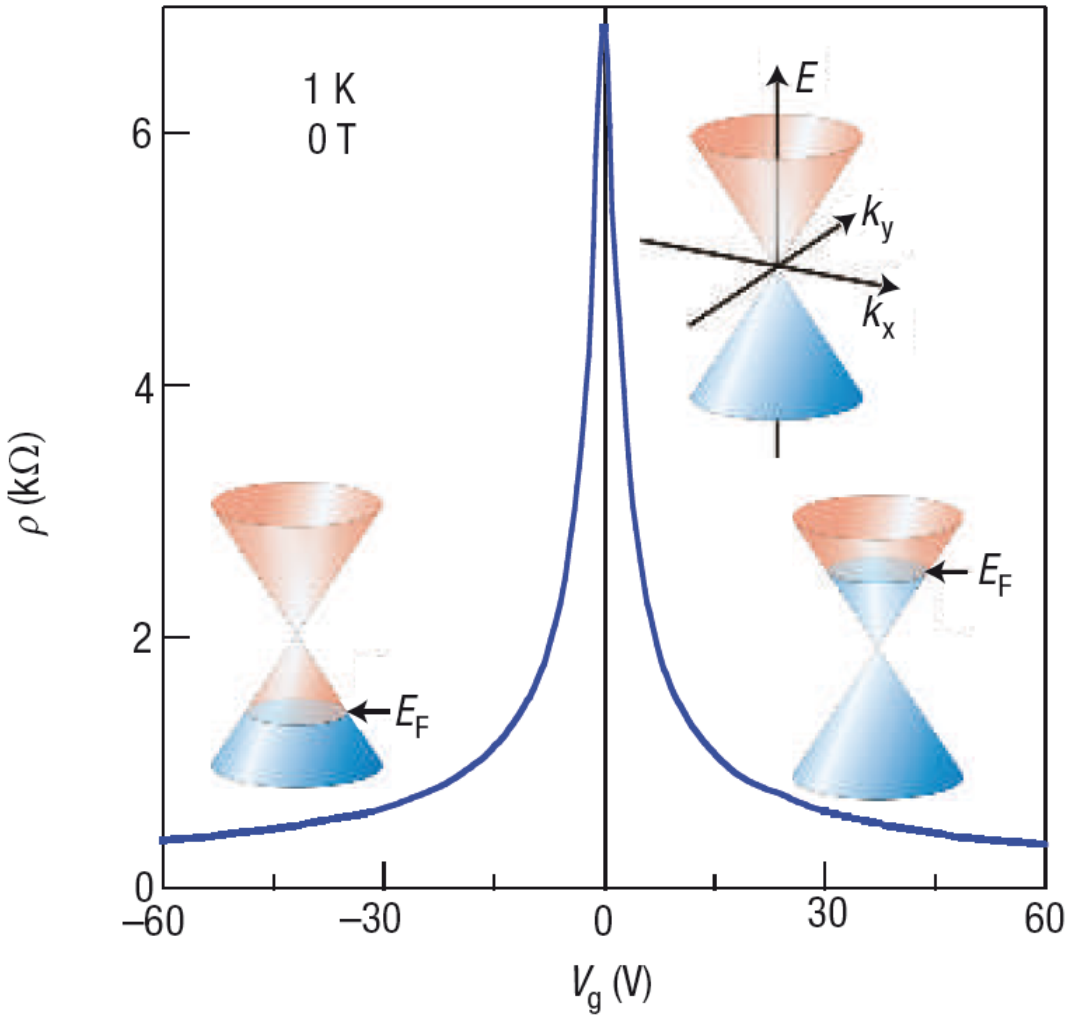

Figure 6.3: Ambipolar electric field effect in single-layer graphene. The insets show its conical low-energy spectrum E(k), indicating changes in the position of the Fermi energy E_F with changing gate voltage V_g. Positive (negative) V_g induces electrons (holes) in concentrations $n = \alpha V_g$ where the coefficient α=7.2 X 10^{10} cm^{-2} V^{-1} for field-effect devices with a 300 nm SiO_2 layer used as a dielectric. The rapid decrease in resistivity ρ on adding charge carriers indicates their high mobility (in this case, μ=5,000 cm^2 V^{-1} s^{-1} and does not noticeably change with increasing temperature to 300 K) [7]

Another important characteristic of single layer graphene is its ambipolar electric field effect at room temperature, that is charge carriers can be tuned between electrons and holes by applying a required gate voltage. In positive

gate bias the Fermi level rise above the Dirac point which promote electrons to populate into conduction band, whereas, in negative gate bias the Fermi level drop below the Dirac point promoting the holes in the valence band in concentrations of $n = \alpha V_g$.

6.1.4 Graphene-metal interface

Distance between graphene and metal surface

If the graphene is physisorbed one would expect the distance between the graphene and the metal surface to be comparable to the layer spacing of 3.35Åin bulk graphite. Most data exist for the (1X1) structure of graphene on Ni(111), which, of course, is much more easily accessible than the systems with the large moir unit cells. Figure 6.4 shows the result of a LEED-I(V) [low energy electron diffraction] analysis of graphene on Ni(111) [8].

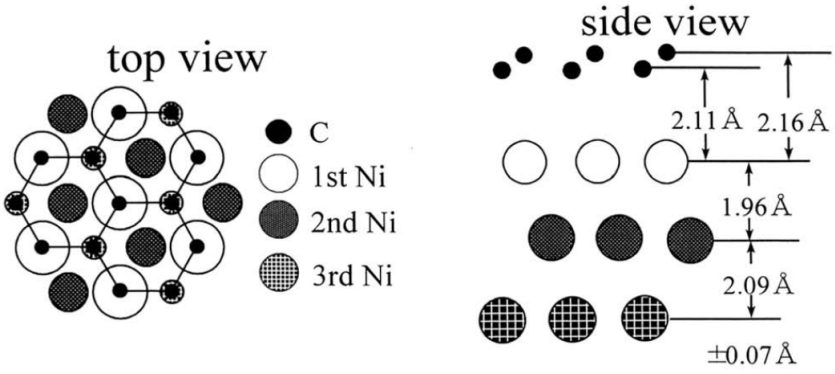

Figure 6.4: Top view and side view of the (1X1) structure of graphene on Ni(111) [8]

Previous models with both C atoms in hollow sites (fcc/hcp configuration) seem to have been ruled out. The vertical positions are 2.11 and 2.16Å. A distance of 2.1Åwas confirmed in an ion scattering analysis and in several Density functional theory (DFT) calculations values between 2.0 and 2.1Åwere found.

6.1.5 Prospect of good performance in soil environment

A characteristic property of bulk graphite is its inertness with respect to oxidation and other chemical reactions, which seems to hold for monolayer graphene, too. The bonding to metal surfaces does not lift this stability. Graphene on Ru(0001) can be exposed to air without affecting the moiré structure. In addition to this, a graphene layer can passivate the underlying metal surface. From the experiments of J. Wintterlin and M.L. Bocquet [8] it was evident that the graphene protects the surface from oxidation. This protection effect could also be confirmed for an intercalated Fe layer between the Ni(111) surface and the graphene overlayer.

6.1.6 Summary (Why graphene)

Generally copper conductors are used as earth grid conductors, a practice that has been in place since power system earthing was first implemented. The earth grid is installed for the designed lifetime of the substation. Over time more power sources are added to the electrical grid system which increases the magnitude of the prospective fault current. Consequently, the earth grids may not be able to function as planned if the prospective fault current exceeds the original design limit. Additional factors that may compromise the safe operation of an earth grid include significant changes in the soil and corrosion of the earth grid conductors leading to an overall decrease in the conductivity. As a potential solution to these circumstances, graphene coated copper conductors were investigated with the aim to both increase conductor conductivity and reduce corrosion of the conductor rods.

Despite being atomically thin the graphene remains high in quality. Its unique property is that other than the graphene no other film is even poorly metallic under ambient conditions. It is assumed that the graphene layers on the metal surfaces represent the most perfect over-layers known in surface science [8]. In addition to this the graphene shows no transition to the insulator state down to the temperature of liquid helium. Their small size (much less than 1 mm) and strong inter-atomic bonds ensure that the thermal fluctuations cannot lead to the generation of dislocations or other crystal defects even at a elevated temperature [7]. In addition, a truly exceptional feature of the graphene is that μ (charge mobility) remains high even at the highest electric field induced concentration. Bunch et al [33] have shown that the graphene membrane can be impermeable to the standard gases including helium. In the most recent reporting by R.K.S. Raman

et al. [34] it was evident that the graphene coating prevents electrochemical degradation. It was shown that the corrosion resistance (arithmetical sum of metal/electrolyte interface resistance and surface coating resistance pore resistance) of a graphene coated specimen is 1.5 orders of magnitude higher than an uncoated copper specimen. Graphene as an anti corrosion coating has been identified as promising in many publications [34–36].

Graphene has a hydrophobic nature. It prevents hydrogen bonding with water [37]. Graphene is inert with respect to oxidation and other chemical reactions. Given that corrosion in the soil is basically an oxidation/chemical reaction. It is expected that graphene will not corrode in the soil. It also gives an indication that graphene might perform well under the impulse condition.

That is why a graphenel coating has the potential to inhibit corrosion without sacrificing conductivity.

6.2 Deposition and characterisation technique

At present, there is no pathway for the formation of a graphene layer that can be exfoliated from or transferred from the graphene synthesized on SiC, but there is a way to grow and transfer graphene grown on metal substrates. Although graphene has been grown on a number of metals, we still have the challenge of growing large-area graphene [38]. In our experiment graphene was grown on a cylindrical conductor covering a large surface area ($5.74\text{x}10^{-3}\text{m}^2$). As we were able to grow graphene on the desired substrates, no thin film transfer process was required before using these substrates in power systems applications.

Technique described by Yao et al. [39] was used as the starting point for developing the graphene deposition technique on bulk cylindrical copper conductors. Working procedures and characterisation of the number of layers is explained in the following sections.

Figure 6.5: Experimental setup for the process of graphene deposition on copper process

6.2.1 Graphene deposition on copper

For doing scale model test for evaluating earthing performance of graphene coated conductors, it was planned to grow graphene thin films on bulk copper substrates (0.14 m long and 0.00625 m radius). But it is difficult to characterize the surface of such big samples because it is not convenient to focus on samples of such big radius with the characterizing instruments (Raman microscope and Scanning electron microscope). So for ease of characterization initially hemispherical samples of 0.01m long and radius of 0.003 m (approximate) was taken for running the experiments. Then after finding the proper recipe of growing graphene on hemispherical copper substrates, experiments were run on 0.14m long samples and those samples are assumed to have same surface characteristics as the hemispherical conductors have.

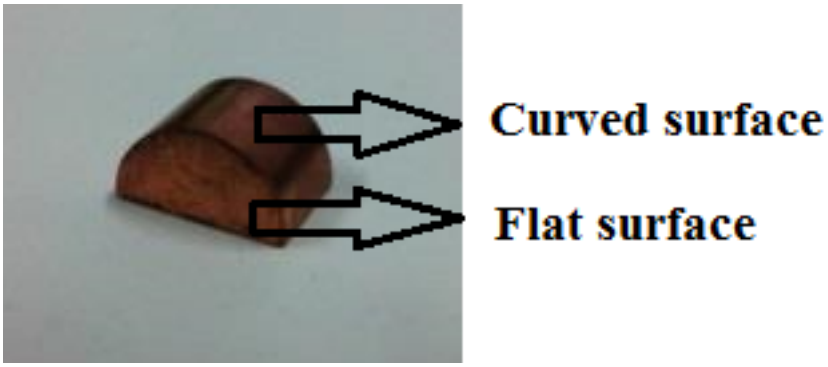

Figure 6.6: Hemispherical substrate

At first hemispherical conductors were used. Ultrasonication was used to clean these substrates, first with propan-2-ol and then with distilled water. For each, the duration of ultrasonication was 5 minutes. The substrates were then placed in a tube furnace which was heated to a temperature of 975^{o}C. Argon gas at 100 standard cubic centimetres per minute (SCCM) was then allowed to flow. An initial annealing of the metal substrate was carried out by flowing 500 SCCM H_2 for 20 minutes at 975^{o}C in order to recover a pure metal surface. Then a gas mixture of a carbon source (methane gas was used in this experiment) and H_2 was introduced into the furnace. Duration of methane gas flow was 3 minutes in the first experiment. As that deposition did not result in graphene film on the substrates, duration of gas flow was increased to 5 minutes. Finally it was increased to 10 minutes. Methane gas flow rate was 6 SCCM in the first experiment. As this experiment did not result in graphene thin film growth on copper surface, methane gas flow was gradually increased in the later experiments. In all these experiments, during deposition phase of the experiment 500 SCCM of Hydrogen gas flowed into the furnace. After completion of the growth, the carbon source supply was stopped and the furnace was cooled down to room temperature by flowing 200 SCCM Ar and 100 SCCM H_2 with a cooling rate of 10^{o}C /minute. After being unable to grow graphene films on copper surface with a certain recipe, an electro-polished sample was also used in the experiment using the same recipe to understand the effect of surface roughness in this deposition process.

After finally gaining graphene films on top of the hemispherical samples, copper rods of 0.05 m diameter were used. Ultrasonication was used to clean these substrates, first with propan-2-ol and then with distilled water. For each, the duration of ultrasonication was 5 minutes. The substrates were then placed in a tube furnace which was heated to a temperature of 975^{o}C.

Argon gas at 100 standard cubic centimetres per minute (SCCM) was then allowed to flow. An initial annealing of the metal substrate was carried out by flowing 500 SCCM H_2 for 20 minutes at 975^{o}C in order to recover a pure metal surface. Then a gas mixture of a carbon source (methane gas was used in this experiment) and H_2 was introduced into the furnace. The graphene film growth time was 10 minutes and during this time 30 SCCM methane and 500 SCCM of Hydrogen gas flowed into the furnace. After completion of the growth, the carbon source supply was stopped and the furnace was cooled down to room temperature by flowing 200 SCCM Argon and 100 SCCM H_2 with a cooling rate of 10^{o}C /minute. For getting better control over the deposition process, an increased temperature of 1000^{o}C was also applied during the experiment. But it did not enhance the quality of deposited graphene film on copper surface. Rather it caused reduced quality of thin film growth.

6.2.2 Characterisation of the graphene deposition on copper

Various instruments were used to observe the morphology and homogeneity of the produced graphene films. These are described in the following sections:

Graphene existance identification with Raman spectroscopy

Raman spectroscopy (named after Sir C. V. Raman) is a spectroscopic technique used to observe vibrational, rotational, and other low-frequency modes in a system. It relies on inelastic scattering, or Raman scattering, of monochromatic light, usually from a laser in the visible, near infrared, or near ultraviolet range. The laser light interacts with molecular vibrations, phonons or other excitations in the system, resulting in the energy of the laser photons being shifted up or down. The shift in energy gives information about the vibrational modes in the system. Raman spectroscopy is commonly used to identify molecules present in a specific surface. Typically, a sample is illuminated with a laser beam. Electromagnetic radiation from the illuminated spot is collected with a lens and sent through a monochromator. Elastic scattered radiation at the wavelength corresponding to the laser line (Rayleigh scattering) is filtered out, while the rest of the collected light is dispersed onto a detector by either a notch filter or a band pass filter. Spontaneous Raman scattering is typically very weak, and as a result the main difficulty of Raman spectroscopy is separating the weak inelastically scattered light from the intense Rayleigh scattered laser light. Historically, Raman spectrometers used holographic gratings and multiple dispersion stages to achieve a high degree of laser rejection. In the past, photomultipliers were the detectors of

choice for dispersive Raman setups, which resulted in long acquisition times. However, modern instrumentation almost universally employs notch or edge filters for laser rejection and spectrographs either axial transmissive (AT), CzernyTurner (CT) monochromator, or FT (Fourier transform spectroscopy based), and CCD detectors [40]. Diffraction grating disperses light onto the detector to generate a spectrum. Then the spectrum gives information about the molecular bonding.

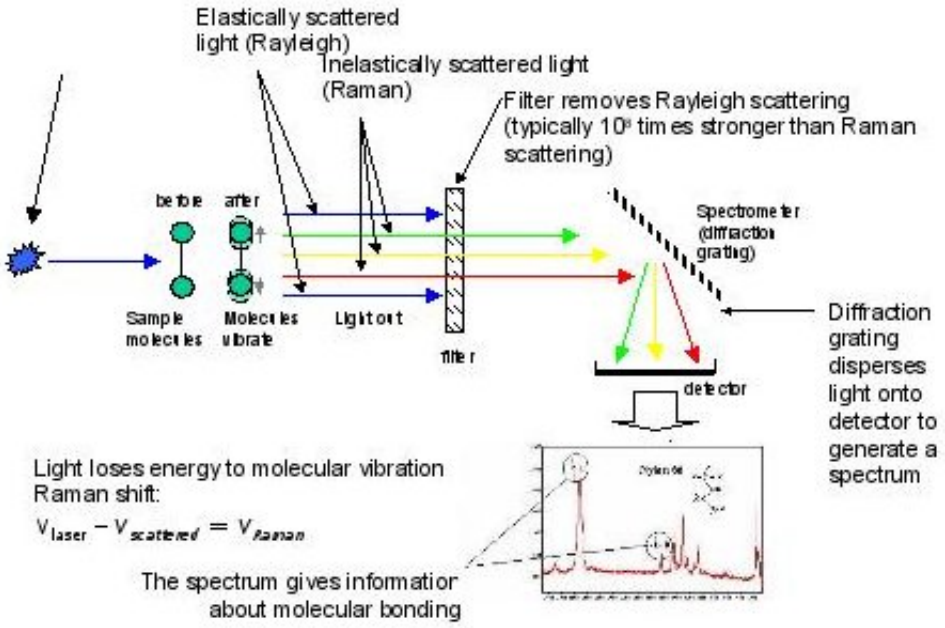

Figure 6.7: Principle of raman spectroscopy [41]

The Raman spectroscopy measurements were performed at room temperature with a Renishaw spectrometer. The wavelength of the excitation of the laser used was 785 nm. A 50X objective (zoom) was used. Raman spectroscopy was analysed at different random points of the curved surface and the flat surface of the conductor. One Raman spectroscopic analysis result from each surface is presented in this section.

The Raman spectroscopy allows unambiguous, high-throughput, nondestruc-

tive identification of the graphene layers. The two most intense features of the Raman spectroscopy of graphene are the G peak at 1580 cm^{-1} and G′ peak at 2700 cm^{-1}. G′ peak is the second most prominent peak always observed in the graphite samples [42]. In addition to these two major peaks, a weaker D band is also observed at 1350 cm^{-1} in most of the scanned areas. This peak is due to the disorder or defect in the perfect graphite; such as edges, point defects and subdomain boundaries [39]. It indicates that the graphene deposited on the copper substrate is not continuous throughout the surface or not uniform.

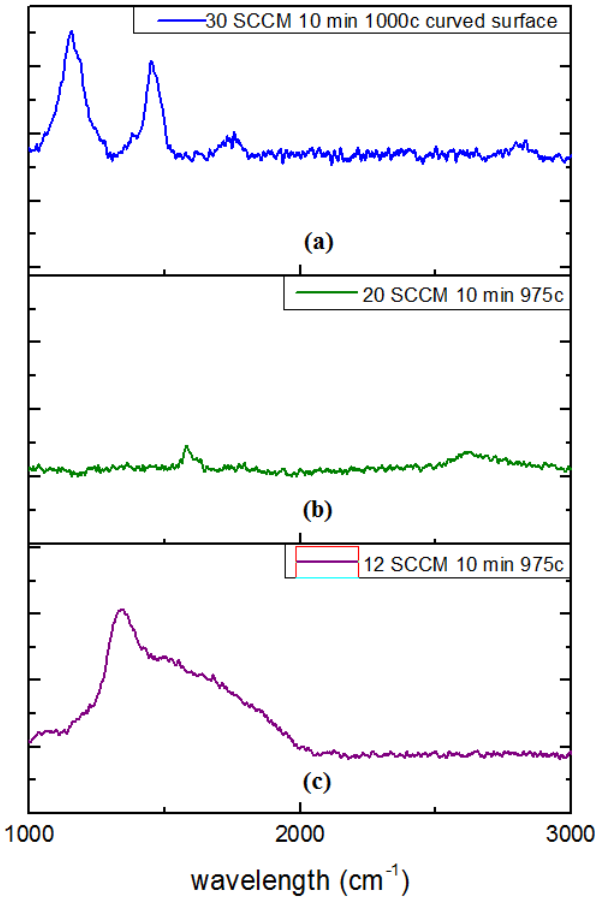

Figure 6.8: Raman spectra at (a) 30 SCCM methane gas flow at 1000^{o}C, (b) 20 SCCM methane gas flow at 975^{o}C, and (c) 12 SCCM methane gas flow at 974^{o}C. Deposition time for all these experiments were 10 minutes and all of these were failed attempts to grow graphene on cylindrical copper rod surface (785 nm excitation laser).

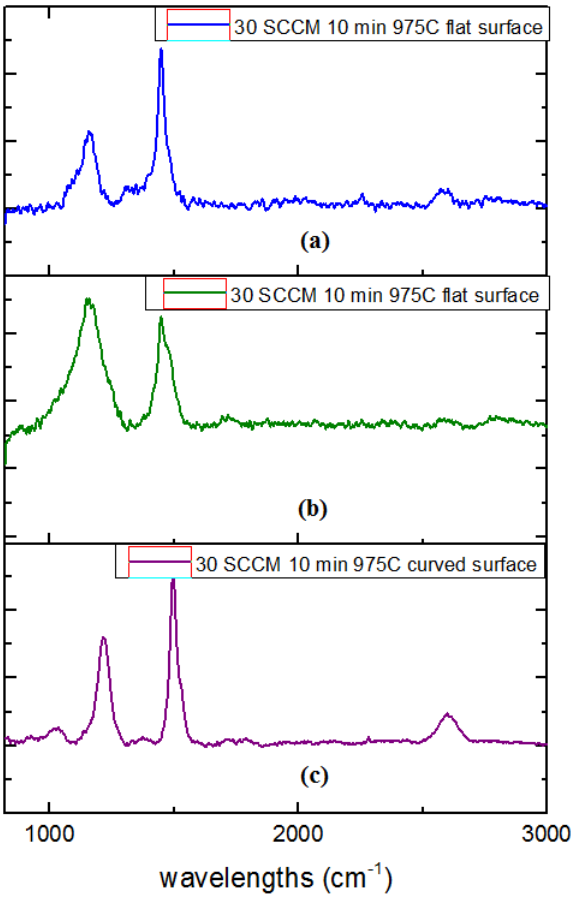

Figure 6.9: Raman spectra at- 30 SCCM methane gas flow at 975^{o}C on flat surface of the cylindrical copper rod (figure a, and b), and curved surface (c). Deposition time for all these experiments were 10 minutes and all of these were successful attempts to grow graphene on cylindrical copper rod surface (785 nm excitation laser).

Graphene thickness measurement by Raman spectroscopy

A low intensity of the disorder induced D band is observed relative to that of the G-band. Peak intensity ratios of I_D to I_G is in the range $0.05 < I_D/I_G < 0.3$ for the graphene monolayer sample grown in the CVD method [43]. It has been reported [44] that the G to G′ peak intensity ratio (I_G/I'_G) provides a good indication of the number of graphene layers in the CVD-derived graphene samples.

Table 6.1: Area, X of maximum Y, Full Width at Half Height (FWHM), and location of G peak (for successful deposition) calculated from Raman spectroscopy

Case	Area	X of maximum Y	FWHM	Location of G peak(cm^{-1})
12 sccm 10 min 975c	776175	174.78	1524.741	
20 sccm 10 min 975c	373436	172.87	167.46	
30 sccm 10 min 1000c curved surface	548744	1315.87	650.6228	
30 sccm 10 min 975c flat surface 1	201388	1585.08	305.87	1584.66
30 sccm 10 min 975c flat surface 2	790044	1318.89	468.6	1586.2
30 sccm 10 min 975c curved surface	752970	1584.582	306.55	1587.89

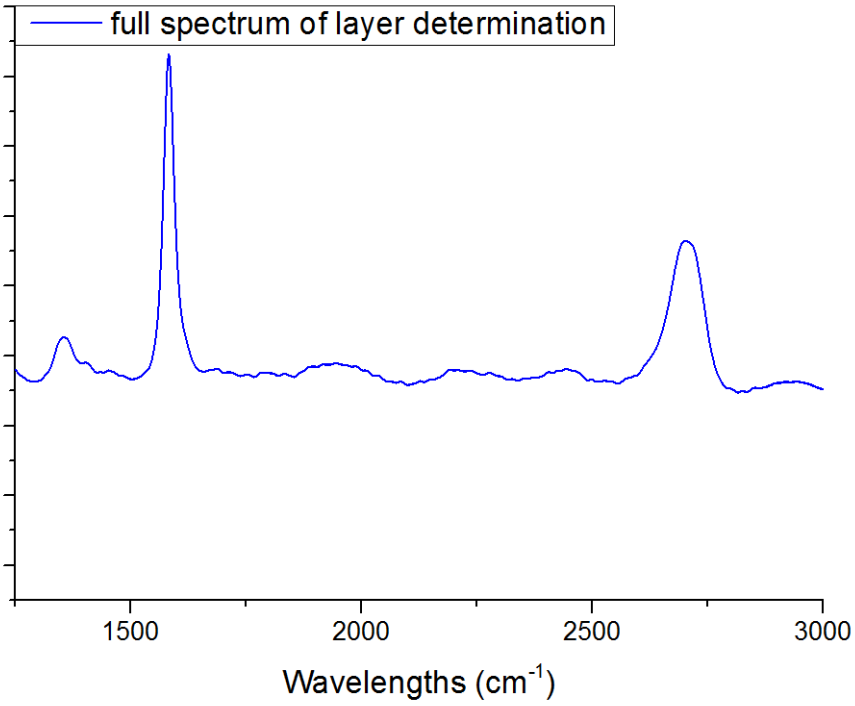

Figure 6.10: Full spectra of the point on copper rod surface where Raman microscopy was used with increased exposure time and accumulations to determine the number of layers by studying the shape of 2D peak.

In order to find out the number of layers of graphene film on copper, Raman spectra was run with increased exposure time of the sample to the laser. An increased accumulation was also taken in order to eliminate the luminescence effect of the sample from the Raman spectra and increase the accuracy. Both shape and G to G′ peak intensity ratio of the Raman spectra shown in figure 6.10 and 6.11 indicate multiple (3) layers of graphene on the samples tested. This result is supported by several literatures [38, 44].

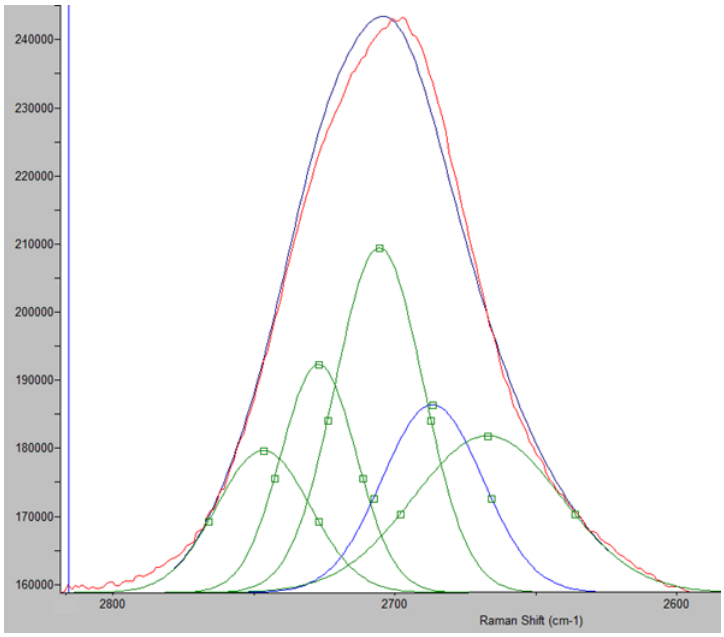

Figure 6.11: Gaussian fit of the 2D peak of Raman spectra (Raman spectra at 10% laser power, 40 sec exposure time and 10 accumulations taken)

Raman mapping analysis

A Raman mapping experiment refers to the collection of a matrix of Raman spectra via automated shifts of the microscope stage of the Raman mapping instrument equipped with point or line laser excitation [45]. Chemical images can then be produced from the acquired spectra in various ways. The simplest option is to follow the intensity variation at the wave numbers that are uniquely assignable to the components of the material being imaged. This so-called univariate approach is used whenever possible because it is the simplest and most understandable way to produce chemical images, one for each component. Raman microspectroscopy is applied to record complete spectral maps of any surface of any object. It provides information on the

position and the concentration of a given element on the surface of the object.

A Raman mapping scan was done with a excitation laser of 532 nm wavelength. Image scanning properties were 150 points per line and 150 lines per image. This scan was run for a surface area of 150 μm by 150 μm. Raman mapping analysis of curved surface by selecting the 1580 peak is presented in the following figure. As the sample had curved surface on its top it was tough to focus on the surface with the instrument. Focused surface (bright yellow in the figure) was showing the presence of quite uniform graphene.

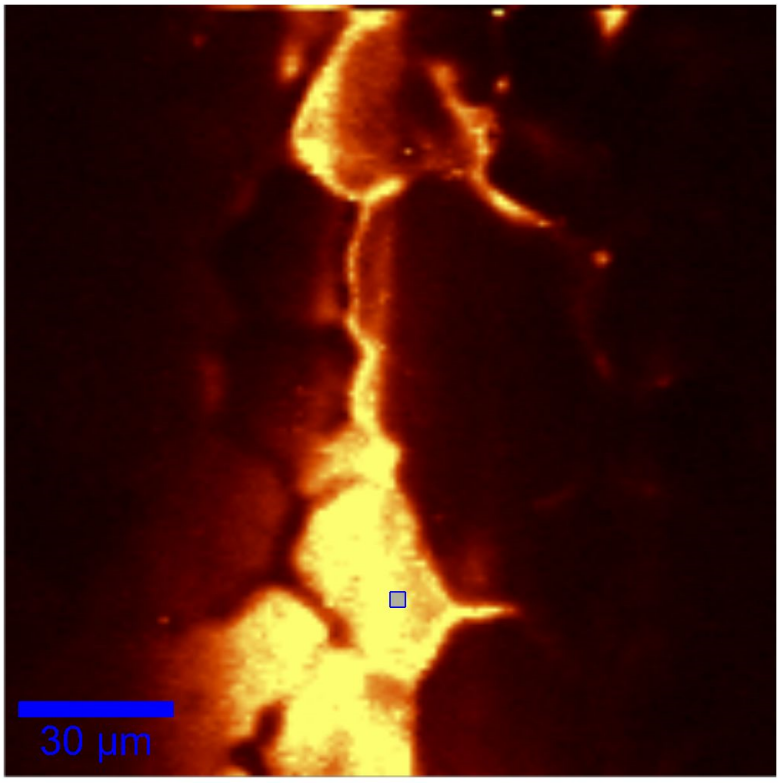

Figure 6.12: Raman mapping analysis of curved surface by selecting the 1580 peak

Scanning electron microscopy of the graphene deposition

In scanning electron microscopy (SEM), an electron beam is scanned across a sample's surface. When the electrons strike the sample, a variety of signals are generated. By detecting specific signals, an image or a sample's elemental composition is produced. The three signals which provide the greatest

amount of information in SEM are the secondary electrons, backscattered electrons and X-rays.

Secondary electrons are emitted from the atoms occupying the top surface producing an image of the surface. A high resolution image can be obtained because of the small diameter of the primary electron beam.

Backscattered electrons are the primary beam electrons which are 'reflected' from atoms in the solid (the sample). The sample morphology causes the variation in contrast across different spots of the image. The image will therefore show the distribution of different chemical phases in the sample. Because these electrons are emitted from a depth in the sample, the resolution in the image is not as good as for the secondary electrons.

Interaction between the primary beams and the atoms in the sample causes shell transitions which result in the emission of an X-ray. The emitted X-ray has an energy characteristic of the parent element. Detection and measurement of the energy permits elemental analysis (Energy Dispersive X-ray Spectroscopy or EDS). EDS can provide a rapid qualitative, or with adequate standards, quantitative analysis of elemental composition with a sampling depth of 1-2 microns [46].

Zeiss sigma SEM was used for taking the SEM images of the surface of the samples. Electron images were taken at different maginification with different scale bar. Li et al [38] defined the thickness variation (number of layers) of the graphene thin film from the color intensity of SEM images. Comparing the results they obtained indicates that, there might be 3 layers of graphene in the prepared samples used in this project.

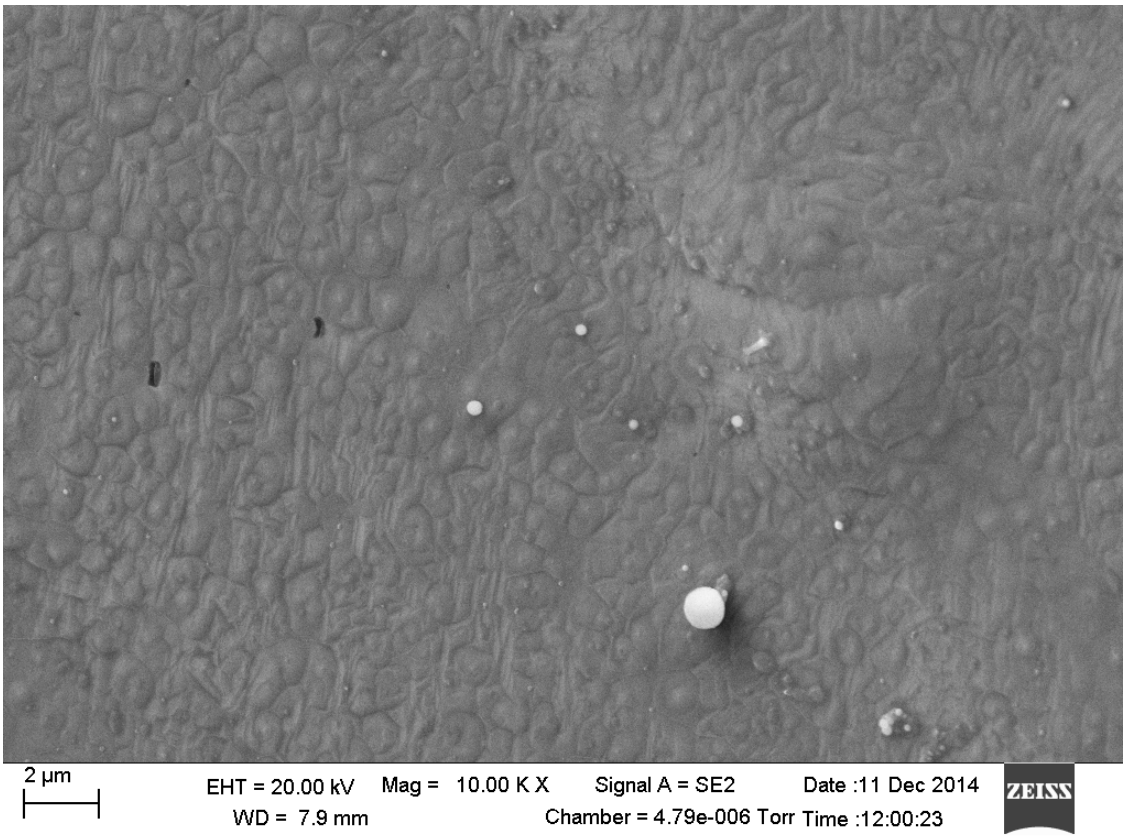

Figure 6.13: SEM image of the sample surface at a 2μm scale bar with 10000 times magification

EDS was also carried out to determine the weight ratio to the constituting compounds. EDS scan resulted in 19.6% of carbon in the sample where the remaining was copper.

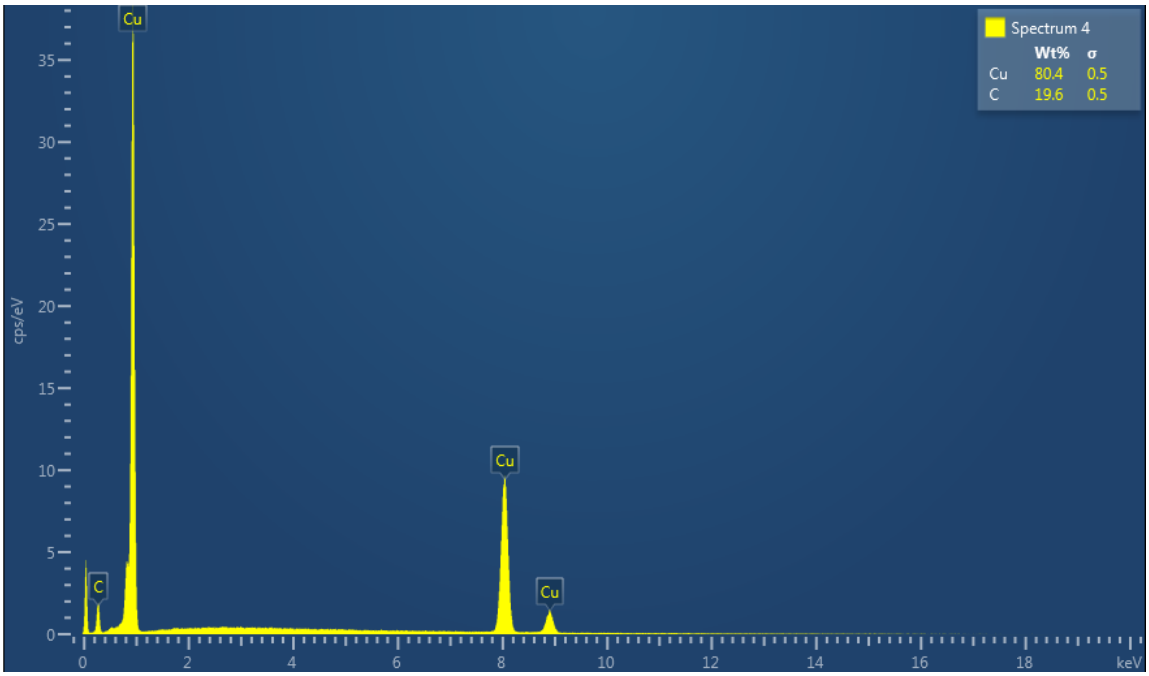

Figure 6.14: EDS scan result

Chapter 7

CONVENTIONAL AND COATED CONDUCTOR TESTING

To evaluate the performance of the graphene coated conductor samples and the uncoated samples they were tested in different test environments. These tests and their results will be discussed in this chapter.

7.1 CDEGS simulation of earth grid system with coated conductor

A two layer soil model was used. The top layer had a resistivity of 50 Ωm and a thickness 5.29 m. The resistivity of the bottom layer was 575.8891 Ωm. For the purpose of study a simple 40 m by 40 m grid was designed. Scalar potential (touch voltage) rise in the earth surface was calculated with CDEGS. First the simulation was run with bare copper as the earth grid conductor. The bare copper was defined with as having a resistivity of 1.68^{-08} Ωm, a relative permittivity of 10^{10}, and a relative permeability of 0.999994. Then coatings of different thicknesses were added to the central conductor (copper). To investigate the influence of the graphene coating, the coating material was defined to have a resistivity of 10^{-8} Ωm, a relative permittivity of 20 and a relative permeability of 1 [47].

This simulation result indicates that graphene coating will not decrease the conductivity of copper. Rather, a thick layer of graphene will increase conductivity to some extent. A similar result was observed in a simulation using stainless steel (resistivity of 6.90^{-07} Ωm, relative permittivity of 10^{10}, rela-

tive permeability of 1) as bulk material. The value of relative permittivity was chosen arbitrarily as the simulation required a large number. Significant improvement of the conductivity of grapheme-coated copper was not observed in comparison to the conductivity of bare copper as the resistivity of copper and graphene is nearly same. But a coating on the stainless steel is likely to bring a mentionable change because stainless steel has a much higher resistivity than the graphene.

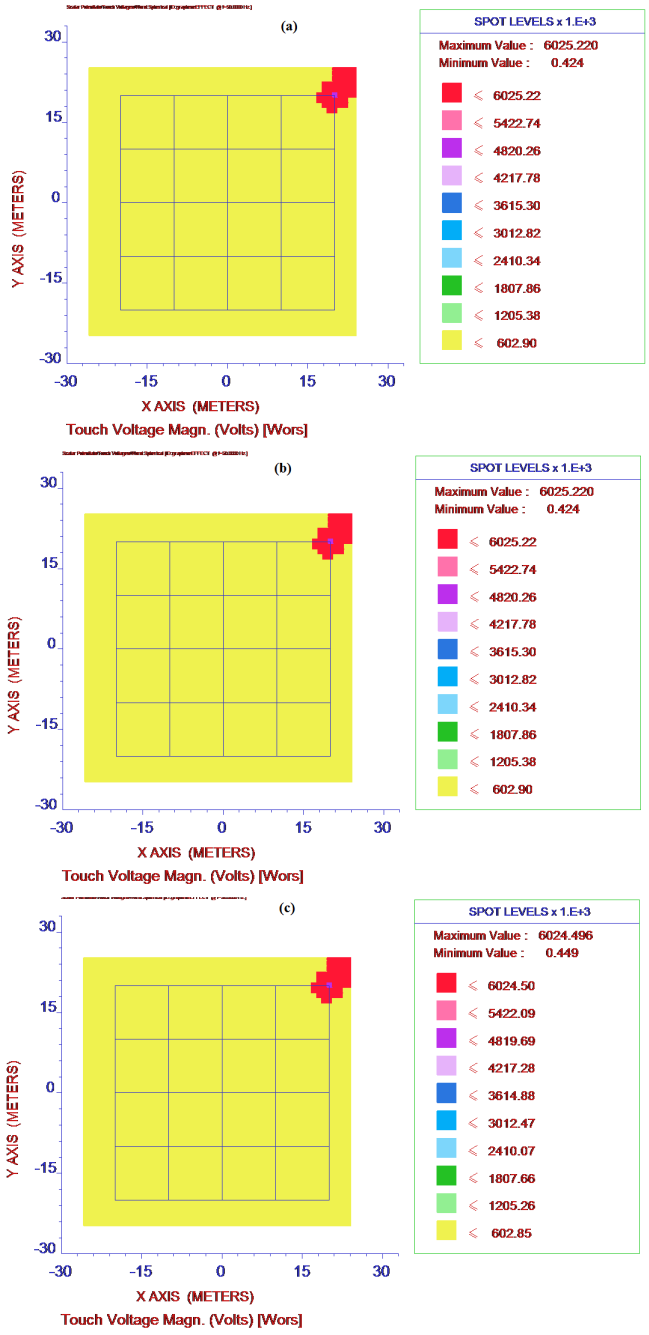

Figure 7.1: Spot 2D view of the scalar potential rise in earth surface (touch voltage) after a staged 275kV fault in 40m by 40m earth grid (CDEGS simulation). Figure a: earth grid material is bare copper. Figure b: earth grid material is graphene coated (10^{-6}m thickness) on bare copper. Figure c: earth grid material is graphene coated (10^{-3}m thickness) on bare copper

7.2 Electrochemical impedance study of the earth grid

The significant factors in the determination of the transient response of any earthing arrangement are:

- earthing resistance: the resistance to earth offered by each element in the earthing system
- inductance: for extensive earth such as grids and counterpoises the transient performance is largely dependent on the self and mutual inductance of individual element
- ohmic resistance of the electrode
- ground capacitance.

Hence, any earthing arrangement can be represented by its distributed earth resistance (or conductance), inductance, ohmic resistance and capacitance per unit length. However, for the usual size of the electrodes used in earth grids, the ohmic resistance is very small and is therefore neglected. Also, the ground capacitance which is in parallel with the earth resistance (leakage conductance) is negligible. The value of C is about one nano Farad per m length taking the dielectric constant of earth as 9. For soil resistivity values up to 3000 Ωm, the time constant RC is of the order of 0.01 to 0.1 microseconds. Ramamoorty et al. [48] indicated that it is sufficient if each element of the grid is modelled with its inductance and ground conductance to evaluate the transient performance.

Van Westling et al. [49] described from the viewpoint of electrochemical impedance spectroscopy that the earth grid could be considered as a electrode of an electrochemical cell. It is represented by a resistance connected in series with a parallel combination of a resistance and a capacitance. For better modelling, capacitance is replaced with a constant phase element (CPE). CPE is used because in soil the electrode (earth grid) remains at a saturated stage with the ion and water concentration.

The soil chemical interface during current flow can be more precisely designed based on the manual from Autolab, Gamry and EC lab:

The potential drop between the reference electrode and the working electrode, is the ohmic resistance and can be represented as R. The ohmic resistance depends on the conductivity of the electrolyte and the geometry of

the electrode. In a Nyquist plot, the intersection of the impedance data with the real part of the axis at the high frequency end gives the ohmic resistance. So in the earthing system soil resistance is the ohmic resistance. In the interface of the conductor/electrode to the soil it is assumed that there forms a resistance known as charge transfer resistance (R_{ct}). An electrical double layer exists at the electrode/electrolyte interface. This double layer is formed as ions from the solution approach the electrode surface. Charges in the electrode are separated from the charges of these ions. The separation is of the order of Angstroms. Modelling an electrochemical phenomenon with an ideal capacitor assumes that the surface under investigation is homogeneous which is normally not the case. This lack of homogeneity is modelled with a CPE.

Nyquist plots and Bode plots are most commonly used to represent studies of electrochemical impedance. In Bode plots the magnitude of the impedance and phase angle are plotted respectively as a function of a wide range of frequency. It is represented in logarithmic scale. Nyquist plots are plotted in linear scale. It is a function of real impedance versus imaginary impedance. The frequency range is selected in such a way that the curve meets the asymptotic limits. In this case imaginary impedance tends to zero. Hence only the real impedance contributes to the total impedance.

In electrochemical systems, diffusion of ionic species at the interface is common. The Warburg impedance was developed to model this phenomenon. In the soil it is assumed that the electricity is diffused so it is expected that the electrochemical cell comprising the earth grid may have Warburg impedance.

7.2.1 Experimental setup

Measurements were made in a conventional electrolytic cell with a platinum counter electrode using a saturated calomel electrode (SCE) as the reference electrode [35]. Anions, such as chloride, sulphite, carbonate etc. are considered to degrade metals/alloys but among these, chloride containing solutions are considered the most aggressive electrolyte in this context [50]. The electrodes were immersed in a solution consisting of 0.5 M (0.5 molecular weight gram powder in per Litre volume of solution- Molar) Sodium Sulphate. A second set of experiments were carried out using 0.1 M sodium chloride as the electrolyte. Exposed surface areas of the conductors to the solution were 520 mm^2. A BioLogic VMP 3 potentiostat was used (EC-Lab 10.17 software) to perform these experiments-

7.2.2 Impedance spectroscopy results

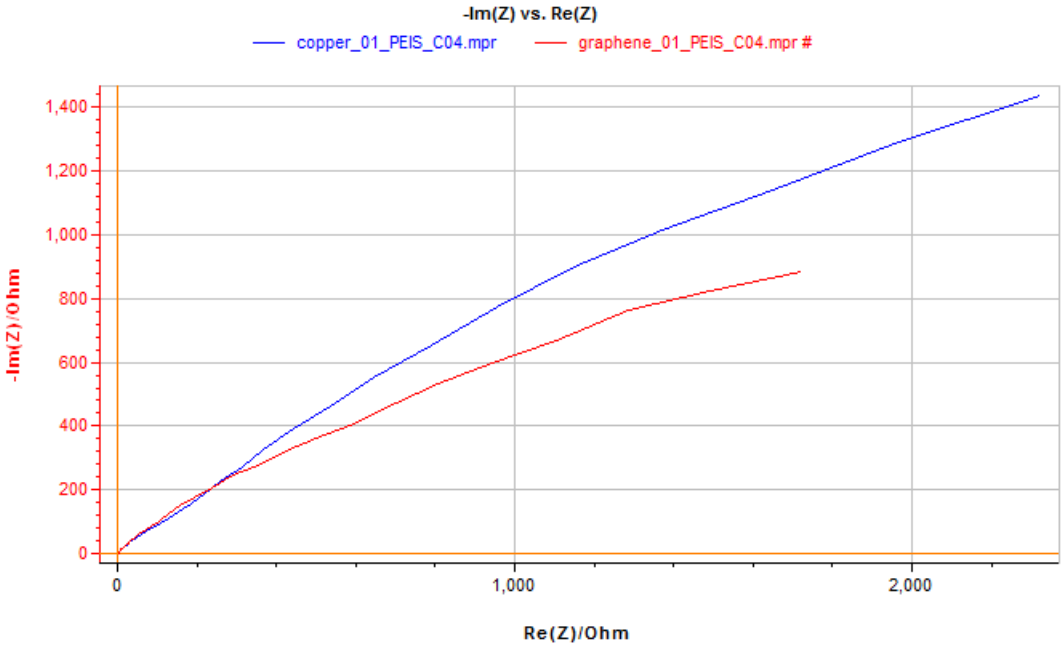

Figure 7.2: Electrochemical impedance spectroscopy of bare and graphene coated copper conductors in 0.5 M Sodium sulphate solution

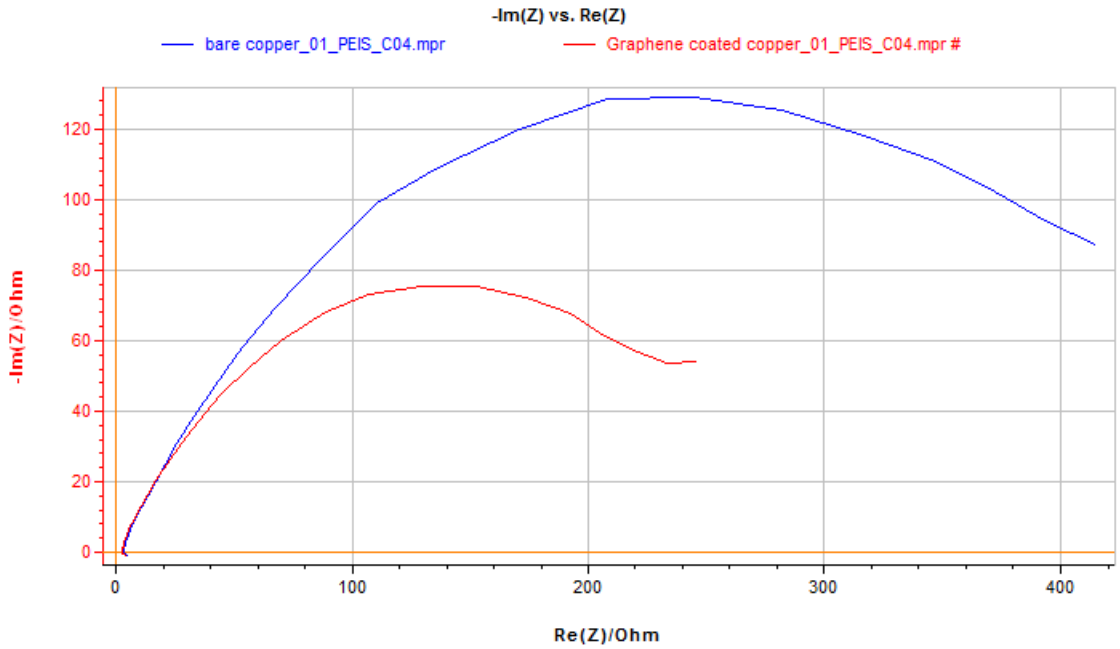

Figure 7.3: Potentio electrochemical impedance spectroscopy of bare and graphene coated copper conductors in 0.1 M Sodium chloride solution

Impedance of two interfaces: metal/electrolyte and surface coating/ electrolyte, is analysed from the Nyquist plot in figure 7.2 and figure 7.3. From these figures it is evident that graphene coated conductors show less resistance (real and imaginary).

7.2.3 Corrosion performance evaluation

If the copper electrodes are corroding at a high rate with the metal ions passing easily into solution, a small potential applied between the electrodes will produce a high current, and therefore a low polarization resistance [51]. This corresponds to a high corrosion rate. This is the basis of the linear polarization measurement used to evaluate corrosion performance of any metal/alloy.

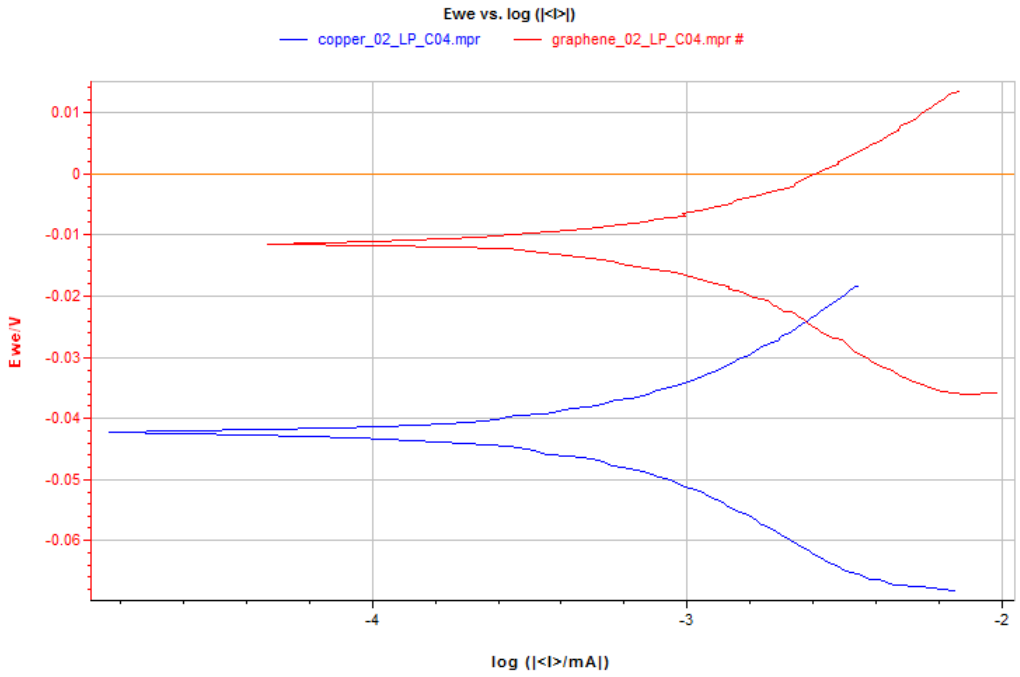

Figure 7.4: Polarization curves of the graphene coated and uncoated copper in 0.5 M sodium sulphate solution

If both anodic and cathodic Tafel lines (Branches of polarization curve) show linear behavior, by extrapolating of lines to corrosion potential and calculating their slope, cathodic and anodic Tafel slopes can be calculated and also corrosion current density is measured from the cross-point of the two lines. In addition, it is possible to calculate the corrosion potential, corrosion current density and anodic and cathodic Tafel slopes if there is at least one branch under activation control. For this purpose, the branch that shows linear behavior is considered [52].

During linear polarization, the anodic dissolution rate of copper at a given potential is estimated by the anodic current densities. The rate of oxygen reduction reaction determines the cathodic current densities [53]. The anodic current densities of the graphene coated specimens were almost the same in magnitude to the uncoated specimens. These results are very close.

E_{corr} quantifies the intensity of corrosion susceptibility. The shift in E_{corr} in the more positive direction indicates less susceptibility to corrosion. The

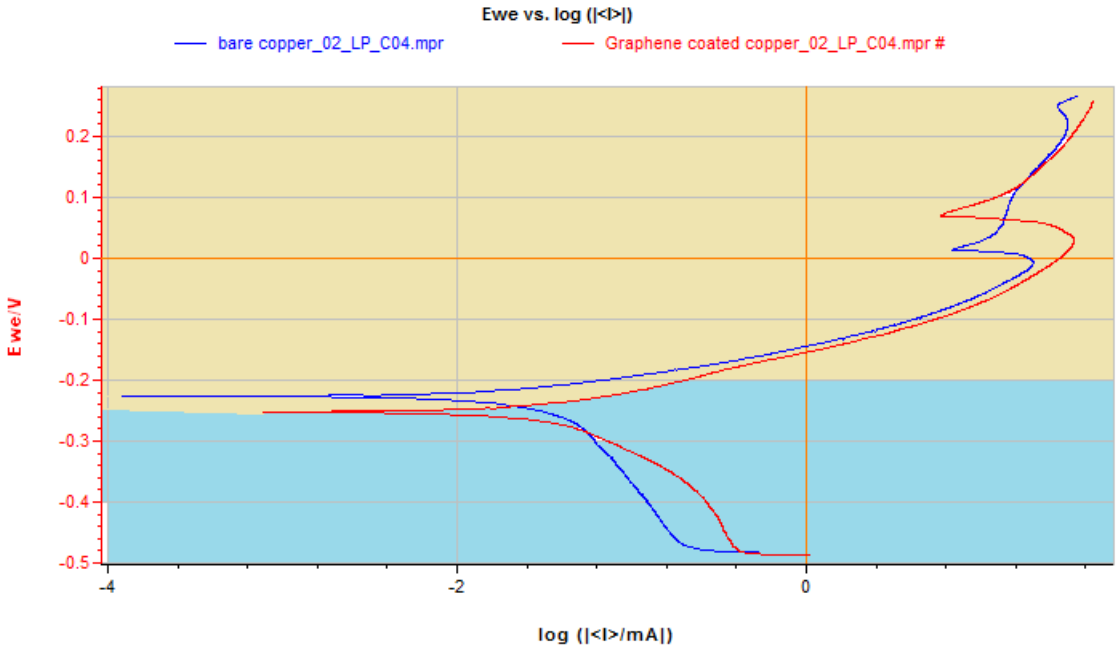

Figure 7.5: Polarization curves of the graphene coated and uncoated copper in 0.1 M sodium chloride solution. (Light yellow indicates the anodic region and light turquoise the cathodic region of the plots.) In this figure the intercept of the anodic and cathodic plots shifts in the positive direction for graphene coated copper. This indicates decreased susceptibility to corrosion of graphene coated copper conductor in comparison to uncoated copper.

corrosion potential, E_{corr} (i.e., the intercept of the anodic and cathodic regions of the plot) of the graphene coated copper specimen was 30 mV more positive as compared to the uncoated copper specimen in both solutions.

From electrochemical point of view, electrons enter the metal and metal ions diffuse into the electrolyte. The DC current that manages to cross the electrode-electrolyte interface experiences a charge transfer resistance. Electricity conduction increases as the charge transfer resistance decreases. From the above analysis we can say that the charge transfer resistance has gotten better for the graphene coated copper samples which is good as this is the path to discharge of the current to earth.

7.3 Scale model test of the earth grid

The scale model test of the conductor grid is done to predict the performance of the earth grid system in the soil environment. The accuracy of the results obtained in the scale model tests is verified by comparing them with the data available in the literature. For the scale model tests all the physical dimensions are scaled down using the same scaling factor. The physical dimensions are conductor diameter, conductor installation depth, soil resistivity etc. It is observed that the pattern of the current flow and the shape of the equipotential surfaces remain unchanged in scale model tests [54]. The following must be ensured in the working setup of soil model test:

- The soil models should be a stable mix with each other. There must be the flexibility to change the soil resistivity of the layers. The liquid models give better test results because they facilitate:
  a) measurements of potentials
  b) replacement and modification of the earthing models representing the grid and vertical rods
  c) proper contact with the thin wires of the model
- The size of the electrolytic tank should be big enough to eliminate the boundary effect.

The early scale model tests used water to represent the uniform soil. The use of the small models in the large tanks gave consistent results. It enabled various models and conditions to be tested and the effects of different parameters to be observed. The technique of using scale models in an electrolytic tank to determine the surface potential distribution during earth faults was introduced in a paper by Koch in 1950 [55]. In the late 1960s, a two-layer laboratory model was developed at Ecole Polytechnique to verify computer techniques [1]. This method used concrete blocks to represent the lower layer of soil (Mukhedkar, Gervais, and Dejean). Ohio State University developed a system using agar (a gelatine like substance, frequently used in biological studies) to simulate the lower levels of soil. In this project, accurate uniform and two-layer soil models were used to study the effects of many parameters on resistance and surface potentials. The results of the model tests have shown that the scale models can be effectively used for parametric studies for earth grid design and for verifying computer simulations of earth grid parameters [56].

In these methods, resistivity of the scale model soil layers could not be controlled precisely. In addition to this, the resistivity of the medium could not

be held to a specific value for a long period. B. Thapar and S.L. Goyal [54] introduced a method to overcome these disadvantages. They suggested using tap water or salt water to represent both the mediums. An anacrylic sheet needs to be fitted with conducting pins to keep the two mediums distinct and separate without hampering the conduction of the electric current.

7.3.1 Test setup

Two conductor rods were immersed into the water. To maintain the same test environment for both set of conductors, all the rods were dipped 2 cm into the water. Therefore, 916.37 mm^2 was the exposed surface area to the water. Water was chosen as the conducting medium for the ease of the experiment as it facilitates current conduction and is very easily sourced. The conductors were connected to the power supply. The test procedure consists of applying voltages across the two electrodes for the purpose of calculating impedance. This procedure is prescribed as part of a standard operating procedure in IEEE documentation [1]. The current was drawn from the nominated outlet; an isolating transformer (8.33A rated) was used for safety and was varied during the test with a VARIAC. The current and voltage were measured by conventional electrical measuring instruments to derive the test cell impedance. The test duration was typically around half an hour for each test.

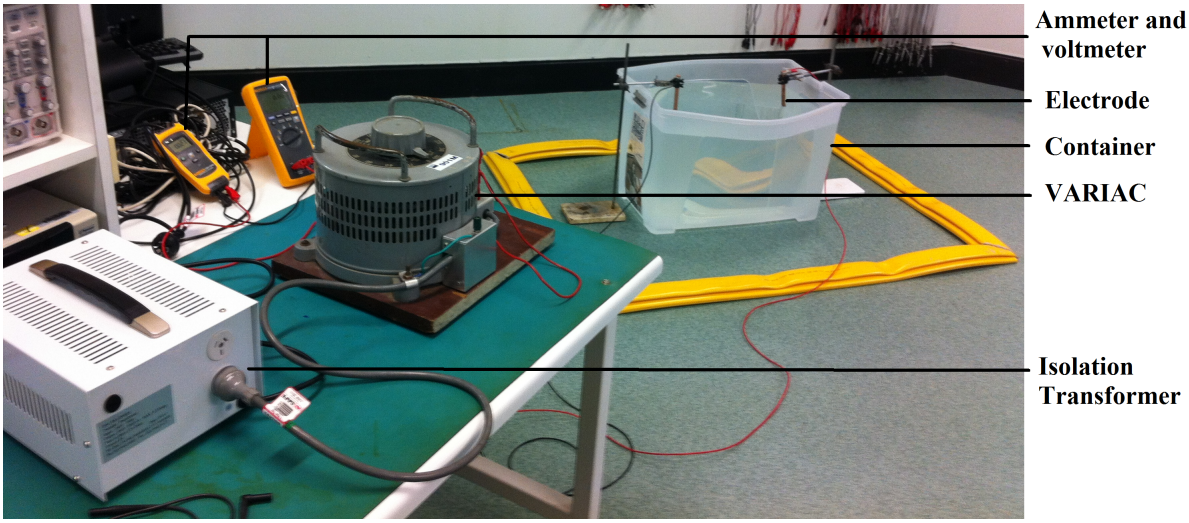

Figure 7.6: Experimental setup for scale model test of earth grid

7.3.2 Test results

Different voltages (up to 274 V) Volts were applied across the conductors for the copper-copper electrode system and the graphene coated copper-graphene coated copper system. The time required to apply the specific voltage and to decrease to zero was also recorded. After applying a certain voltage, current was measured. From the test results it is evident that the graphene coated copper system was conducting more current than the bare copper electrode system for the same applied voltage.

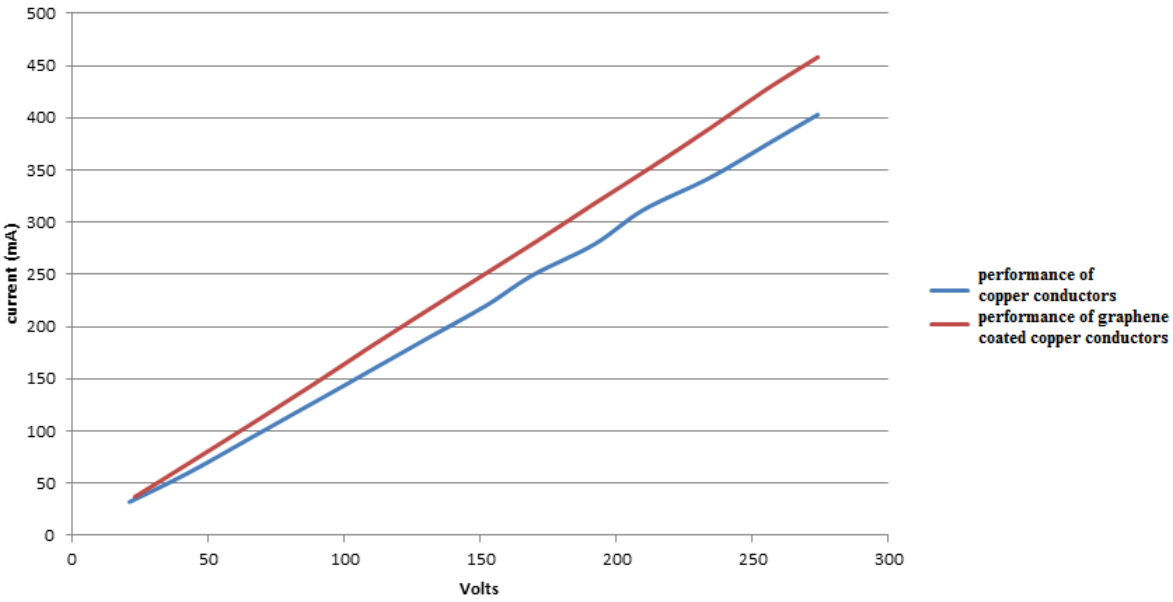

Figure 7.7: Experimental results of the scale model test of earth grid

Some photos of the conductor surface after the test are presented below. It appears that before the experiment the graphene coated conductor is more shiny than the bare copper conductors. But after the current conduction (as well as corrosion to some extent) the graphene coated copper conductors turned darker than the corroded bare copper conductors. Microscopic/spectroscopic tests are required in order to gain better understanding of the surface morphology of these corroded conductors.

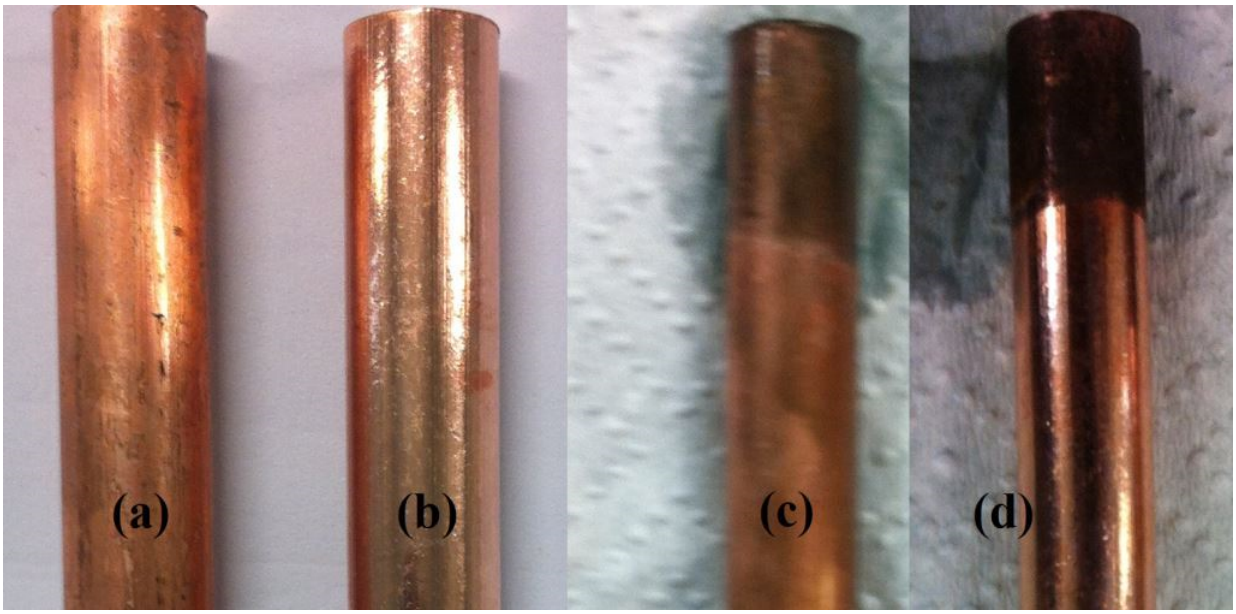

Figure 7.8: uncoated copper conductor before (a) and after (c) I-V test, graphene coated copper conductor before (b) and after (d) I-V test

7.4 Earth grid impulse characteristics

7.4.1 Experimental results based on observations

Behaviour of earth electrodes subjected to the high magnitude impulse currents has been investigated by many researchers. H.W. Towne was the pioneer in this field of research. His research is limited in scope considering the extent and practical importance of the subject. Refs. [57–59] showed that the impulse resistance of a driven earth is below the corresponding power frequency measured value. L. Bewley [57] explained this behaviour as a function of time. Tests were done using parallel insulated counterpoise and buried counterpoise. The counterpoise was buried to a depth of about 12 inches (0.3 m), parallel and directly underneath the line conductors. Tests were made on the lengths of 200 ft (61 m), 500 ft (152.4 m), and 925 ft (281.94 m) earth rods with surges of 15 kV and 90 kV. The impulse resistance of a driven earth was found to be about 20 % lower than its DC resistance. Bewley explained the effect of capacitance and the inductance in the change in impedance during and after lightning strikes.

L. Bewley [57] and P. Bellaschi [58] agreed that inductance of the earth

is usually unimportant. But in the case of abrupt current rise it becomes significant. In their experiment it was observed that the inductance of the rod was approximately 3 μH. In an experiment it was also observed that the ratio of impulse resistance to the power frequency resistance at 1000, 2500, 5000, and 10000 Amperes decreases respectively to the values 0.85, 0.75, 0.65 and 0.55.

In a companion paper, Bellaschi [59] reported a series of impulse tests on electrodes with a current range between 400 A to 15.5 kA. Different impulse shapes (20/50, 8/125 and 25/65) were also varied during these experiments. It was observed that the reduction in the impulse resistance compared to the power frequency resistance depended on the type of soil and the earth electrode arrangement, but was independent of the wave of the impulse. It was also found that the impulse resistance of the electrodes buried in soil of high resistivity had the maximum degree of reduction in resistance from its power frequency resistance. He also observed that the soil surrounding the rod breaks down at a critical voltage gradient. The tests were done in the period spanning December 1940 to September 1941 to observe the seasonal variation of impulse resistance. The seasonal variations in particularly marked at low and medium currents but decreases at the higher currents. It was also observed that rain does not affect the impulse resistance appreciably. Analysis of the data shows that the decrease in resistance of driven earths with the increasing impulse current can be considered to be the result of an increase in the effective radius and length of the rod.

Gupta et al. [60, 61] experimentally investigated the effect of impulse currents on square and rectangular earth grids. The impulse resistance was found to be higher than the power frequency impedance. The impulse resistance was defined as the ratio of the peak voltage to the peak current at the injection point and it was found that this quantity increased as the soil resistivity increased. It was also found that the impulse resistance was higher for the injection at the grid corner rather as compared to the centre. A corner fed grid has a much larger inductance than a centre fed one. As a result, the effective area of a grid fed at the corner is smaller than that of a grid fed at the centre. Laboratory experiments using the scale models of square and rectangular grids in soils of different resistivity also confirmed that the impulse resistance was always higher than the DC resistance for all the resistivities tested. Gupta et al. [60,61] concluded that the soil ionisation effect for the earth grids was very small and can be ignored. But the impulse impedance decreased as the area of the grid increased until a certain area was reached (referred to as the effective area) beyond which no further decrease

was found. Similar findings have been reported by Ramamoorty, et al. [48], and Velazquez and Mukhedkar [62] reported that the transient behaviour of the earth electrode depended on the length of electrode, soil resistivity, permittivity and the shape of the impulse wave. According to their results, the impulse resistance of the earth electrodes increases to a maximum value equal to the surge impedance and then decreases. It eventually reaches the DC resistance of the earth electrode.

Vainer [63] and Giudice et al. [64] have reported some results of experiments to investigate the impulse behaviour of earth grids. In some of the results, the impulse coefficient (ratio of the impulse resistance to the DC resistance) is less than unity which indicates the occurrence of soil ionization. However, a close scrutiny of these results shows that this has happened only in the case of small grids laid in a very high resistivity soils which will normally not happen in actual practice.

To summarise, in the measurement of impulse impedance, soil ionization might be influential if the test is done in a scaled model. In addition, impulse impedance might be higher corresponding to the power frequency impedance. But in real field operations this might not be in effect. Impulse impedance varies according to the injection point of the current. It is independent of shape of the waveform of the current and of seasonal change. So impulse impedance measurement of any earth grid system by varying the impulse injection point may give an idea of the performance of that system.

7.4.2 Insights into the change in impedance during a lightning impulse

The change in impedance of the conductor in the earth is explained from the different perspectives by different authors. L.V. Bewley [57] explained this property with the electrical quantities. He described that at the time the abrupt wave front first arrives at a given point, the current distribution in the earth is governed by the capacitance of the earth. Thus, the zero potential plane with respect to the voltage images is at some depth below the surface. Consequently, $Z = \sqrt{\frac{L}{C}}$ and the effective C is small on account of the depth of the zero potential plane. So the surge impedance is high. These starting values are designated as points a in figure. 7.9. There then ensues a very fast transient at the end of which the resistance network dominates over the capacitance network, after which the zero potential plane rapidly rises to the surface of the earth. The lightning current continues its relatively

slow downward trend, and thus at the end of this readjustment, the effective C is much increased, but with no change in the effective L. Therefore, the surge impedance reduces to a minimum designated by points b in figure 7.9. Thereafter, the effective capacitance does not change. At this point, the zero potential plane is already at the surface, but the current continues its downward displacement. So the effective L increases causing the surge impedance to increase slowly. These effects were reported clearly and definitely for an insulated counterpoise.

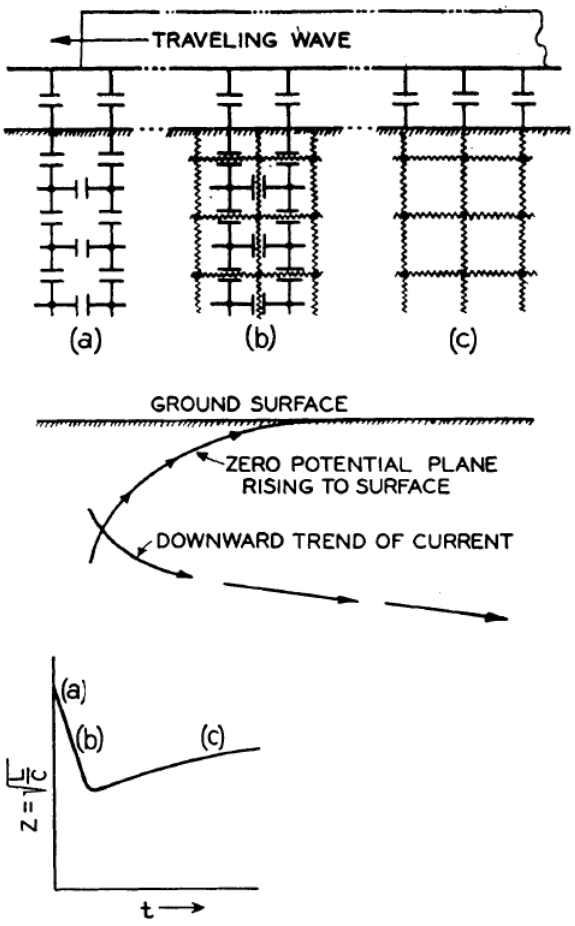

Figure 7.9: Top: Equivalent network at successive instants; Middle: Current and zero potential plane in the earth; Bottom: Variation of surge impedance [57]

P. L. Bellaschi [58] described that the soil near the copper electrode cre-

ates a high resistance surface around the electrode. The soil has different ions and near the copper electrode it tries to form an oxide layer. But the lightning impulse sweeps through the surface of the conductor. So as high resistant soil gets removed and more surface area is created, as a result the resistance gets lowered. He explained with the example of a soil of the resistivity in the order of 0.0075 Ω /m^3 that on the basis of this resistivity, the voltage gradient at the rod would be around 41 kV/cm (assuming an impulse current of 10,000 Amperes (crest)). It is doubtful whether the earth could sustain gradients of this magnitude at all without breakdown.

The critical internal breakdown gradient of the soils is in the range of 10-20 kV/cm. B.R. Gupta et al. [60] mentioned that a stroke impinging on the centre of the earth grid will cause a maximum voltage gradient of only 8 kV/cm. If the stroke impinges at other points of the grid, except the peripheral conductors, the maximum voltage gradient is again not likely to exceed the critical value.

In summary, the impact of lightning strikes in the substation earthing system was emphasized in the previous research works. But the reason behind the change of resistance value due to lightning strikes, electrochemical change of the conductor, changes in soil environment and chemistry in conductor-soil interface was not sufficiently coherent. This section was written to provide a clearer relationship between the above inter-related topics.

7.4.3 Preliminary results from a simulation study of the earth grid response to impulse current

This simulation study is principally to explore the post processing capability of the software packages. In particular, this summary shows the visualisations that are produced for the user to assess the suitability of any proposed earth grid design.

CDEGS simulation studies of lightning strikes at earth grid

To reduce the computation time, a simplified model of earthing system was used to obtain electric field, magnetic field and current densities across various test points. The model consisted of a copper rod of 0.00625 m radius installed at a depth of 0.5 m in an uniform soil with a 100 Ωm resistivity, a relative permittivity of 1 and relative permeability of 1 was assumed.

The lightning surge current considered in this study is defined by the fol-

lowing double exponential type function. Lightning surge was fed to the ground conductor with a copper wire of 0.00625 m radius.

$$I(t) = I_m(e^{-\alpha t} - e^{-\beta t}) \tag{7.1}$$

Where, I_m = 30 kA, α = 1.4 x 10^4 s^{-1} and β = 6 x 10^6 s^{-1}. This wave is characterized by a rise time of 1 μs and a half value time of 50 μs, which are typical values for lightning strokes.

A Fourier transform of lightning stroke current signal resulted in the following frequencies. An electromagnetic field distribution in the soil and through the grounding conductor was calculated for each of these frequencies with CDEGS. These data are presented in Appendix C.

Table 7.1: Frequencies resulted from the Fourier Transform of the lightning strike current signal.

Frequency Number	Frequency
1	0
2	10 kHz
3	20 kHz
4	30 kHz
5	40 kHz
6	50 kHz
7	60 kHz
8	70 kHz
9	90 kHz
10	110 kHz
11	140 kHz
12	250 kHz
13	360 kHz
14	540 kHz
15	720 kHz
16	1.08 MHz
17	1.44 MHz
18	1.8 MHz
19	2.16 MHz
20	2.52 MHz
21	2.56 MHz

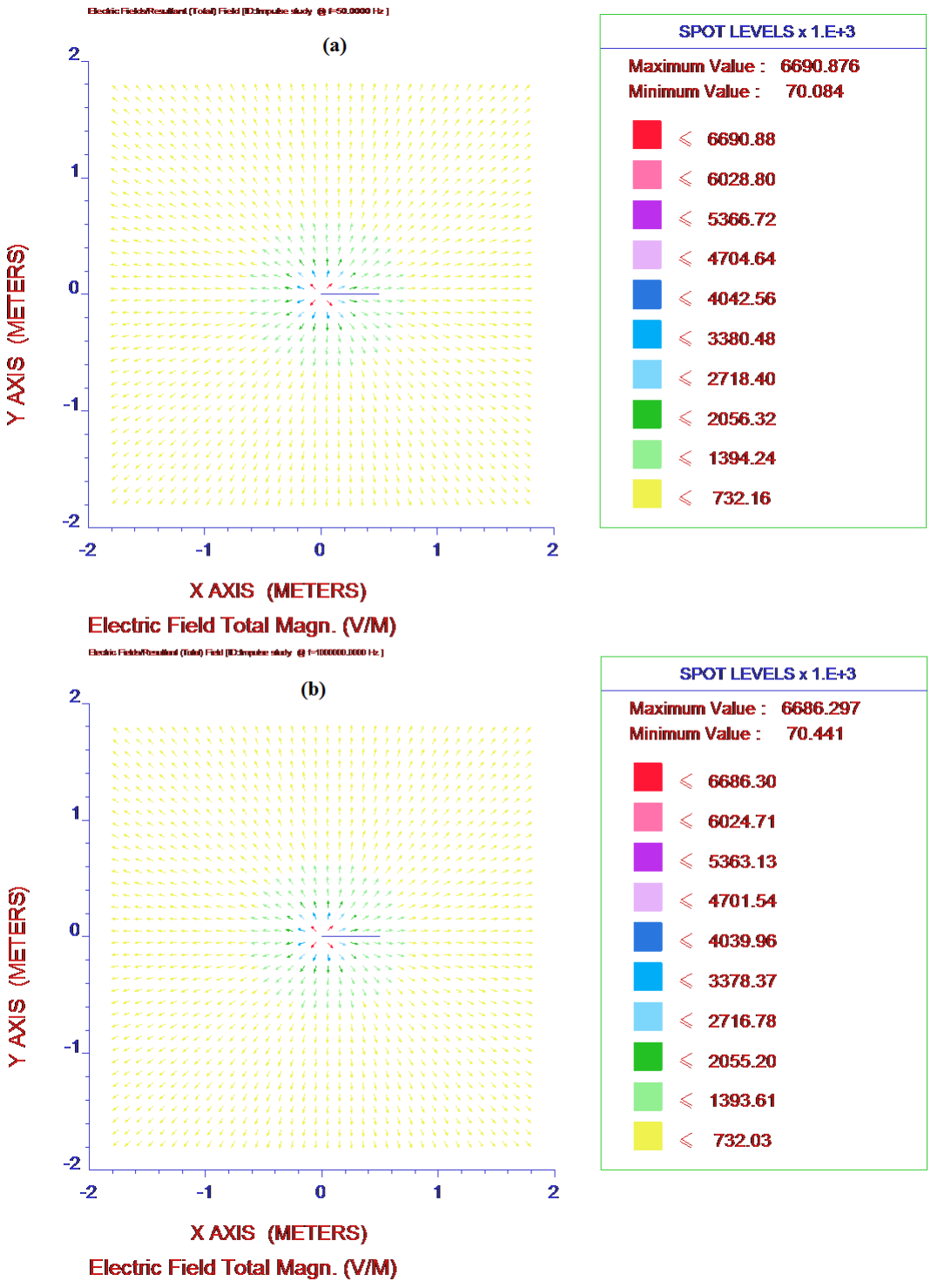

Figure 7.10: Electric field distribution at earth surface at a lightning incident at 50 Hz frequency (a) and at 1 MHz frequency (b).

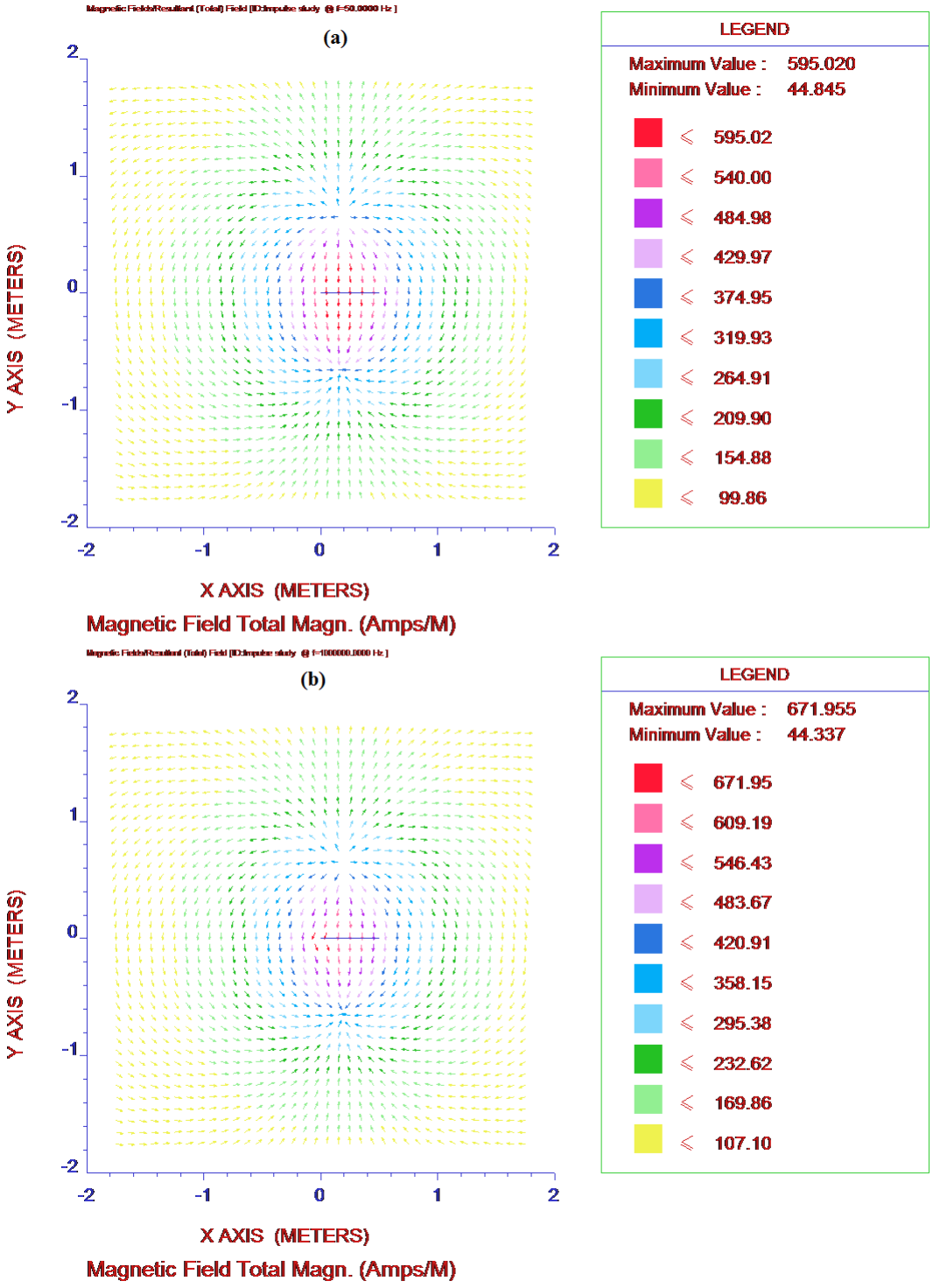

Figure 7.11: Magnetic field distribution at earth surface at a lightning incident at 50 Hz frequency (a) and at 1 MHz frequency (b).

Observations

It was observed in the lightning study of this earthing system that, from the frequency 250 kHz and above, the real part of the current entering to the grounding conductor increased from 0.5197 per unit (P.U.) to 0.5205 P.U.

Ground conductors used in this simulations had a radius of 0.5 m. No current dissipated through the end of the conductor. This infers that current dissipated through its outer surface into the soil (data is presented in the appendix). This study gives an insight that any replacement of copper or surface coating on copper must enable good conduction through its curved surface area.

Chapter 8

CORRODED CONDUCTORS STUDY

In this chapter, a study of corroded metals and earth grid conductors is presented.

Copper has two kinds of oxide compounds: Copper (I) oxide (Cuprite) and Copper (II) oxide (Tenorite). When exposed to the atmosphere, a layer of brown-black copper oxide forms on the surface of the pure copper. This reaction takes place when water, moisture condensation or rain (in which oxygen is dissolved) comes into contact with the copper. It is referred to as copper corrosion or weathering. In contrast to iron corrosion (rust), copper corrosion stops at a point because the layer of copper oxide produced via the corrosion reaction acts as a protective barrier against further corrosion of the underlying copper surface. The end result is a green layer called "verdigris". The basic reaction representing copper corrosion in the atmosphere is:

$$2Cu(s) + O_2(g) = 2CuO(s) \tag{8.1}$$

Table 8.1: Identification of the corrosion type of copper from its color

Name	Formula	Color
Native copper	Cu	Red
Cuprite	Cu_2O	Red
Chalcocite	Cu_2O	Dark gray
Chalcopyrite	Fe_xCu_yS	Gold Metallic
Covellite	CuS	Blue
Bornite	Cu_5FeS_4	Golden brown to copper red
Brochantite	$Cu_4SO_4(OH)_6$	green hydrated copper sulfate
Malachite,	$Cu_2CO_3(OH)_3$	green hydrated copper carbonate
azurite	$Cu_3(CO_3)_2(OH)_2$	blue hydrated copper carbonate

8.1 Corrosion types

8.1.1 AC corrosion

For many years, it was believed that the corrosion of metal structures was caused only by direct current (DC). However, increasingly, it is being recognized that AC corrosion is caused by stray signals generated in the metal structures by nearby conductors [65] carrying AC current. There is an inverse relationship between the impact of the AC current and its frequency. Even on cathodically protected structures AC corrosion might appear [66]. Several publications have suggested that the enhancement of corrosion of the affected structures takes place during the anodic half-cycle of the AC sine wave. Furthermore, it is generally accepted that the AC-enhanced corrosion rate amounts to only a small fraction (in the order of 1% or less) of that caused by DC currents of the same magnitude. AC corrosion in the atmosphere is assumed to proceed slowly as a protective layer builds up on the surface of the conductor [67]. Based on these observations, some articles concluded that the threat of AC-enhanced corrosion, even if potentially present, could be easily mitigated with cathodic protection.

AC current density thresholds for different corrosion rates are as follows [67]:

- Below an AC current density of 30 A/m^2 there is probably no risk of accelerated corrosion;
- Between 30 and 100 A/m^2, corrosion is possible;

- At AC current densities in excess of 100 A/m^2, corrosion damage is to be expected.

Estimation of AC corrosion from fault studies

The formation of natural green patina on the copper structures requires a long time. Several different methods have been developed to achieve the same results artificially using chemical reactions. Copper has good resistance to corrosion by all types of freshwater. Corrosion rates are from 5.08 g/yr to 25.4 g/yr (mass loss). Corrosion rates for water saturated with air and carbon dioxide are an order of magnitude greater than those for municipal or distilled water. Copper also has good resistance to corrosion in seawater and is widely used for sheathing on surfaces exposed to seawater [68].

Goidanich et al. [67] studied AC corrosion as a functions of the exposure time and the alternating current density using the criterion of mass loss. The Power System Earthing Guide Part 1 (EG- 0) [69] gives probabilistic data of the prospective occurence time and the quantity of power system faults in a year based upon the voltage rating. Updated prospective maximum fault current data was collected for different substations in Queensland, Australia. The data and formula given in [67] were utilised to formulate the following study. In the formula:

M_w refers to the molecular weight of the earth grid conductor,
t is the fault duration (in this study fault clearance time is used as fault duration),
I_{rms} is the root mean square of the alternating current amplitude associated with the corrosion process (in this study the probable highest line to earth fault of the specific substation is used),
n is the number of electrons per molar unit associated in the corrosion reaction (for copper it is 2) and
F is the Faraday constant (96500 Coulomb/mol). The study below shows the probable copper loss (in mass) due to earth faults.

- Alexandra headlands (132 kV)

  Δ W=$\frac{M_w.t.I_{rms}.2\sqrt{2}}{\pi nF}$

  Δ W=($2\sqrt{2}$ x 9.88 x 103 x 220 x 10^{-3} X 63.5)/(3.1416 x 2 x 96500)
  = 2.96 x 10^{-4} x 9.88 x 222 = 0.64 g
  Assuming 4 occurrences per year yields metal loss= .64 x 4 = 2.56 g

- Alexandra headlands (11 kV)
  Δ W= 2.96 x 10^{-4} x 9.94 x 1000 = 2.94 g
  Assuming 40 occurrences per year yields metal loss= 2.94 x 40 = 117.69 g

- Blackstone (275 kV)
  Δ W=2.96 x 10^{-4} x 20.12 x 120 = 0.7146 g
  Assuming Single occurrence per year yields metal loss= 0.72 g

- Blackstone (110 kV)
  Δ W=2.96 x 10^{-4} x 22.18 x 220= 1.44 g
  Assuming 4 occurrences per year yeilds metal loss = 5.77 g

- Bulli Creek (330 kV)
  Δ W= 0.5026 g
  Statistics data shows the probability of faults occurring at this voltage level is less than 0.5 occurrences in a year.

- Conabri north (22 kV)
  Δ W=5.75 g
  Assuming 40 occurrences per year yields metal loss of = 230 g

From the above calculation it can be seen that low voltage substations appear to be more affected by AC corrosion. This is due mainly, not to the fault current level in these substations but to the frequent occurrences of faults.

8.2 Survey of cathodic protection in use

Recently (9 April 2014), EPRI (Energy Power and Research Institute) conducted a survey concerned with the recent practice of using cathodic protection to protect against corrosion. In the survey a high percentage of electrical power utilities (41%) reported using cathodic protection as a form of corrosion control on their critical assets. Unless "run to failure" is an option, typical life extension methods include application of coating systems, alternate material selection, inhibitors and cathodic protection systems (impressed current or sacrificial anode). The intent of this survey was to understand the market penetration of cathodic protection, how it was implemented and what structures were selected as either critical or cost effective. From the survey results, it was seen that 11 out of 68 (16.20%) substations are using a mix of impressed current and sacrificial anode cathodic protection (some with deep anode beds).

Earth grids were found to be primarily using impressed current cathodic protection systems (4 out of 68 i.e. 5.90%). Direct buried structures within substations are often candidates for impressed current cathodic protection but some systems designs are sacrificial anode type.

8.3 Summary

Soil influences can be estimated from the pattern of corroded copper conductor samples. Most of the copper conductors in the earth, extracted from the Powerlink substations had green patina on them. As it takes a long time to form that particular kind of patina on the copper conductors in a natural process, the impact of AC corrosion was studied to understand this accelerated corrosion rate. It was found that the earth faults contribute in the corrosion of the earth grids, and it varies with the fault level and the frequency of fault occurrence. Section 8.2 is a summary of the EPRI survey on the use of the cathodic protection to mitigate the impact of corrosion on the earth grid.

Chapter 9

EARTH GRID CONDITION MONITORING

At present some installed earth grids use "impressed current cathodic protection" to maintain a satisfactory earth grid working condition. But this practice does not readily allow the condition of the earth grid to be assessed. In this chapter, "impressed current method" and the "continuous monitoring system outline" will be discussed as a background to a preliminary design for continuous monitoring of the earth grids:

9.1 Cathodic protection using the impressed current method

In this method, the metallic structure was selected as the cathode by connecting the negative terminal of an external direct current power supply to the metallic structure. The positive terminal is connected to an inert anode. Using a corrosion resistant material means that the anodic reaction is not the dissolution of the metal but rather some other reaction such as oxidation of water or chloride ions.

The most commonly used power units are transformer-rectifiers. Power is transformed to the appropriate alternating current voltages then rectified to direct current. There are a commonly used design systems for varying current output including those which allow automatic control, i.e. the unit can sense the potential of the protected structurre and automatically adjust the current up or down so that the potential remains constant. Where main power is not available solar cells, wind generators, thermoelectric generators or gas turbine generators may be used.

The range of materials used for impressed current anodes is much wider than that available for galvanic systems. It ranges from low cost scrap steel which suffers large losses to inert platinised or mixed metal oxide coated titanium which are efficient but expensive. Steel graphite and silicon iron are brittle and must be handled with care at all times. The anode is usually surrounded by backfill such as coke breeze to improve electrical contact between the anode and surrounding soil.

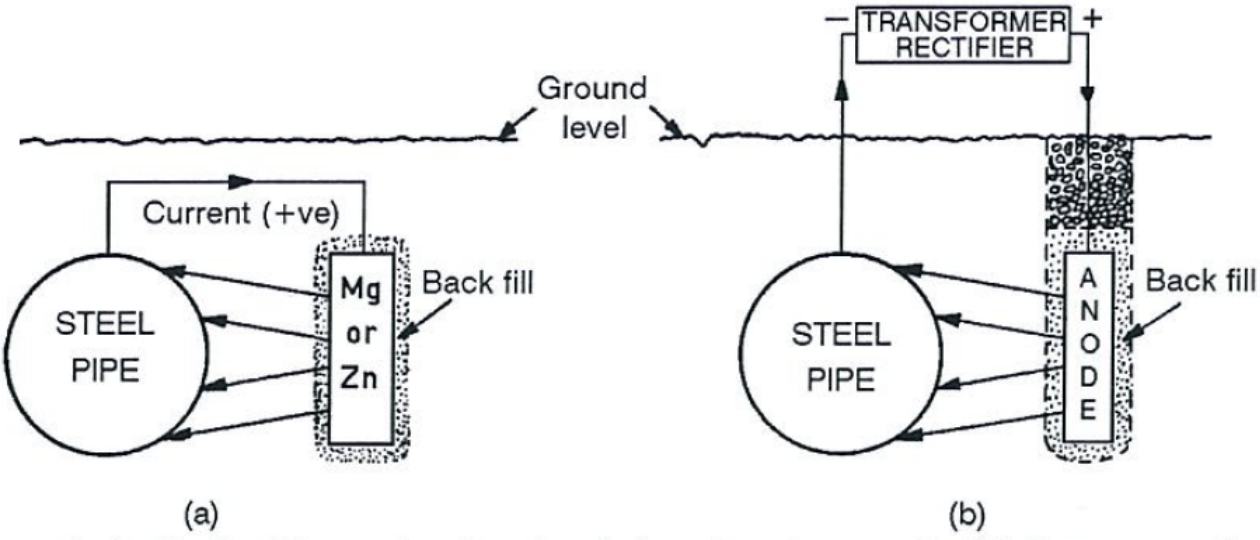

Figure 9.1: Cathodic protection by (a) galvanic anode (b) impressed current [32]

9.2 Outline of a continuous monitoring system

Maximum earth potential rise of an electrical power station/substation during an earth fault is calculated from a staged fault test. This procedure is referred as a current injection test (CIT). The current injection test allows the testing of the actual voltage transfer to nearby infrastructure such as farm fences, water or gas pipelines, and telecommunication assets. The test allows measuring the actual AC induction of any metallic structure running parallel to the feeder. The current injection test can be divided into:

- Earth grid resistance measurements

- Step and touch voltage measurements
- Earth Potential Rise (EPR) contour measurements
- Transfer voltage measurements.

Let the impedance of the power station earth grid be Z_{GE} and the portion of the total fault current which returns through the earth path be I_G. The ground/earth potential rise (GPR) expressed in Volts rms is then obtained by taking the product of I_G and Z_{GE}.

In previous years low current (about 300 mA DC) was used. An AC filter was used on the voltage probe. It was used to average the ambient noise over a given time constant. The filter time constant was usually set to one second. Immediately prior to energizing the DC source on the current probe, the filtered ambient voltage was recorded. The DC source was then switched on and after a delay of three filter time constants (3 seconds) the new potential measurement was recorded. The difference between the measurements was considered the potential rise of the grid due to the DC current [70]. This method for earth resistance measurement was not designed to measure the low Z_{GE} of the large grids, and moreover, it could only measure resistance and not the reactive component of the impedance. When there is a significant amount of stray DC current present in the earth this measurement technique is inaccurate. This difficulty can be overcome by the use of high direct current signal values to achieve a usable signal-to-noise ratio.

F. P. Zupa, and J. F. Laidig [71] described a method for current injection testing which resolves the previous problems. They used the fall-of-potential method with an AC signal with a frequency close to 60 Hz to measure the Z_{GE}. In this method all electrical conducting paths are left connected to the power station grid and with the power station operating in its normal configuration. The GPR is then obtained by multiplying the Z_{GE} and the total single phase fault current available I_{Ftotal}.

Present literature [72] emphasizes the frequency of the injected current. The current injection set frequency should be chosen to ensure minimum overlap between the power frequency and the injection frequency. The authors describe the procedure for two types of scenarios: the substation supplied with a return path (cable screen/overhead earth wire) and the substation supplied without a return path. They concluded that depending on the HV feeding arrangement and its route surrounding the infrastructure, the CIT route shall be determined. It will ensure that the test will yield to acceptable

results.

A recent practice is to use CDEGS to estimate the position of the remote earth. Then using a GPS the estimated probable position is located and the electrodes are installed there. For small isolated power stations, the zone of influence of EPR may be sufficiently small so that portable temporary leads would be appropriate to use as the current and voltage probes. For larger power stations, particularly in built-up areas, the zone of EPR influence may extend for several miles and such leads are impractical. Communications cable pairs are often available, at least temporarily, to extend the probes as far as necessary to reach remote earth. With this literature review as a background, two conceptual models of the continuous monitoring system are described below.

9.2.1 Stand-alone continuous monitoring system

The basic principle behind the proposed continuous monitoring system is that periodically, low level voltage signals of different frequencies are applied between the earth grid and separate electrodes. These separate electrodes will be installed approximately 20 m from the main earth grid. A stand alone control unit is connected between the earth grid and the separate electordes and periodically applies a range of voltage signal types. The response from the grid-electrode configuration to the different applied voltage signals is recorded the control unit. Continuous post processing can then be undertaken on the recorded data. A graphene coated conductor bar will be utilised for this purpose.

It is proposed to use multiple small electrodes to measure:

- Linear polarization resistance (LPR) to measure corrosion rates,
- AC impedance as a function of frequency which measures the change in surface properties,
- The potential of the local environment to estimate corrosion susceptibility (Pourbaix diagram) for measuring corrosion potential.

These data would be used to evaluate the condition of the health of the earth grid. For measuring the earth potential rise a reference remote earth point is necessary.

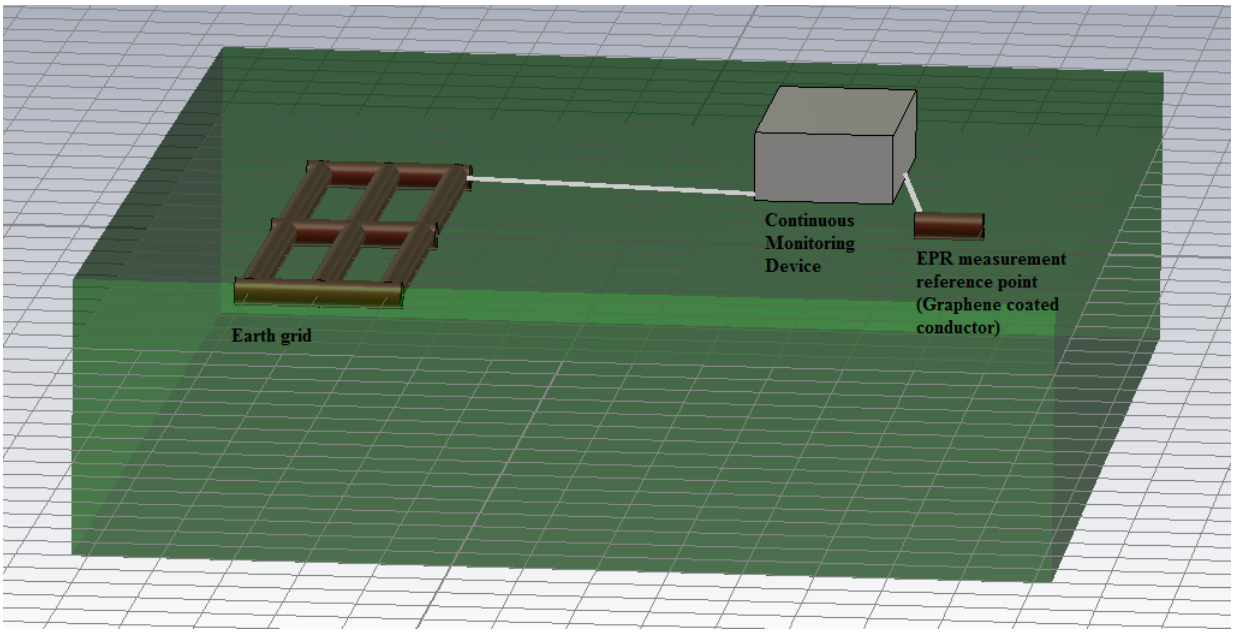

Figure 9.2: Stand-alone continuous monitoring system

9.2.2 Continuous monitoring system utilizing a remote earth electrode of the telecommunication network

In this method, the basics of the impressed current method will be also utilised. One or multiple continuous monitoring devices will be installed near (approximately 20 meters) the main earth grid. This device or devices would inject current at different frequencies and will be able to measure the earth potential rise. These data would be used to evaluate the condition of the earth grid. In contrast to the previous stated method, for measuring the earth potential rise the telecommunication network's remote earth point would be used.

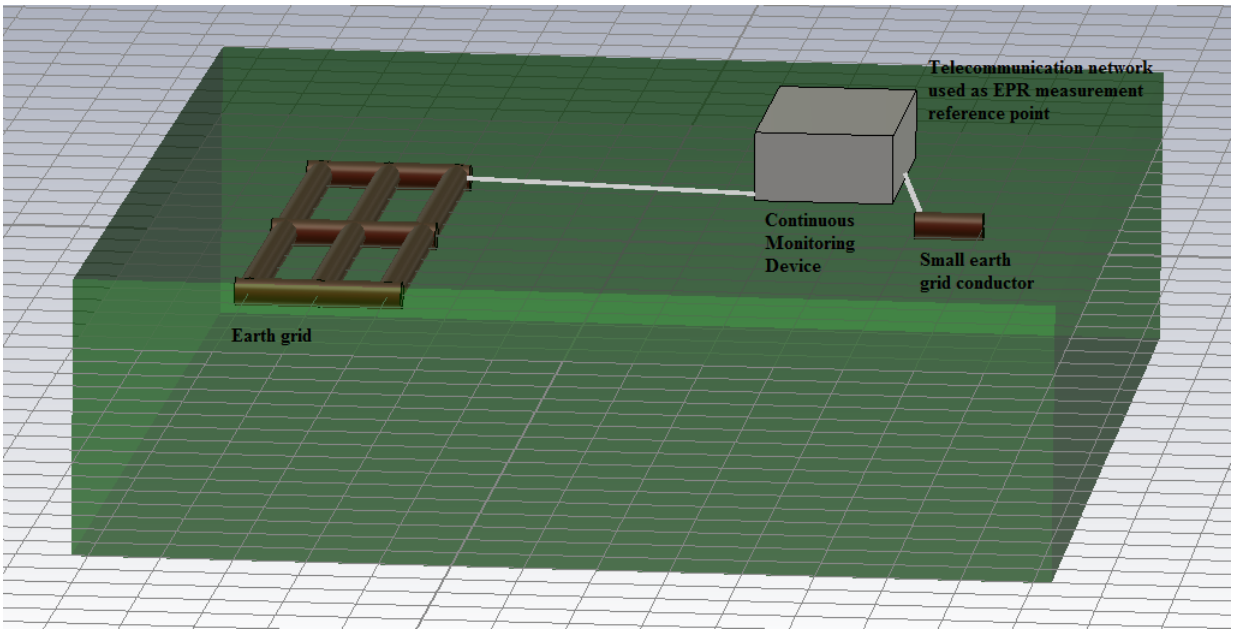

Figure 9.3: Continuous monitoring system utilizing a remote earth electrode of the telecommunication network

Chapter 10

CONCLUSION

10.1 Summary

The project was started to explore the opportunities of enhancing substation earthing system. Improving the design methodology was studied at the early stage of the project. From the earth grid sensitivity analysis with the simulation software, optimum earth grid installation depth in different types of soil and its performance during the lightning strikes was evaluated.

A preliminary study of the opportunities to substitute copper conductors in earthing system was then presented in the thesis. A new way of depositing thin film of graphene on round copper conductors was developed. From a scale model test of earthing system it was found that, graphene coated copper conductors were conducting more current than the bare copper conductors. Corrosion tests resulted in little improved corrosion inhibiting performance. From the experimental data of these experiments it suggests that the charge transfer resistance has reduced for the graphene coated samples. This enables a facilitated path to discharge of the current to earth. The current conduction mechanism of graphene coated copper is yet to be fully explored.

The linear polarization method is used for continuously monitoring the metal pipeline corrosion. A continuous monitoring system for earth grid is proposed utilizing this method. It has been also proposed to evaluate the applicability of impressed current method utilizing telecommunication network's remote earth point for earth potential rise measurement to make the monitoring system robust.

10.2 Future work

Majumder et al. [34] has reported that graphene acts as an ionic barrier to steel, which inhibits corrosion. To what extent charge transfer resistance improves for graphene coated steel would infer the possibility of earthing performance with this coated metal. While graphene occupies only a few monolayers of carbon it has a noticeable effect on the surface potential of the metal. Improvements in conductivity of the graphene coated steel would bring a paradigm shift in the power industry as this would be very cost effective in comparison to the copper. So, to extend this work, it would be very useful to investigate the performance of graphene coated steel as an earth grid conductor.

Extracted data from the on-site data logger (established as a part of a continuous monitoring system development) would not only facilitate the device fabrication but will provide new insights into grid behaviour over a period of time.

Bibliography

[1] "IEEE guide for safety in ac substation grounding," *IEEE Std 80-2000*, pp. i–192, 2000.

[2] G. A. Burdick, "Energy band structure of copper," *Physical Review*, vol. 129, no. 1, p. 138, 1963.

[3] V. Singh, D. Joung, L. Zhai, S. Das, S. I. Khondaker, and S. Seal, "Graphene based materials: past, present and future," *Progress in Materials Science*, vol. 56, no. 8, pp. 1178–1271, 2011.

[4] K. S. Novoselov, A. K. Geim, S. Morozov, D. Jiang, Y. Zhang, S. Dubonos, I. Grigorieva, and A. Firsov, "Electric field effect in atomically thin carbon films," *science*, vol. 306, no. 5696, pp. 666–669, 2004.

[5] K. Novoselov, D. Jiang, F. Schedin, T. Booth, V. Khotkevich, S. Morozov, and A. Geim, "Two-dimensional atomic crystals," *Proceedings of the National Academy of Sciences of the United States of America*, vol. 102, no. 30, pp. 10 451–10 453, 2005.

[6] J. S. Bunch, A. M. Van Der Zande, S. S. Verbridge, I. W. Frank, D. M. Tanenbaum, J. M. Parpia, H. G. Craighead, and P. L. McEuen, "Electromechanical resonators from graphene sheets," *Science*, vol. 315, no. 5811, pp. 490–493, 2007.

[7] A. K. Geim and K. S. Novoselov, "The rise of graphene," *Nature materials*, vol. 6, no. 3, pp. 183–191, 2007.

[8] J. Wintterlin and M.-L. Bocquet, "Graphene on metal surfaces," *Surface Science*, vol. 603, no. 10, pp. 1841–1852, 2009.

[9] *Substation earthing guide*. Energy Networks Association, 2006, vol. EG1.

[10] J. Sverak, "Simplified analysis of electrical gradients above a ground grid-i how good is the present ieee method? (a special report for wg 78.1)," *Power Apparatus and Systems, IEEE Transactions on*, vol. PAS-103, no. 1, pp. 7–25, Jan 1984.

[11] S. J. Schwarz, "Analytical expressions for the resistance of grounding systems [includes discussion]," *Transactions of the American Institute of Electrical Engineers Power Apparatus and systems, part iii.*, vol. 73, no. 2, pp. –, Jan 1954.

[12] G. F. Tagg, *Earth resistances*. G. Newnes, 1964.

[13] A. Samouëlian, I. Cousin, A. Tabbagh, A. Bruand, and G. Richard, "Electrical resistivity survey in soil science: a review," *Soil and Tillage Research*, vol. 83, no. 2, pp. 173–193, 2005.

[14] E. B. Joffe and K.-S. Lock, "Grounding for power distribution and lightning protection systems," *Grounds for Grounding: A Circuit-to-System Handbook*, pp. 371–468.

[15] Y. Gao, R. Zeng, X. Liang, J. He, W. Sun, and Q. Su, "Safety analysis of grounding grid for substations with different structure," in *Proceedings of International Conference on Power System Technology*, vol. 3, 2000, pp. 1487–1492 vol.3.

[16] W. I. T. 64, "Disconnecting times and related matters: Fault voltage definitions," January 1988.

[17] A. Puttarach, N. Chakpitak, T. Kasirawat, and C. Pongsriwat, "Substation grounding grid analysis with the variation of soil layer depth method," in *Power Tech, 2007 IEEE Lausanne*. IEEE, 2007, pp. 1881–1886.

[18] J. Sverak, "Optimized grounding grid design using variable spacing technique," *Power Apparatus and Systems, IEEE Transactions on*, vol. 95, no. 1, pp. 362–374, Jan 1976.

[19] AECOM, "Earthing system (design report-kumbarilla park 275/132kv substation)," 22 March 2012.

[20] T. Mitton and R. Watson, "Specialist earthing analysis," *Transmission & Distribution*, vol. 5, p. 55, 2010.

[21] L. H. Harrison, "The effect of reactive components in the measurement of grounding circuits," *American Institute of Electrical Engineers, Part II: Applications and Industry, Transactions of the*, vol. 72, no. 5, pp. 340–345, 1953.

[22] "IEEE guide for measuring earth resistivity, ground impedance, and earth surface potentials of a grounding system," *IEEE P81/D11*, pp. 1–86, 2012.

[23] R. Rdenberg, "Grounding principles and practice i—fundamental considerations on ground currents," *Electrical Engineering*, vol. 64, no. 1, pp. 1–13, 1945.

[24] F. Dawalibi and D. Mukhedkar, "Transferred earth potentials in power systems," *Power Apparatus and Systems, IEEE Transactions on*, vol. PAS-97, no. 1, pp. 90–101, 1978.

[25] C. H. Lee and C. N. Chang, "Comparison of the safety criteria used for ground grid design at 161/23.9 kV indoor-type substation," *International Journal of Electrical Power Energy Systems*, vol. 49, pp. 47-56, 2013.

[26] C.-H. Lee, "Safety Assessment of AC Grounding Systems Based on Voltage Dependent Body Resistance."

[27] A. Dimopoulos, H. Griffiths, A. Haddad, A. Ainsley, F. Ainslie, and D. Frame, "Parametric Analysis of Safety Limit-Curves in Earthing Systems and Comparison of International Standard Recommendations," in Universities Power Engineering Conference, 2006. UPEC'06. Proceedings of the 41st International, 2006, pp. 272-276.

[28] H. Dehbonei, "Risk Based versus Deterministic Earthing Design Methods," 2010.

[29] D. IEC, "Ts 60479-1: 2005," *Effects of Current on Human Beings and Livestock–Part 1: General Aspects*, 2006.

[30] E. P. Ltd, "Comparison of substation safety criteria given by the american (ieee) and european (iec) standards," http://www.elek.com.au/Files/SafeGrid/Earthing%20Grid%20Safety%20Criteria_IEEE%20and%20IEC%20Comparison.pdf, last accessed 3rd December, 2014.

[31] "Safe substation grounding - part ii," *IEEE Transactions on Power Apparatus and Systems*, vol. PAS-101, no. 10, pp. 4006–4023, Oct 1982.

[32] "Introduction to cathodic protection." Australian corrosion association, 1990.

[33] J. S. Bunch, S. S. Verbridge, J. S. Alden, A. M. van der Zande, J. M. Parpia, H. G. Craighead, and P. L. McEuen, "Impermeable atomic membranes from graphene sheets," *Nano letters*, vol. 8, no. 8, pp. 2458–2462, 2008.

[34] R. Singh Raman, P. Chakraborty Banerjee, D. E. Lobo, H. Gullapalli, M. Sumandasa, A. Kumar, L. Choudhary, R. Tkacz, P. M. Ajayan, and M. Majumder, "Protecting copper from electrochemical degradation by graphene coating," *Carbon*, vol. 50, no. 11, pp. 4040–4045, 2012.

[35] N. Kirkland, T. Schiller, N. Medhekar, and N. Birbilis, "Exploring graphene as a corrosion protection barrier," *Corrosion Science*, vol. 56, pp. 1–4, 2012.

[36] L. Cardenas, J. MacLeod, J. Lipton-Duffin, D. Seifu, F. Popescu, M. Siaj, D. Mantovani, and F. Rosei, "Reduced graphene oxide growth on 316l stainless steel for medical applications," *Nanoscale*, 2014.

[37] O. Leenaerts, B. Partoens, and F. Peeters, "Water on graphene: Hydrophobicity and dipole moment using density functional theory," *Physical Review B*, vol. 79, no. 23, p. 235440, 2009.

[38] X. Li, W. Cai, J. An, S. Kim, J. Nah, D. Yang, R. Piner, A. Velamakanni, I. Jung, E. Tutuc *et al.*, "Large-area synthesis of high-quality and uniform graphene films on copper foils," *Science*, vol. 324, no. 5932, pp. 1312–1314, 2009.

[39] Y. Yao, Z. Li, Z. Lin, K.-S. Moon, J. Agar, and C. Wong, "Controlled growth of multilayer, few-layer, and single-layer graphene on metal substrates," *The Journal of Physical Chemistry C*, vol. 115, no. 13, pp. 5232–5238, 2011.

[40] "Raman spectroscopy," http://en.wikipedia.org/wiki/Raman_spectroscopy, [Online; last accessed: 6 Jan 2015].

[41] U. of Exeter, "Surface enhanced raman spectroscopy," https://newton.ex.ac.uk/research/biomedical-old/optics/sers.html, last accessed 3rd January, 2015.

[42] A. Ferrari, J. Meyer, V. Scardaci, C. Casiraghi, M. Lazzeri, F. Mauri, S. Piscanec, D. Jiang, K. Novoselov, S. Roth *et al.*, "Raman spectrum of graphene and graphene layers," *Physical review letters*, vol. 97, no. 18, p. 187401, 2006.

[43] L. Malard, M. Pimenta, G. Dresselhaus, and M. Dresselhaus, "Raman spectroscopy in graphene," *Physics Reports*, vol. 473, no. 5, pp. 51–87, 2009.

[44] A. Reina, X. Jia, J. Ho, D. Nezich, H. Son, V. Bulovic, M. S. Dresselhaus, and J. Kong, "Large area, few-layer graphene films on arbitrary substrates by chemical vapor deposition," *Nano letters*, vol. 9, no. 1, pp. 30–35, 2008.

[45] S. Sasić *et al.*, "Raman mapping of low-content api pharmaceutical formulations. i. mapping of alprazolam in alprazolam/xanax tablets." *Pharmaceutical research*, vol. 24, no. 1, p. 58, 2007.

[46] "Sem,eds : Scanning electron microscopy with x-ray microanalysis," http://wings.buffalo.edu/faculty/research/scic/sem-eds.html, [Online; last accessed: 20 Nov 2014].

[47] "Graphene," http://en.wikipedia.org/wiki/Graphene, [Online; last accessed: 4 Mar 2014].

[48] M. Ramamoorty, M. Narayanan, S. Parameswaran, and D. Mukhedkar, "Transient performance of grounding grids," *Power Delivery, IEEE Transactions on*, vol. 4, no. 4, pp. 2053–2059, Oct 1989.

[49] E. Van Westing, G. Ferrari, F. Geenen, and J. De Wit, "In situ determination of the loss of adhesion of barrier epoxy coatings using electrochemical impedance spectroscopy," *Progress in organic coatings*, vol. 23, no. 1, pp. 89–103, 1993.

[50] R. Singh Raman, P. Chakraborty Banerjee, D. E. Lobo, H. Gullapalli, M. Sumandasa, A. Kumar, L. Choudhary, R. Tkacz, P. M. Ajayan, and M. Majumder, "Protecting copper from electrochemical degradation by graphene coating," *Carbon*, vol. 50, no. 11, pp. 4040–4045, 2012.

[51] Caproco, "Caprocolinear polarization resistance lpr) general information," http://www.caproco.com/catalog/pdf/Probes-Instruments/Linear-Polarization-Resistance/LPR-General-Information.pdf, last accessed 3rd December, 2014.

[52] A. Kosari, M. Momeni, R. Parvizi, M. Zakeri, M. Moayed, A. Davoodi, and H. Eshghi, "Theoretical and electrochemical assessment of inhibitive behavior of some thiophenol derivatives on mild steel in hcl," *Corrosion Science*, vol. 53, no. 10, pp. 3058–3067, 2011.

[53] G. Kear, B. Barker, and F. Walsh, "Electrochemical corrosion of unalloyed copper in chloride media—-a critical review," *Corrosion science*, vol. 46, no. 1, pp. 109–135, 2004.

[54] B. Thapar and S. Goyal, "Scale model studies of grounding grids in non-uniform soils," *Power Delivery, IEEE Transactions on*, vol. 2, no. 4, pp. 1060–1066, 1987.

[55] W. Koch, "Grounding methods for high-voltage stations with grounded neutrals," *translated from Elektrotechnische Zeitschrift*, vol. 71, no. 4, pp. 89–91, 1950.

[56] J. Sverak, C. Booraem, and D. Kasten, "Post-design analysis and scale model tests for a two grid earthing system serving the 345kv gis facilities at seabrook power plant," in *CIGRE Symposium on High Currents in Power Systems Under Normal, Emergency and Fault Conditions. Brussels, Belgium:[sn]*, 1985.

[57] L. Bewley, "Theory and tests of the counterpoise," *Electrical Engineering*, vol. 53, no. 8, pp. 1163–1172, 1934.

[58] P. Bellaschi, "Impulse and 60-cycle characteristics of driven grounds," *Transactions of the American Institute of Electrical Engineers*, vol. 60, no. 3, pp. 123–128, 1941.

[59] P. L. Bellaschi, R. E. Armington, and A. E. Snowden, "Impulse and 60-cycle characteristics of driven grounds - ii," *Electrical Engineering*, vol. 61, no. 6, pp. 349–363, June 1942.

[60] B. Gupta and B. Thapar, "Impulse impedance of grounding grids," *IEEE Transactions on Power Apparatus and Systems*, vol. PAS-99, no. 6, pp. 2357–2362, Nov 1980.

[61] B. Gupta and V. K. Singh, "Impulse impedance of rectangular grounding grids," *IEEE transactions on Power Delivery*, vol. 7, no. 1, pp. 214–218, Jan 1992.

[62] R. Velazquez and D. Mukhedkar, "Analytical modelling of grounding electrodes transient behavior," *IEEE transactions on Power Apparatus and Systems*, vol. PAS-103, no. 6, pp. 1314–1322, June 1984.

[63] A. Vainer, "Impulse characteristics of grounding systems," *ELEKTRICHESTVO (USSR)*, pp. 23–27, March 1966.

[64] E. Giudice and G. L. Piparo, "Behaviour of earth plates to pulse waveforms," *Telecomunicazioni(Italia)*, vol. 21, pp. 59–65, 1972.

[65] R. Zhang, P. R. Vairavanathan, and S. B. Lalvani, "Perturbation method analysis of ac-induced corrosion," *Corrosion Science*, vol. 50, no. 6, pp. 1664–1671, 2008.

[66] N. G. T. Mark Yunovich, "Ac corrosion: Corrosion rate and mitigation requirements," N. International, Ed., no. NACE-04206, CC Technologies. New Orleans, Louisiana: CORROSION 2004, 28 March-1 April 2004.

[67] S. Goidanich, L. Lazzari, and M. Ormellese, "Ac corrosion. part 2: Parameters influencing corrosion rate," *Corrosion science*, vol. 52, no. 3, pp. 916–922, 2010.

[68] Corrosionist, "Why does copper oxidize," http://www.corrosionist.com/Why_Does_Copper_Oxidize.htm, last accessed 16th July, 2014.

[69] E. N. A. Limited, *Power System Earthing Guide Part 1: Management Principles*, 1st ed., E. N. A. Limited, Ed. Energy Networks Association Limited, May 2010.

[70] I. S. B. Project, "A guide for determining the maximum electric power station ground potential rise and induced voltage from a power fault," *I.C.E.P. Guide*, vol. P367, p. 2, December 6, 1977.

[71] F. P. Zupa and J. F. Laidig, "A practical ground potential rise prediction technique for power stations," *IEEE Transactions on Power Apparatus and Systems*, vol. PAS-99, no. 1, pp. 207–216, Jan 1980.

[72] M. Nassereddine, J. Rizk, A. Hellany, and M. Nagrial, "Hv substation earth grid commissioning using current injection test (cit) method," in *8th IEEE Conference on Industrial Electronics and Applications (ICIEA), 2013*, June 2013, pp. 67–72.

Appendix A

DATA USED FOR THE COMPARATIVE STUDY BETWEEN THE IEEE-80 and IEC 60479:

A.1 Data of the comparison in terms of allowable touch voltage:

Table A.1: Data of the comparison in terms of allowable touch voltage

Fault clearing time	IEEE_50Kg	IEEE_70Kg	IEC_c1	IEC_c2	IEC_c3
0.01	814	1101	157	272	394
0.02	602	814	160	280	409
0.03	511	691	164	288	419
0.04	459	620	169	293	421
0.05	423	572	173	294	423
0.06	397	537	174	293	425
0.07	377	510	176	292	425
0.08	360	487	177	292	419
0.09	346	468	178	291	415
0.1	334	452	179	288	413
0.2	261	353	161	253	358
0.3	222	301	124	197	306
0.4	197	266	84	146	247
0.5	178	241	60	101	190
0.6	164	222	50	80	147
0.7	153	207	44	68	114
0.8	144	195	40	58	93
0.9	136	184	38	53	82
1	130	176	36	51	75
2	93	126	31	41	57
3	76	103	30	38	55
4	66	90	30	38	55
5	59	80	29	38	55
6	54	73	29	38	55
7	51	68	29	38	55
8	47	63	29	38	55
9	44	60	29	38	55
10	42	57	29	38	55

A.2 Data of the comparison in terms of body resistance:

Table A.2: Data of the comparison in terms of body resistance

Fault clearing time	IEEE_50Kg/70Kg	IEC_c1	IEC_c2	IEC_c3
0.01	1000	361	292	287
0.02	1000	363	293	288
0.03	1000	364	294	288
0.04	1000	365	296	288
0.05	1000	366	299	288
0.06	1000	367	303	288
0.07	1000	368	306	288
0.08	1000	369	309	288
0.09	1000	370	312	288
0.1	1000	371	316	288
0.2	1000	382	348	301
0.3	1000	399	374	328
0.4	1000	440	390	358
0.5	1000	497	420	378
0.6	1000	542	451	391
0.7	1000	573	482	410
0.8	1000	596	510	432
0.9	1000	612	530	449
1	1000	627	544	463
2	1000	674	604	518
3	1000	685	620	527
4	1000	689	624	528
5	1000	693	625	531
6	1000	694	625	531
7	1000	695	625	531
8	1000	695	625	531
9	1000	695	625	531
10	1000	696	625	531

A.3 Data of the comparison in terms of allowable step voltage:

Table A.3: Data of the comparison in terms of allowable step voltage

Fault clearing time	IEEE_50Kg	IEEE_70Kg	IEC_c1	IEC_c2	IEC_c3
0.01	1144	1548	299	556	810
0.02	846	1144	305	573	841
0.03	718	972	313	588	863
0.04	645	872	321	598	865
0.05	594	805	328	597	871
0.06	558	755	330	592	875
0.07	529	717	334	589	874
0.08	506	685	335	587	862
0.09	486	659	336	582	853
0.1	469	636	338	573	849
0.2	367	497	301	488	724
0.3	312	423	229	372	603
0.4	276	374	151	271	472
0.5	251	339	104	184	358
0.6	231	313	83	141	273
0.7	215	291	72	115	208
0.8	202	274	66	98	167
0.9	192	177	62	89	145
1	182	145	58	84	132
2	131	126	49	65	96
3	107	103	47	62	93
4	93	90	46	60	92
5	83	80	46	61	92
6	76	73	46	61	92
7	71	68	45	60	92
8	66	63	45	61	92
9	62	60	45	61	92
10	59	57	45	61	92

A.4 Data of the comparison in terms of surface layer resistivity:

Table A.4: Data of the comparison in terms of surface layer resistivity

Surface layer reisitivity	IEEE_50Kg	IEEE_70Kg	IEC_c1	IEC_c2	IEC_c3
100	222	301	258	430	731
200	246	334	286	478	812
300	270	366	314	524	890
400	294	398	341	570	968
500	317	430	369	615	1045
600	341	461	396	661	1122
700	364	493	423	706	1199
800	388	525	451	751	1276
900	411	556	478	797	1353
1000	434	588	505	842	1430
2000	668	904	776	1294	2198
3000	901	1220	1047	1747	2966
4000	1134	1536	1318	2199	3734
5000	1368	1851	1589	2651	4501
6000	1601	2167	1860	3103	5269
7000	1834	2483	2137	3555	6036
8000	2068	2799	2402	4007	6804
9000	2301	3114	2637	4459	7572
10000	2534	3430	2944	4911	8339

A.5 Data of the comparison in terms of surface layer depth:

Table A.5: Data of the comparison in terms of surface layer depth

surface layer depth	IEEE_50Kg	IEEE_70Kg	IEC_c1	IEC_c2	IEC_c3
0.01	341	462	396	661	1123
0.04	589	797	684	1141	1938
0.07	734	993	852	1422	2415
0.1	820	1110	953	1589	2699
0.13	875	1184	1016	1696	2879
0.16	912	1235	1060	1768	3002
0.19	939	1271	1091	1820	3090
0.22	959	1298	1114	1859	3156
0.25	975	1319	1132	1889	3207
0.28	987	1336	1147	1913	3248

Appendix B

Kumabarilla park earth grid injection testing report

POWERLINK QUEENSLAND
Internal Memorandum

DATE: 24 January 2014

TO: Principal Engineer Substation Electrical Design– R. Martin

FROM: Substation Electrical Design Engineer– J. Pinheiro.

H075 KUMBRILLA PARK SUBSTATION INJECTION TEST RESULTS

INTRODUCTION

This document summarizes the data used to check the design of the earth grid at H075 Kumbrilla Park Substation. The check was carried out using the Substation Design Procedures and Work Instructions which are based on the American National Standard "IEEE Guide for Safety in AC Substation Grounding ANSI/IEEE Std 80-2000".

TESTS PERFORMED

An injection test was carried out by PLQ on 16th January 2014 using the feeder(Feeder 8882) current injection method in accordance with the work instruction. The fault levels, system impedances were obtained from the Protection Engineer System Analysis for a 2012 system shown in Appendix F.

For the worst case 275kV phase to ground fault at H075 Kumbrilla park Substation, the grid to ground current (IG) is calculated to be 8468 A.

Soil Resistivity

The CDEGS soil model was adjusted to produce a reasonable correlation to the measured grid resistance and fall of potential gradient. The adjusted soil resistivity model is below.

Soil Layer	**Original Model** from the Design		**Modified Model** to reflect injection test	
	Soil Resistivity (Ωm)	Soil Layer Thickness (m)	Soil Resistivity (Ωm)	Soil Layer Thickness (m)
Top	Infinite	Infinite	Infinite	Infinite
Middle	350	0.4	350	0.4
Layer1	20	4	20	4
Layer2	35	Infinite	22	Infinite

RESULTS

Based on the measurements at selected test points (see Appendix-H), there are no areas of concern within the substation area, or at the substation fence.

Grid resistance

- The measured earth mat resistance of the substation R_G = 0.062Ω. This compares to a calculated resistance of 0.06253Ω using the CDEGS model.

Step and touch potentials

At 0.28s, 0.5s and 1s fault duration the Levels for inside and outside the substation fence (using the adjusted soil model) are; (IEEE Std.80-2000 50kg) as obtained from CDEGS.

Tolerable Limits 50kg person	Safe Touch Limit	Safe Step Limit
With **NO GRAVEL 1s**	176.3	363.3
With **NO GRAVEL 0.5s**	245.1	505.1
With **NO GRAVEL 0.28s**	319.3	658.0
3,000 Ω-m Surface (100mm crush rock layer over natural) **0.5s**	763.2	2577.5

	Touch Voltage	**Step Voltage**
Maximum scaled measured levels (**Within the Substation and outside boundary of fence**)	167.11V	13.5 V

Fall of Potential

Grid Potential rise for the fault current of 8.468KA is 529V.

Modelled Distance from the substation fence until safe touch voltage with respect to remote earth is reached with 0.5s clearing time.	≈ 55m approx
Measured Distance from the substation fence until maximum measured safe touch voltage with respect to remote earth is reached with 0.5s clearing time.	≈ 18m approx

Safe Limit of Earth Grid Current Discharge

Using the available information, it's approximated that the touch voltage limit within the substation boundary is reached without gravel when the grid to ground fault current reaches 21kA (using limits as per IEEE Std.80-2000 50kg, 0.5 sec clearing time).

RECOMMENDATIONS

The measured touch and step potentials do not exceed allowable values at H075 Kumbrilla Park substation with no gravel layer inside the substation fence and with no gravel layer outside the substation fence.

However, a gravel layer is installed inside the substation as per current plant maintenance strategies, regardless of requirements due to the touch and step voltages.

While no observation is reported of a remote earth hazard situation at present, attention is required to ensure none is bought within 18m of the substation. Similarly no continuous metallic connection (fence, pipelines, etc) originating at the substation shall continue beyond 18m from the fence.

Reasonable correlation is found between the measured values and the computed values by CDEGS.

Should the earth mat current increase due to system changes or the substation be substantially augmented then the entire earth grid design should be re-evaluated.

APPENDICES

A) EGPR Calculation
B) Fall of potential measurements
C) CDEGS fall of potential calculation
D) CDEGS Safety calculations table
E) CDEGS System information summary
F) EMPR summary
G) Decrement Factor Calculations
H) Step & Touch Potential Plan

REFERENCE

1. H075 Kumbrilla Park Substation Step & Touch Potential Plan Sketch
2. H075 Kumbrilla Park Injection Test Results
3. Aecom Earthing System Design Report.

Regards

J. Pinheiro
Substation Electrical Design Engineer

Checked

Electrical Design Engineer

Approved

7165

Principal Engineer Substation Electrical Design

APPENDIX A: EGPR Calculation

EARTH GRID RESISTANCE AND POTENTIAL RISE CALCULATION

Measured Volts	=	**0.823**	**Volts**
Injected Current	=	**25**	**Amps**
Ig	=	**8468**	**Amps**
K2	=	**0.527**	
K1= Ig / (I test x K2)	=	**642.73**	

EARTH GRID RESISTANCE :	=	**0.062**	**Ohms**
EARTH GRID POTENTIAL RISE :	=	**529.0**	**Volts**

	Scaled up from design report		Measured threshold	
safe step	**166**	**Volts**	**258.27**	**mV**
safe touch	**172**	**Volts**	**267.61**	**mV**

APPENDIX B: Fall of Potential Measurements.

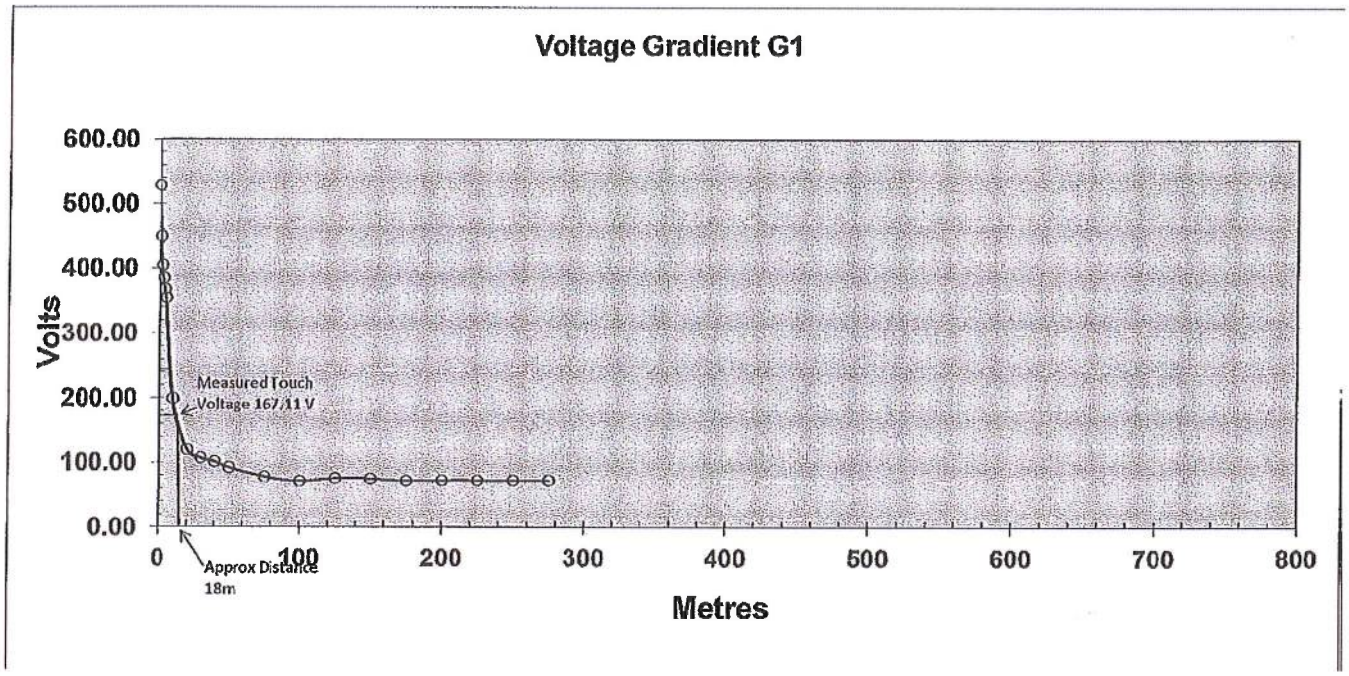

Voltage Gradient G2

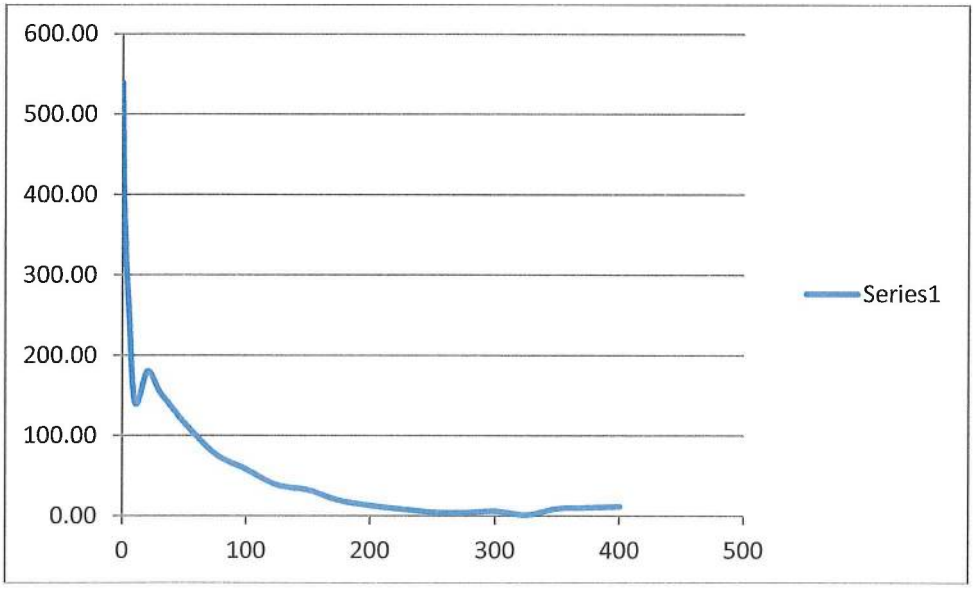

APPENDIX C: CDEGS Fall of Potential Calculation

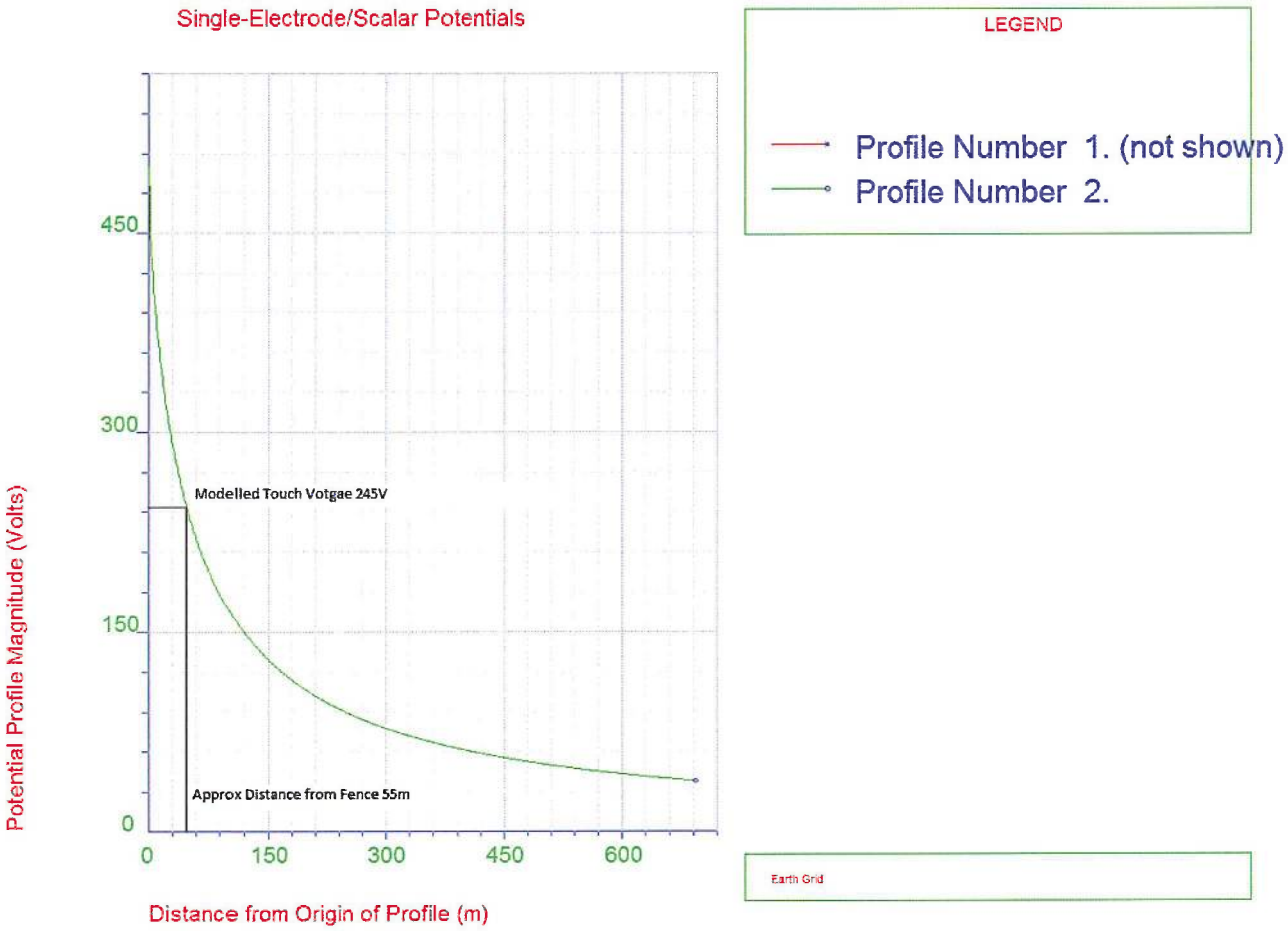

APPENDIX D: CDEGS Safety Calculations Table

DATE OF RUN (Start)= DAY 4 / Month 2 / Year 2014
STARTING TIME= 11:16:01:69

>> Safety Calculations Table

System Frequency.....(Hertz).: 50.000
System X/R.....: 11.251
Surface Layer Thickness.....(in).: 6.0000
Number of Surface Layer Resistivities.....: 10
Starting Surface Layer Resistivity.....(ohm-m).: NONE
Incremental Surface Layer Resistivity.....(ohm-m).: 500.00
Equivalent Sub-Surface Layer Resistivity....(ohm-m).: 350.00

Body Resistance Calculation.....: IEEE Std.80-2000
Fibrillation Current Calculation.....: IEEE Std.80-2000 (50kg)
Foot Resistance Calculation.....: IEEE Std.80-2000
User Defined Extra Foot Resistance: 0.0000 ohms

Fault Clearing Time (sec)	0.280	0.500	1.000
Decrement Factor	1.062	1.035	1.018
Fibrillation Current (amps)	0.219	0.164	0.116
Body Resistance (ohms)	1000.00	1000.00	1000.00

SURFACE LAYER RESIST-IVITY (OHM-M)	FAULT CLEARING TIME 0.280 sec. STEP VOLTAGE (VOLTS)	0.280 sec. TOUCH VOLTAGE (VOLTS)	0.500 sec. STEP VOLTAGE (VOLTS)	0.500 sec. TOUCH VOLTAGE (VOLTS)	1.000 sec. STEP VOLTAGE (VOLTS)	1.000 sec. TOUCH VOLTAGE (VOLTS)	FOOT RESIST-ANCE: 1 FOOT (OHMS)
NONE	658.0	319.3	505.1	245.1	363.3	176.3	1093.8
500.0	817.8	359.3	627.8	275.8	451.6	198.4	1480.9
1000.0	1334.3	488.4	1024.3	374.9	736.7	269.7	2732.0
1500.0	1842.7	615.5	1414.7	472.5	1017.5	339.8	3963.5
2000.0	2348.5	741.9	1803.0	569.6	1296.8	409.7	5188.7
2500.0	2853.2	868.1	2190.5	666.5	1575.4	479.3	6411.2
3000.0	3357.2	994.1	2577.5	763.2	1853.8	548.9	7632.2
3500.0	3861.0	1120.0	2964.2	859.9	2131.9	618.5	8852.4
4000.0	4364.4	1245.9	3350.7	956.5	2409.9	688.0	10071.9
4500.0	4867.7	1371.7	3737.1	1053.1	2687.8	757.4	11291.1

* NOTE * Listed values account for short duration asymmetric waveform decrement factor listed at the top of each column.

APPENDIX E: CDEGS System Information Summary

STARTING TIME= 11:13:08:77

==========< G R O U N D I N G (SYSTEM INFORMATION SUMMARY) >==========

Run ID.....: Earth Grid
System of Units .....: Metric
Earth Potential Calculations.....: Single Electrode Case
Type of Electrodes Considered.....: Main Electrode ONLY
Soil Type Selected.....: Multi-Layer Horizontal
SPLITS/FCDIST Scaling Factor.....: 8.4680

1
1

MULTI-LAYER EARTH CHARACTERISTICS USED BY PROGRAM

LAYER No.	TYPE	REFLECTION COEFFICIENT	RESISTIVITY (ohm-meter)	THICKNESS (METERS)
1	Air	0.00000	0.100000E+11	Infinite
2	Soil	-1.00000	350.000	0.400000
3	Soil	-0.891892	20.0000	4.00000
4	Soil	0.476190E-01	22.0000	Infinite

1

CONFIGURATION OF MAIN ELECTRODE
==========

Original Electrical Current Flowing In Electrode..: 1000.0 amperes
Current Scaling Factor (SPLITS/FCDIST/specified)..: 8.4680
Adjusted Electrical Current Flowing In Electrode..: 8468.0 amperes
Number of Conductors in Electrode.....: 69
Resistance of Electrode System.....: 0.62531E-01 ohms

SUBDIVISION
==========
Grand Total of Conductors After Subdivision.: 730

Total Current Flowing In Main Electrode.....: 8468.0 amperes
Total Buried Length of Main Electrode.....: 5957.1 meters

EARTH POTENTIAL COMPUTATIONS
==========

Main Electrode Potential Rise (GPR).....: 529.51 volts

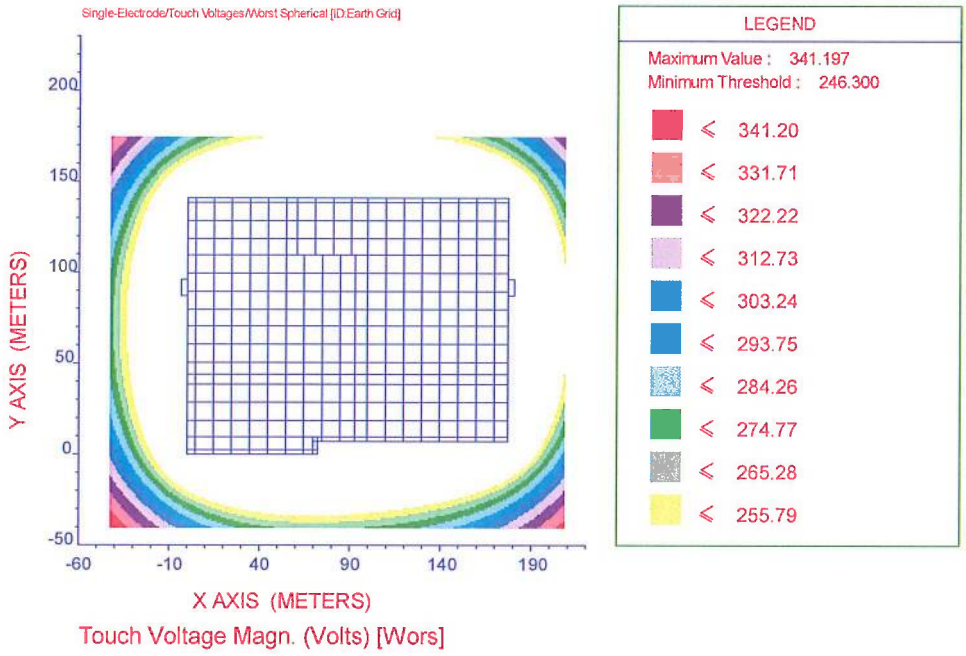

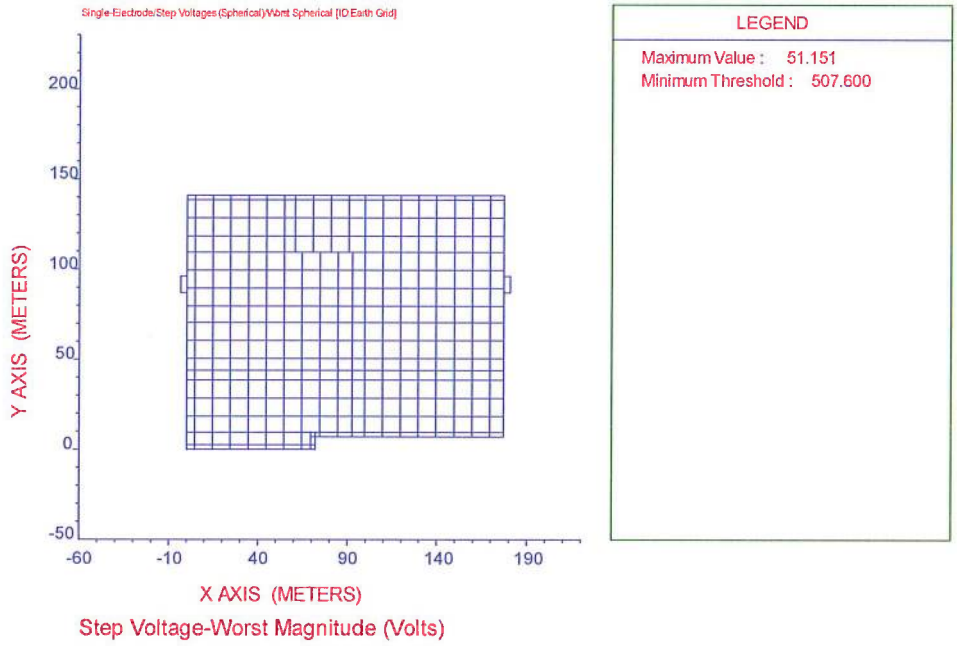

Note: The Touch & Step voltage graphs above are modelled With **NO GRAVEL 0.5s**

APPENDIX F: EMPR Summary

EMPR FOR H075 Kumarilla Park
Fault on 1T 275kV BUS Year 2012

H0751201

E. SUMMARY of RESULTS.

a. Plotted Values - (ohms and amps).

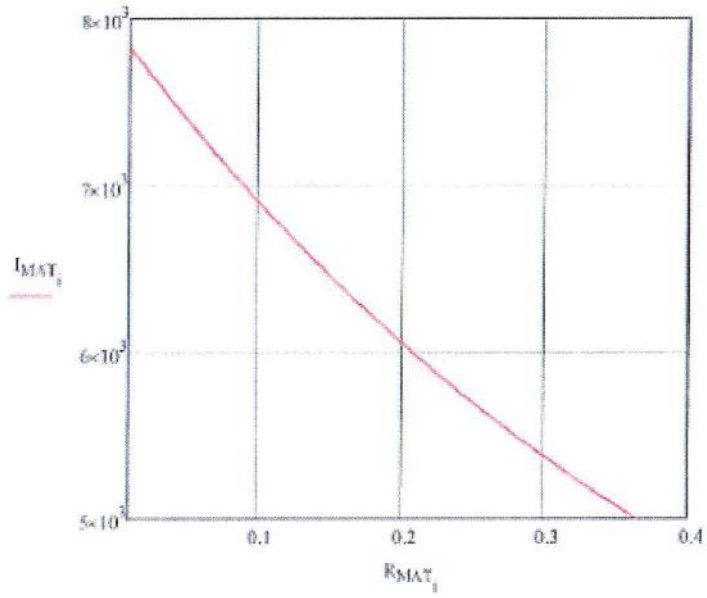

b. Table Values at Main Points - (ohms, volts and amps).

$n := 60, 61 .. 70$

n	R_{MAT_n}	V_{LNFR_n}	I_{MAT_n}
60	0.06	437.41	7290.20
61	0.06	444.08	7280.01
62	0.06	450.73	7269.90
63	0.06	457.37	7259.78
64	0.06	463.98	7249.68
65	0.07	470.57	7239.60
66	0.07	477.15	7229.54
67	0.07	483.71	7219.50
68	0.07	490.25	7209.49
69	0.07	496.76	7199.49
70	0.07	503.27	7189.52

c. Total Ground Current -(Amps)

$I_G = 3939.3$ $I_{MAT_{62}} = 7269.9$ $|I_{1T}| = 14217.2$

d. Fault Impedance -(p.u.)

$Z1 := 0.00108 + 0.01511j$ $Z2 := 0.00108 + 0.01437j$ $Z0 := 0.00190 + 0.01629j$

APPENDIX G: Decrement Factor Calculation

SUBJECT :- EARTH GRID DESIGN - DECREMENT FACTOR CALCULATION

SUBSTATION :- 1076 Kumbrilla Park

PROJECT :-

1. REFERENCES

(a) IELE Guide for Safety in AC Substation Grounding ANSI/IEEE Std 80-1986

(b) A.S. 2067-1984 Switching assemblies and ancillary equipment for A.t.ernating voltages above 1 kV

(c) QETC Engineering Standard 2.0-6

(d) ESAA course notes on Safe Earthing Design

2. GENERAL NOTES

(a) Design calculations are done on Mathcad for windows using file decrement factor.MCD located on the network under the directory.

(b) **Change input data** for your specific application. Values given are typical only

(c) Formula used in the following calculations are simplified empirical equations from reference (a) above

(i) There is a possibility that during a 0.5 sec. fault clearance there is a brief decontinuance of the fault and restriking it would not clear, this would be the worst case for decrement factor. The decrement factor shall be worked out using a total fault time of 0.5 sec. in two 0.25 sec. parts. That is t_a = 0.5 sec. and t_c = 0.25 sec. (p.105 Ref. (a)) as stated in the input data

3. INPUT DATA

$I_g := 7269.9$ Grid to earth current in amps calculated by Protection and Circuitry section I_{MAT}

$t_f := 0.1$ Time of earth fault duration in sec (page 105 Ref. (a)) - also see note (i) in Section 2

$V_{Base} := 275$ Voltage (ph - ph)

$S_{Base} := 100$ Base MVA

$Z_{1R} := 0.00108$) positive sequence resistance at the faulted location in p.u.
)

$Z_{1X} := 0.01511$) positive sequence reactance at the faulted location in p.u
)

$Z_{2R} := 0.00108$) negative sequence resistance at the faulted location in p.u
)

$Z_{2X} := 0.01437$) negative sequence reactance at the faulted location in p.u.
)

$Z_{0R} := 0.00196$) zero sequence resistance at the faulted location in p.u
)

$Z_{0X} := 0.0162$) zero sequence reactance at the faulted location in p.u
)

4. CALCULATIONS

$$Z_{Base} := \frac{V_{Base}^2}{S_{Base}}$$) Base Impedance
Ω
)

$Z_{Base} = 756.25$

$R_p := Z_{1R} Z_{Base}$ $R_0 := Z_{0R} Z_{Base}$ $X_p := Z_{1X} Z_{Base}$ $X_0 := Z_{0X} Z_{Base}$

$R_p = 0.817$) positive sequence resistance at the faulted location in ohms/phase

$X_p = 11.427$) positive sequence reactance at the faulted location in ohms/phase

$R_n = 0.817$) negative sequence resistance at the faulted location in ohms/phase

$X_n = 10.867$) negative sequence reactance at the faulted location in ohms/phase

$R_0 = 1.437$) zero sequence resistance at the faulted location in ohms/phase

$X_0 = 12.251$) zero sequence reactance at the faulted location in ohms/phase

) **calculated by Protection and Circuitry Section to determine the Decrement Factor (Section 13.9 Ref. (a)). worst fault condition normally at bus.**

4.3.1 Calculation of modified grid to earth current

$$XR := \frac{X_p + X_n + X_0}{R_p + R_n + R_0}$$

X/R ratio using components of subtransient impedance at the fault (p.104 Ref. (a))

$XR = 11.251$

$$T_a := \frac{XR}{2 \cdot \pi \cdot 50}$$

system subtransient time constant in sec (p 104 Ref. (a))

$T_a = 0.036$

$$D_f := \sqrt{1 + \frac{T_a}{t_f} \cdot \left(1 - \exp\left(-2 \cdot \frac{t_f}{T_a}\right)\right)}$$

decrement factor to increase current for time constant effects (eq. 65 Ref. (a))

$D_f = 1.165$

$I_G := I_g \cdot D_f$

grid to ground current in amps increased due to decrement factor above (eq. 64 Ref. (a))
- projection factor taken as 1, with future growth treated separately.

$I_G = 8468$

Appendix C

SUPPORTING DATA OF EARTH GRID LIGHTNING STUDY WITH CDEGS

In the following tables supporting data of lightning strike study of earth grid is presented. In these tables segment 1 refers to the grounding grid, and segment 2 refers to the copper rod used to feed lightning strikes to the grounding grid.

Frequency	Segment	Current entering origin of conductor (p.u.)	Current leaving origin of conductor (p.u.)	Current leaking through conductor surface (p.u.)
0	1	0.5197-j0.3562E-14	0	-0.5197+j0.3562E-14
	2	1.000+j0.000	0.5197-j0.3562E-14	-0.4803-j0.3562E-14
10000	1	0.5197-j0.3360E-04	0	-0.5197+j0.3360E-04
	2	1.000+j0.000	0.5197-j0.3360E-04	-0.4803-j0.3360E-04
20000	1	0.5197-j0.6699E-04	0	-0.5197+j0.6699E-04
	2	1.000+j0.000	0.5197-j0.6699E-04	-0.4803-j0.6699E-04
30000	1	0.5197-0.1004E-03	0	0.1004E-03+j1.039
	2	1.000+j0.000	0.5197-j0.1004E-03	-0.1004E-03+j0.9606
40000	1	0.5197-j0.1340E-03	0	-0.5197+j0.1340E-03
	2	1.000+j0.000	0.5197-j-0.1340E-03	-0.4803-j0.1340E-03
50000	1	0.5197-j0.1676E-03	0	-0.5197+j0.1676E-03
	2	1.000+j0.000	0.5197-0.1676E-03	-0.4803-j0.1676E-03
60000	1	0.5197-j0.2013E-03	0	-0.5197+j0.2013E-03
	2	1.000+j0.000	0.5197-j0.2013E-03	-0.4803-j0.2013E-03

Frequency	Segment	Current entering origin of conductor (p.u.)	Current leaving origin of conductor (p.u.)	Current leaking through conductor surface (p.u.)
70000	1	0.5197-j0.2352E-03	0	-0.5197+j0.2352E-03
	2	1.000+j0.000	0.5197-j0.2352E-03	-0.4803-j0.2352E-03
90000	1	0.5197-j0.3034E-03	0	-0.5197+j0.3034E-03
	2	1.000+j0.000	0.5197-j0.3034E-03	-0.4803-j0.3034E-03
110000	1	0.5197-j0.3722E-03	0	-0.5197+j0.3722E-03
	2	1.000+j0.000	0.5197-j0.3722E-03	-0.4803-j0.3722E-03
140000	1	0.5197-j0.4767E-03	0	-0.5197+j0.4767E-03
	2	1.000+j0.000	0.5197-j0.4767E-03	-0.4803-j0.4767E-03
250000	1	0.5198-j0.6946E-03	0	-0.5198+j 0.6946E-03
	2	1.000+j0.000	0.5198-j0.6946E-03	-0.4802-j0.6946E-03
360000	1	0.5198-j0.1206E-02	0	-0.5198+j0.1206E-02
	2	1.000+j0.000	0.5198-j0.1206E-02	-0.4802-j0.1206E-02
540000	1	0.5199-j0.1922E-02	0	-0.5199+j0.1922E-02
	2	1.000+j0.000	0.5199-j0.1922E-02	-0.4801-j0.1922E-02

Frequency	Segment	Current entering origin of conductor (p.u.)	Current leaving origin of conductor (p.u.)	Current leaking through conductor surface (p.u.)
720000	1	0.5200-j0.2743E-02	0	-0.5200+j0.2743E-02
	2	1.000+j0.000	0.5200-j0.2743E-02	-0.4800-j0.2743E-02
1080000	1	0.5201-j0.4374E-02	0	-0.5201+j0.4374E-02
	2	1.000+j0.000	0.5201-j0.4374E-02	-0.4799-j0.4374E-02
1440000	1	0.5202-j0.5972E-02	0	-0.5202+j0.5972E-02
	2	1.000+j0.000	0.5202-j0.5972E-02	-0.4798-j0.5972E-02
1800000	1	0.5203-j0.7588E-02	0	-0.5203+j0.7588E-02
	2	1.000+j0.000	0.5203-j0.7588E-02	-0.4797-j0.7588E-02
2160000	1	0.5204-j0.9222E-02	0	-0.5204+j0.9222E-02
	2	1.000+j0.000	0.5204-j0.9222E-02	-0.4796-j0.9222E-02
2520000	1	0.5205-j0.1087E-01	0	-0.5205+j0.1087E-01
	2	1.000+j0.000	0.5205-j0.1087E-01	-0.4795-j0.1087E-01
2560000	1	0.5205-j0.1106E-01	0	-0.5205+j0.1106E-01
	2	1.000+j0.000	0.5205-j0.1106E-01	-0.4795-j0.1106E-01